Age-Independent Oceanic Plate Thickness and Asthenosphere Melting from SS Precursor Imaging

Shuyang Sun[1] and Ying Zhou[1]

[1]Virginia Tech

December 8, 2022

Abstract

The Earth's asthenosphere is a mechanically weak layer characterized by low seismic velocity and high attenuation. The nature of this layer has been strongly debated. In this study, we process twelve years of seismic data recorded at the global seismological network (GSN) stations to investigate SS waves reflected at the upper and lower boundaries of this layer in global oceanic regions. We observe strong reflections from both the top and the bottom of the asthenosphere, dispersive across all major oceans. The average depths of the two discontinuities are 120 km and 255 km, respectively. The SS waves reflected at the lithosphere and asthenosphere boundary are characterized by anomalously large amplitudes, which require 12.5% reduction in seismic velocity across the interface. This large velocity drop can not be explained by a thermal cooling model but indicates 1.5%-2% localized melt in the oceanic asthenosphere. The depths of the two discontinuities show large variations, indicating that the asthenosphere is far from a homogeneous layer but likely associated with strong and heterogeneous small-scale convections in the oceanic mantle. The average depths of the two boundaries are largely constant across different age bands. In contrast to the half space cooling model, this observation supports the existence of a constant-thickness plate in oceanic regions with a complex and heterogeneous origin.

Age-Independent Oceanic Plate Thickness and Asthenosphere Melting from SS Precursor Imaging

Shuyang Sun[1] **and Ying Zhou**[1]

[1]Department of Geosciences, Virginia Tech, Blacksburg, VA 24061, USA

Key Points:

- SS precursors reveal depths of the lithosphere-asthenosphere boundary independent of seafloor age
- The oceanic lithosphere-asthenosphere boundary is a strong reflector and can be explained by 1.5%-2% of partial melt
- Large depth variations of the top and the bottom boundaries of the asthenosphere suggest a heterogeneous melting process

Corresponding author: Shuyang Sun, `sysun@vt.edu`

Abstract

The Earth's asthenosphere is a mechanically weak layer characterized by low seismic velocity and high attenuation. The nature of this layer has been strongly debated. In this study, we process twelve years of seismic data recorded at the global seismological network (GSN) stations to investigate SS waves reflected at the upper and lower boundaries of this layer in global oceanic regions. We observe strong reflections from both the top and the bottom of the asthenosphere, dispersive across all major oceans. The average depths of the two discontinuities are 120 km and 255 km, respectively. The SS waves reflected at the lithosphere and asthenosphere boundary are characterized by anomalously large amplitudes, which require $\sim$12.5% reduction in seismic velocity across the interface. This large velocity drop can not be explained by a thermal cooling model but indicates 1.5%-2% localized melt in the oceanic asthenosphere. The depths of the two discontinuities show large variations, indicating that the asthenosphere is far from a homogeneous layer but likely associated with strong and heterogeneous small-scale convections in the oceanic mantle. The average depths of the two boundaries are largely constant across different age bands. In contrast to the half space cooling model, this observation supports the existence of a constant-thickness plate in oceanic regions with a complex and heterogeneous origin.

Plain Language Summary

In the plate tectonic theory, the outermost shell of the Earth consists of a small number of rigid plates (lithosphere) moving horizontally on the mechanically weak asthenosphere In oceanic regions, the lithosphere is thought to be formed by gradual cooling of the hot mantle. Therefore, the thickness of the plate depends on the age of the seafloor. The problem with the classic half space cooling model is that bathymetry and heat flow measurements at old seafloors do not follow its predicted age dependence. A modified theory, called the plate model, can better explain those geophysical observations by assuming additional heat at the base of an oceanic plate with a constant thickness of about 125 km. However, such a constant-thickness plate has not been observed in seismology. In this study, we image the asthenosphere boundaries using a global dataset of seismic waves reflected off the Earth's internal boundaries. We observe strong reflections from both the top and the bottom of the asthenosphere, across all major oceans. The amplitudes of these waves can be explained by 1.5%-2% of partial melt and the average boundary depths are independent of seafloor age. This observation supports the existence of a constant-thickness plate in the global oceans with a complex origin.

1 Introduction

In the plate tectonic theory, the outermost shell of the Earth consists of a small number of rigid plates (lithosphere) moving horizontally on the mechanically weak asthenosphere. The origin of the asthenosphere as well as the defining mechanism of its top and bottom rheological interfaces have been highly controversial (Fischer et al., 2010; Rychert et al., 2012; Kawakatsu & Utada, 2017; Fischer et al., 2020; Rychert et al., 2020; Karato, 1992; Gaherty & Jordan, 1995). The oceanic plates make up ∼70% of the Earth's surface and they have a relatively simple geological and tectonic history and therefore they are ideal for resolving these fundamental questions. The classic half-space cooling model predicts that the thickness of the thermal boundary layer as well as the depth of the ocean increase proportionally with the square root of the sea-floor age. While this simple conductive cooling model successfully explains the first-order observations in the oceans, bathymetry and heat flow measurements at seafloor older than ∼70 million years do not follow the age dependence predicted by the half space cooling model. The plate model, which assumes additional heat at the base of an oceanic plate with a constant thickness, successfully explains the flattening of sea floor depth and heat flow observations (Parsons & Sclater, 1977). However, such a constant-thickness plate has not been observed in seismology, and the exact source of the additional heat remains unclear, probably associated with small-scale convections (Richter, 1973; Richter & Parsons, 1975; Parsons & Sclater, 1977; Richards et al., 2020) or oceanic hotspots (Korenaga & Korenaga, 2008).

It is a general feature in global seismic surface wave studies that the high-velocity lid in oceanic regions becomes thicker with sea-floor age (French et al., 2013; James et al., 2014; Godfrey et al., 2017; Ma & Dalton, 2019). It has also been suggested that a plate model with additional heat at a constant depth of about 125 km fits surface wave observations (Maggi et al., 2006). Recent surface-wave studies suggest a small amount of melt is trapped within the entire low-velocity oceanic asthenosphere (Debayle et al., 2020), which might provide the additional heat required by the plate model. The depths of the lithosphere-asthenosphere boundary (LAB hereinafter) have also been studied using secondary seismic phases reflected or converted at the interface, including SS precursors (Rychert & Shearer, 2011; Schmerr, 2012; Tharimena et al., 2017), receiver functions (Li et al., 2000, 2004; Kawakatsu et al., 2009; Rychert & Shearer, 2009) and active source studies (Stern et al., 2015; Mehouachi & Singh, 2018). Those studies suggest large variations as well as an origin of the asthenosphere much more complex than gradual thermal variations with depth as predicted in the half space cooling model (D. Turcotte & Oxburgh, 1967). A variety of rheological mechanisms have been proposed, including a change in grain size (Faul & Jackson, 2005), seismic anisotropy (Karato & Wu, 1993; Beghein et al., 2014; Auer et al., 2015), elastically accommodated grain boundary sliding (Karato, 2012) and near melting (Yamauchi & Takei, 2016). The large velocity drop and high attenuation also make partial melt a dominant mechanism in many studies (Fischer et al., 2020; Rychert et al., 2020; Debayle et al., 2020; Stern et al., 2015; Mehouachi & Singh, 2018; Schmerr, 2012; Tharimena et al., 2017; Li et al., 2000, 2004; Kawakatsu et al., 2009). For example, a thin sublithosphere melt channel beneath the normal oceanic seafloor has been proposed for the equatorial Atlantic Ocean (Mehouachi & Singh, 2018).

The velocity increase at the base of the asthenosphere has been incorporated in the widely used 1-D global reference earth model, PREM, with about $\sim$7% of velocity increase across the 220-km discontinuity (Dziewonski & Anderson, 1981). A discontinuity at about this depth was first observed in Europe and North America (Lehmann, 1959, 1961; Hales et al., 1980) and later confirmed by studies using surface-wave dispersion measurements, underside seismic reflections, ScS reverberations and receiver functions (Goncz & Cleary, 1976; Vidale & Benz, 1992; Revenaugh & Jordan, 1991; Sacks et al., 1979). This discontinuity has been reported in continental regions and is also called the Lehmann discontinuity. However, many studies have concluded that the 220-km discontinuity is not global in nature and a reflection from this depth is missing in the global long-period stacks (Shearer, 1991; Gu et al., 2001; Deuss & Woodhouse, 2002, 2004; Schmerr & Garnero, 2006), which indicates that the existence of the discontinuity is either absent in oceanic regions, or there are large variations in the depth of this discontinuity.

In this paper, we analyze twelve years of long-period transverse component seismograms recorded at 151 GSN stations (Fig. S1) to investigate SS waves reflected at the top and the bottom of the asthenosphere in oceanic regions, namely, the $S_{\mathrm{LAB}}S$ wave reflected at the LAB and the $S_{220}S$ reflected at the bottom of the asthenosphere. We will interpret the low velocity zone (LVZ) between the two discontinuities observed in oceanic regions as the asthenosphere ("weak layer") as it roughly corresponds to the depth range of the global

LVZ in model PREM. This is the depth range where geotherm may exceed mantle solidus and partial melt occurs (D. L. Turcotte & Schubert, 2002).

2 Data & Methods

SS precursors are underside reflections from internal discontinuities and they arrive before the main SS waves which are reflected at the surface of the Earth. SS precursors are very sensitive to the structures of the interfaces at the reflection midpoints, about halfway between the earthquake and the station. They provide good data coverage in the global oceanic areas where seismic stations are sparse. In this study, we examine 32,369 broadband seismograms at 151 GSN station from 543 earthquakes occurred between January 2009 and December 2020 with SS-wave reflection points in oceanic regions (Figs 1 & 2). The moment magnitude of the earthquakes ranges from 6.0 to 8.0 such that SS precursors are excited by potentially sufficient seismic energy (Schmerr, 2012). We download seismograms from the Data Management Center at the Incorporated Research Institutions for Seismology (IRIS). The instrument responses are removed and the East-West and North-South component displacement seismograms are rotated to obtain the radial and transverse component seismograms.

The seismograms are band-pass filtered between 10 and 80 mHz and decimated to 0.1 second sampling interval. Seismograms with weak or complex SS waves due to source processes are discarded (Figs S2 & S3). Seismograms with noisy SS waves and precursors are also discarded (Fig. S3). This leaves 6,143 sets of transverse component seismograms with epicentral distances greater than 80°. We visually inspect seismograms for SS precursors, including $S_{\mathrm{LAB}}S$, $S_{220}S$, $S_{410}S$ and $S_{660}S$. Clear $S_{\mathrm{LAB}}S$ arrivals are identified on 1,380 seismograms (about 22.5% of the entire dataset) from 144 stations and 395 earthquakes (Figs 1 & 2). The majority of the data with strong $S_{\mathrm{LAB}}S$ waves (981 out of 1380) have focal depths shallower than 45 km, and the epicentral distance varies between 80.1° and 176.3° with the majority larger than 100° (Fig. S1).

SS precursors from the 220-km discontinuity ($S_{220}S$) are observed on 2,756 seismograms. We are able to pick more $S_{220}S$ phases than $S_{\mathrm{LAB}}S$ phases from seismograms partly because many $S_{\mathrm{LAB}}S$ arrivals are too close to the main SS wave arrivals and they are not used in this study to avoid strong phase interferences. The $S_{\mathrm{LAB}}S$ and $S_{220}S$ signals can be both clearly observed on 1,021 of seismograms. There is no apparent geographic pattern associated with the presence (or absence) of the SS precursors (Fig. 2). The amplitudes of the secondary reflected waves are expected to be small, and the SS precursors are often below the noise level due to weak source radiation, small reflection coefficient and/or defocusing caused by mantle heterogeneities. For example, only about 30% of the recorded SS waves have clear SS precursors from the 410-km and the 660-km discontinuities in recent global studies (Guo & Zhou, 2020, 2021).

The observed SS precursors from the LAB ($S_{\mathrm{LAB}}S$) are characterized by large amplitudes that are comparable to the amplitudes of the mantle transition zone SS precursors $S_{410}S$ and $S_{660}S$ (Fig. 1). To investigate the velocity reduction across the LAB discontinuity, we construct 1-D reference models modified from PREM to include a large velocity drop in the asthenosphere (Fig. 3 & Fig. S4). We calculate synthetic seismograms based on traveling-wave mode summation (Liu & Zhou, 2016). The global centroid-moment-tensor (CMT) solutions and the USGS Preliminary Determination of Epicenters (PDE) source locations and origin times are used in the calculations of the 1-D synthetic seismograms. The synthetic seismograms are complete, including all seismic phases with exact amplitudes for earthquakes in 1-D earth models. The effects of incident angles on seismic amplitudes have been automatically accounted for. The synthetic seismograms are then processed using the same bandpass filter as applied to the observed seismograms. The differences in SS precursors between different models facilitate the identification of the $S_{\mathrm{LAB}}S$ and $S_{220}S$ waves on the observed seismograms (Fig. 3).

We measure the amplitudes of the SS precursors $S_{\mathrm{LAB}}S$, $S_{410}S$ and $S_{660}S$ at a period of 25 seconds. The measurements are made in the frequency domain using a 40-second window centered at the arrival time of the SS precursors (Fig. 4). We use a short time window to limit the interference between the $S_{\mathrm{LAB}}S$ wave and the main SS wave. Example amplitude measurement experiments using synthetic data show that amplitude ratios at the measurement frequency as well as their frequency-dependent variations can be well captured using a 40-second time window (Fig. 5). We will focus on measurements at a period of 25 seconds in this study. The longest half duration of the earthquakes used in this study is about 25 seconds and seismic energy often decreases rapidly at frequencies higher than the earthquake corner frequency. In addition, SS precursors at higher frequencies can be heavily contaminated by noises (meteorological and multiple scattering). At periods much longer than 25 seconds, seismograms are not suitable for SS precursor studies as the precursors are not well separated and surface-wave overtone dispersion also becomes a problem. The frequency dependence of the measurements and their corresponding finite-frequency sensitivities will be documented in a separate paper. Amplitude ratios $S_{\mathrm{LAB}}S/S_{410}S$ and $S_{\mathrm{LAB}}S/S_{660}S$ are calculated for the observed datasets as well as synthetic seismograms in 1-D reference models (Fig. 6).

We measure the differential arrival times between the SS waves and their precursors in the dataset. The observed and synthetic seismograms are aligned using the SS traveltime measurements, and the residue arrival times of the SS precursors are then calculated in the frequency domain at a period of 25 seconds (Xue et al., 2015) (Fig. 7). The time shifts due to uncertainties in source origin times do not affect the final measurements as only $\delta t|_{S_{\mathrm{LAB}}S} - \delta t|_{SS}$ and $\delta t|_{S_{220}S} - \delta t|_{SS}$ differential traveltimes are used to determine the depths of the discontinuities. The length of the measurement windows ranges from 42 to 117 seconds for SS waves, 37 to 69 seconds for $S_{\mathrm{LAB}}S$ waves and 38 to 75 seconds for $S_{220}S$ waves. The length of a measurement window depends on the arrivals of the neighboring phases, and the measurement windows are chosen to minimize possible phase interferences. The relation between time delays and depth perturbations of the discontinuities depends on their finite-frequency sensitivity kernels. We calculate finite-frequency traveltime sensitivities to boundary depth perturbations in the framework of travelling-wave mode coupling, which fully account for source radiation patterns, phase interactions as well as time-domain windowing and tapering applied in making frequency-dependent measurements (Deng & Zhou, 2015; Zhou, 2009; Zhou et al., 2005). Example finite-frequency boundary sensitivity kernels for traveltime measurements are plotted in Fig. 4. The finite-frequency sensitivities display a typical X shape due to the minimax-time nature of the reflected waves (Dahlen, 2005). Unlike direct body waves which have minimum-time ray paths, surface-reflected phases are minimax waves in that the reflection point is a stationary maximum for perturbations in the source-receiver ray plane and a minimum for perturbations perpendicular to the plane.

Seismic waves at different frequencies are sensitive to different regions (Fresnel zones) and this introduces frequency-dependent time shifts when lateral variations exist in discontinuity topography, as a result, SS precursors do not always have the same polarities as expected for 1-D earth models (Guo & Zhou, 2020). The interferences between different waves within the measurement window are accounted for in the calculation of the finite-frequency sensitivities, including the travel time curves of the interference phases as well as their amplitudes. We use traveltime sensitivity kernels to identify possible phase interferences in the measurement windows, including interferences with the main SS waves and other phases such as the precursors of depth phases (Fig. S5), precursors and/or multiples of ScS waves (Fig. S6). Sensitivity kernels with abnormal values indicate strong interferences and those measurements are excluded (Figs S5 & S6). In addition, we exclude measurements out of the two standard deviations. This leaves 1274 and 929 sets of measurements for $S_{\rm LAB}S$ and $S_{220}S$, respectively. The thicknesses of the asthenosphere at the 921 locations are calculated as the depth difference between the 220-km discontinuity and the LAB.

3 Results

We process a total number of 32,369 transverse component seismograms that have reflection points in oceanic regions and observe clear SS waves on 6,143 seismograms with simple source time functions. SS precursors are secondary reflected waves, their amplitudes are much smaller than the main SS waves and they are often heavily influenced by scattered waves and phase interactions. As expected, the majority of the seismograms with clear SS waves do not show strong SS precursors from the two discontinuities. The most striking observation from this dataset is the anomalously large amplitudes of the $S_{\rm LAB}S$ phases on 1,380 seismograms, with the majority (1,021 out of 1,380) accompanied by strong $S_{220}S$ phases. The SS precursors are well separated from the main SS waves, and their amplitudes are comparable to the amplitudes of the mantle transition zone phases, $S_{410}S$ and $S_{660}S$ (Fig. 1). The geographic distribution of the reflection points is dispersive across major oceans, including the Pacific, the Atlantic and the Indian ocean, with seafloor age spanning from 10 to 170 million years old (Fig. 1).

3.1 Large Amplitudes of the LAB SS precursors

To quantify the observed large amplitudes of the SS precursors associated with the LAB discontinuity, we calculate the amplitude ratios between the $S_{\rm LAB}S$ phase and two reference phases, $S_{410}S$ and $S_{660}S$. The amplitude measurements are made in the frequency domain based on spectra division at a period of 25 seconds (Guo & Zhou, 2020; Xue et al., 2015), In Fig. 6, we plot the histograms of the minimum amplitude ratios, defined as $\gamma = \text{minimum}[\log(A_{S_{\text{LAB}}S}/A_{S_{410}S}), \log(A_{S_{\text{LAB}}S}/A_{S_{660}S})]$ (Table S1). We have used the minimum values to avoid over amplification when the amplitude of $S_{410}S$ or $S_{660}S$ is small due to scattering or defocusing. The precursors $S_{\text{LAB}}S$ and $S_{410}S$ (or $S_{660}S$) have similar ray paths in the bulk mantle, the use of amplitude ratios minimizes the impact of possible focusing and defocusing effects. In addition, the main SS waves travel through the same regions sampled by the SS precursors, and the distribution the SS amplitude measurements for the entire dataset is very similar to that for the subset in which anomalously large $S_{\text{LAB}}S$ were observed, indicating that the observed large amplitudes of the $S_{\text{LAB}}S$ waves are not a result of focusing caused by mantle heterogeneities (Fig. S7). To investigate possible interference from the main SS waves and other phases on the frequency-domain $S_{\text{LAB}}S$ amplitude measurements, we make additional time-domain amplitude measurements using the maximum value of the envelope function for each $S_{\text{LAB}}S$ measurement window. The measurements made in the frequency domain based on spectra division and those made in the time domain using envelope functions in general agree well (Fig. S8). The observed mean value of the minimum amplitude ratio γ is close to zero (Fig. 6), indicating that the reflection coefficients at the LAB are about the same as those at the 410 and the 660. The corresponding velocity contrasts across the LAB are expected to be larger than the contrasts across the 410 and the 660 due to their smaller incident angles at shallower depths. The geographic distribution of the amplitude ratios do not show dependence on the age of the sea floor (Fig. 6).

To estimate the velocity change across the LAB, we construct a 1-D reference model with the depths of the LAB and the 220-km discontinuity at 130 km and 250 km, respectively (Fig. 3). The velocity jump across the LAB is 12.5% in the reference model (Model I). SS precursors from all upper mantle discontinuities can be clearly identified on the observed seismograms when the observed and synthetic seismograms are filtered to the same frequency band (Fig. 1). We make amplitude measurements and calculate the relative amplitude ratios $\gamma = \text{minimum}[\log(A_{S_{\text{LAB}}S}/A_{S_{410}S}), \log(A_{S_{\text{LAB}}S}/A_{S_{660}S})]$ using the synthetic seismograms following the same process as applied on the observed seismograms. The amplitude ratios between $S_{\text{LAB}}S$ and $S_{410}S$ (or $S_{660}S$) calculated for Model I are very close to the observations (Fig. 6). To better constrain the velocity drop across the LAB required to produce the large amplitudes of $S_{\text{LAB}}S$, we introduce two additional models, Model II with 6% of velocity drop and Model III with 11% of velocity drop across the LAB. Example synthetic seismograms are plotted in Fig. 3 and the amplitude measurements are plotted in Fig. 6. The mean logarithm amplitude ratio γ calculated using Model II as a reference model is -0.3, meaning that the corresponding average amplitudes of the LAB precursors are about 50% of the amplitudes of the 410 (or the 660) precursors, much smaller than the observations. The mean logarithm amplitude ratio γ calculated using Model III as a reference model is slightly smaller than the observed value. Based on the calculations, we conclude that 12.5% of velocity drop across the LAB is necessary in our model to explain the observed large amplitude of the $S_{\mathrm{LAB}}S$ waves (Fig. 6).

3.2 Depths of the LAB and the 220-km Discontinuity

To constrain the depths of the LAB and the 220-km discontinuity, we measure the differential traveltimes $\delta t|_{S_{\mathrm{LAB}}S} - \delta t|_{SS}$ and $\delta t|_{S_{220}S} - \delta t|_{SS}$ with respect to synthetic seismograms calculated in Model I (Fig. 7), similar to the studies of Guo & Zhou (2020, 2021) in which $S_{410}S$ and $S_{660}S$ traveltime measurements were used to investigate the depths of the 410-km and the 660-km discontinuities at a global scale. The time shifts due to uncertainties in source origin times do not affect the final measurements as we use differential traveltimes. We apply 3-D crust and mantle wave speed corrections using global models CRUST1.0 (Laske et al., 2013) and S40RTS (Ritsema et al., 2011). Model I is constructed as the reference model for the oceanic regions where large-amplitude SS precursors have been observed. As it is not a global reference model, there is overall about 5 seconds of traveltime shifts in $\delta t|_{S_{\mathrm{LAB}}S}$-$\delta t|_{SS}$ after 3-D wavespeed and crustal corrections (Fig. 7 & Fig. S9). The mean $\delta t|_{S_{220}S}$-$\delta t|_{SS}$ traveltime delay before and after the corrections remains approximately the same, with an average value close to zero. This indicate that the average velocity in the uppermost mantle in the reference model is close to the global average.

To obtain depth perturbations of the LAB and the 220-km discontinuity, we calculate the sensitivities of the differential traveltimes to depth perturbations of the interfaces by integrating the finite-frequency sensitivity kernels over the surface of the boundary (Fig. 4). The LAB depths obtained from this study varies between ~70 and ~160 km (Fig. 8) and the mean LAB depths obtained using the same data with and without the corrections are 120 km and 125 km, respectively (Figs. 8 & S10). The depth of the 220-km discontinuity varies between 180 and 340 km with a mean value of ∼255 km, and it does not change with wavespeed and crustal corrections. We calculate the thickness of the asthenosphere in regions where both the LAB and the 220-km discontinuities are well defined by strong SS precursors from both discontinuities. The thickness of the asthenosphere ranges from 50 km to 220 km with an average of 140 km. Large depth variations of the LAB and the 220-km discontinuity are observed across the global oceanic regions and the depth can change abruptly over small geographic distances.

The depths of the LAB and the 220-km discontinuity are plotted as a function of seafloor age in Fig. 9. The depths of the two discontinuities obtained using the same dataset but without the 3-D crustal and mantle wave speed corrections are plotted in Fig. S11. The average depth of the two discontinuities are independent of seafloor age, regardless of the corrections applied. To quantify uncertainties in traveltime measurements and discontinuity depth perturbations, we calculate frequency-dependent traveltime measurements at five different periods ranging from 23 to 27 seconds. The standard deviation of those traveltime measurements are then converted to uncertainties in discontinuity depth using the corresponding finite-frequency sensitivities. The depth uncertainties are plotted as error bars in Fig. 9, they are generally small, with an average of 1.1 km for the LAB and 1.2 km for the 220-km discontinuity.

4 Discussions

4.1 Melt Spots in the Oceanic Asthenosphere

The observed large amplitudes of the SS precursors require a large velocity change across the LAB. The presence of a small amount of melt may significantly reduce seismic velocity. It has been suggested that S-wave velocity reduction is about 7.9% for every percent of melt in realistically shaped melt in the upper mantle based on finite element calculations for shear modulus reduction (produced by the presence of a connected network of realistically shaped and naturally organized melt inclusions), with the geometries of the inclusions taken directly from laboratory calculations (Hammond & Humphreys, 2000). The finite element model predictions are also in general agreement with recent experimental results (Chantel et al., 2016). The large amplitudes of the SS precursors observed in this study can be explained by 1.5%-2% of melt in the asthenosphere. This melt concentration is comparable to observations at mid-ocean ridges, for example, the East Pacific Rise (Team, 1998). In a recent surface-wave study (Debayle et al., 2020), a large melt fraction of up to 1% beneath the entire oceanic lithosphere has been suggested, in general agreement with the overall estimation of melt (0.3-2%) from electrical conductivity study (Ni et al., 2011).

A sharp increase in the water content across the LAB has been proposed as a possible candidate for significant wave speed reduction through enhanced anelasticity (Karato, 2012; Karato & Jung, 1998). To explore the effect of anelasticity (seismic quality factor Q) on the amplitudes of SS precursors, we calculate synthetic seismograms in models with and without strong anelasticity in the asthenosphere and compare the amplitudes of the SS precursors. In Fig. 10, the velocity and density structures in Model I and Model IV are identical but their Q values in the asthenosphere are different, Q=80 in Model I and Q=20 in Model IV. The low Q value in the asthenosphere in Model IV results in a much smaller SS amplitude but the amplitude reduction on the $S_{\mathrm{LAB}}S$ wave is very limited. This is because while both the SS wave and the $S_{\mathrm{LAB}}S$ wave experience more attenuation due to enhanced anelasticity, anelasticity also reduces the effective wave speed in the low Q region. Therefore, the effective velocity contrast across the LAB increases, resulting a larger reflection coefficient and increased amplitude of the $S_{\mathrm{LAB}}S$ wave. The amplitude ratios calculated in Model I (Fig. 6) and Model IV (Fig. 10) do not show significant differences in their histograms. We conclude that the large amplitudes of $S_{\mathrm{LAB}}S$ waves therefore can not be explained by a change in anelasticity.

The observed large amplitudes of the SS precursors can not be explained by seismic anisotropy. Strong radial anisotropy (up to 10%) has been observed in the oceanic asthenosphere with SH waves travelling faster than SV waves (Dziewonski & Anderson, 1981; Zhou et al., 2006; Nettles & Dziewoński, 2008; Burgos et al., 2014; Beghein et al., 2014). This radial anisotropy would lead to larger SH wave velocity beneath the LAB, and therefore reduced velocity contrast across the LAB and smaller precursor amplitudes, while the observed large amplitudes of the SS precursors require anomalously large velocity drop (12.5%) across the boundary. Frozen-in radial anisotropy in the oceanic lithosphere from petrological fabrics or melt ponding has been suggested (Auer et al., 2015). In this case, the SH wave speed would become faster in the oceanic lithosphere, which may cause a larger SH velocity contrast across the LAB but a reduced velocity contrast in SV velocity. In this study, strong

$S_{\mathrm{LAB}}S$ phases are also observed on the radial component seismograms (Fig. S12). The observed SS precursors with large amplitudes also display a good azimuth coverage (Fig. 1), indicating that the observed large amplitudes of the $S_{\mathrm{LAB}}S$ waves are unlikely a result of azimuth anisotropy in the lithosphere (Beghein et al., 2014).

It is important to emphasize that we have interpreted the low velocity zone (LVZ) between the two discontinuities observed in oceanic regions as the asthenosphere, and we have modeled the wavespeed structure associated with reflected waves as first-order discontinuities. In 1-D earth models (e.g., PREM), a first-order discontinuity is an equivalent mathematical representation of the earth structure. The same applies to other discontinuities in the Earth including the Moho, the 410 and the 660. Synthetic seismograms calculated based on the equivalent first-order discontinuities can explain the observed seismograms. The large amplitude of the LAB phase observed in this study requires about 12.5% of velocity jump across a first-order discontinuity. The same velocity change over a gradient zone of 5 km or less may also explain the observed $S_{\mathrm{LAB}}S$ amplitudes, with less than 2% of difference in their average amplitudes (Fig. S13). If the velocity change occurs over a much larger gradient zone of 20 km, the average $S_{\mathrm{LAB}}S$ amplitude will decrease by $\sim$17%, and the required velocity increase would be larger in order to produce the same peak amplitude (Deng & Zhou, 2015).

4.2 Age-Independent Thickness of the Oceanic Plate

The observed LAB SS precursors characterized by large amplitudes can be modeled as waves reflected off a first-order discontinuity with a large velocity contrast. The strong SS precursors from the LAB are observed across the global oceanic regions, with an average depth of 120 km that is independent of seafloor age (Fig. 9). This observation supports the plate model for the oceanic bathymetry and heat flow measurements, in which a reheating process is required at the base of the oceanic plate with a constant thickness of about 100-125 km. The reheating process is probably caused by small-scale mantle convection beneath the large oceanic plate (Richards et al., 2020).

The observed depths of the LAB in this study are characterized by substantial local variations. The standard deviation of the LAB depths calculated for the entire dataset is at ~15 km. We calculate the standard deviation of the LAB depths at different length scales (Fig. S14). The standard deviation can be up to ~17 km at small length scales and it becomes consistent with the standard deviation of the entire dataset when the length scale exceeds ~1000 km. Reflectors at depths between 120 and 180 km have been detected across the Pacific ocean in a *SS* precursor stacking study, though they were found in only 16% of the stacks (Schmerr, 2012). LAB reflectors at depths of about 100-140 km have been reported in Hawaii where high-resolution receiver function studies are available with the deployment of local stations (Li et al., 2000, 2004). The large variation of the LAB depths is also consistent with surface waves studies in which individual transects often display considerable depth variability in age-averaged profiles (Rychert et al., 2020; French et al., 2013).

In seismic studies, age-dependent reflectors have been reported in several oceanic regions, especially under the young seafloors (Rychert et al., 2021; Rychert & Shearer, 2011; Tharimena et al., 2017; Wang et al., 2020). For example, a recent receiver function study from ocean bottom seismometers in the equatorial Mid Atlantic Ocean discovered that the LAB depth increases from about 30 km at the mid-ocean ridge to about 80 km beneath 30 million years old seafloors in some locations (Rychert et al., 2021). The relation between the crust age and the LAB depth is much less clear across the Pacific Ocean and it has been suggested that regional dynamical processes may play an important role in asthenospheric melt production (Schmerr, 2012). In this study, we use long period SS waves, as a result, signals from a very shallow reflector (<40 km) will interfere with the main SS waves and will not be picked up. It is also possible that there may be multiple reflectors in the lithosphere in some regions and what we observe in this study represents a strong deep reflector associated with melting not secular cooling. In general, velocity change associated with a thermal lithosphere is expected to be smaller and much more gradual than the reflectors associated with the chemical differentiation (melting) process.

Similar to the LAB, the depths of the 220-km discontinuity also do not depend on the age of the seafloor and are characterized with large local variations. It is understood that the smoothness (roughness) of a same discontinuity in different studies often depends on the regions of study as well as smoothing applied in some of the inversions. Reflectors at depths of 250-300 km (the X discontinuity) have been observed in many oceanic regions, including the South Pacific and the Indian Ocean (Deuss & Woodhouse, 2002, 2004). Large depth variations up to ∼100 kilometers on the 220-km discontinuity have been report over length scales of several hundred kilometers beneath the northwestern Pacific in a short-period array study (Rost & Weber, 2001). The large local variations in the depths of the discontinuities are expected to generate significant variability in both the waveforms and travel times of the SS precursors. When stacking is applied to SS precursors with reflection points in regions where large depth variations occur over very short distances, it may be possible that the large amplitudes of SS precursors could be effectively averaged out in stacking results due to phase equalization (Gu et al., 2001). In Fig. S14, we show a simple example to illustrate the concept that, in some cases, the large amplitudes of SS precursors may not be picked up in stacking results when large variations in SS precursor amplitudes and arrival times are present.

5 Conclusions

The thermal boundary as predicted by the half space cooling model is not observed in SS precursors in this study. Instead, we observe anomalously large amplitudes of SS precursors reflected off the lithosphere-asthenosphere boundary (LAB), which can be explained by ∼12.5% of velocity drop across the boundary. This indicates 1.5%-2% of localized melt across the global oceanic regions. The large variability in the depths and amplitudes of the SS precursors observed across the global oceanic region suggests a heterogeneous melting process in the oceanic asthenosphere. The majority of the LAB SS precursors are accompanied by strong reflections from the 220-km discontinuity. This indicates that the 220-km discontinuity may define the lower boundary of the local asthenosphere where melting occurs.

The plate model, which requires additional heat at the base of a constant-thickness oceanic plate, explains the bathymetry and heat flow observations that do not follow half space cooling predictions. While such a constant-thickness plate has not been reported in seismic studies, the oceanic plate as defined by the strong LAB reflector in this study does not thicken with age but show an average depth of 120 km across different age bands. This observation supports the existence of a constant-thickness plate in oceanic regions. The localized melt spots distributed over the global oceanic regions may be essential to decouple the oceanic plates from the underlying mantle by dramatically reducing the mantle viscosity

(Debayle et al., 2020; Holtzman, 2016).

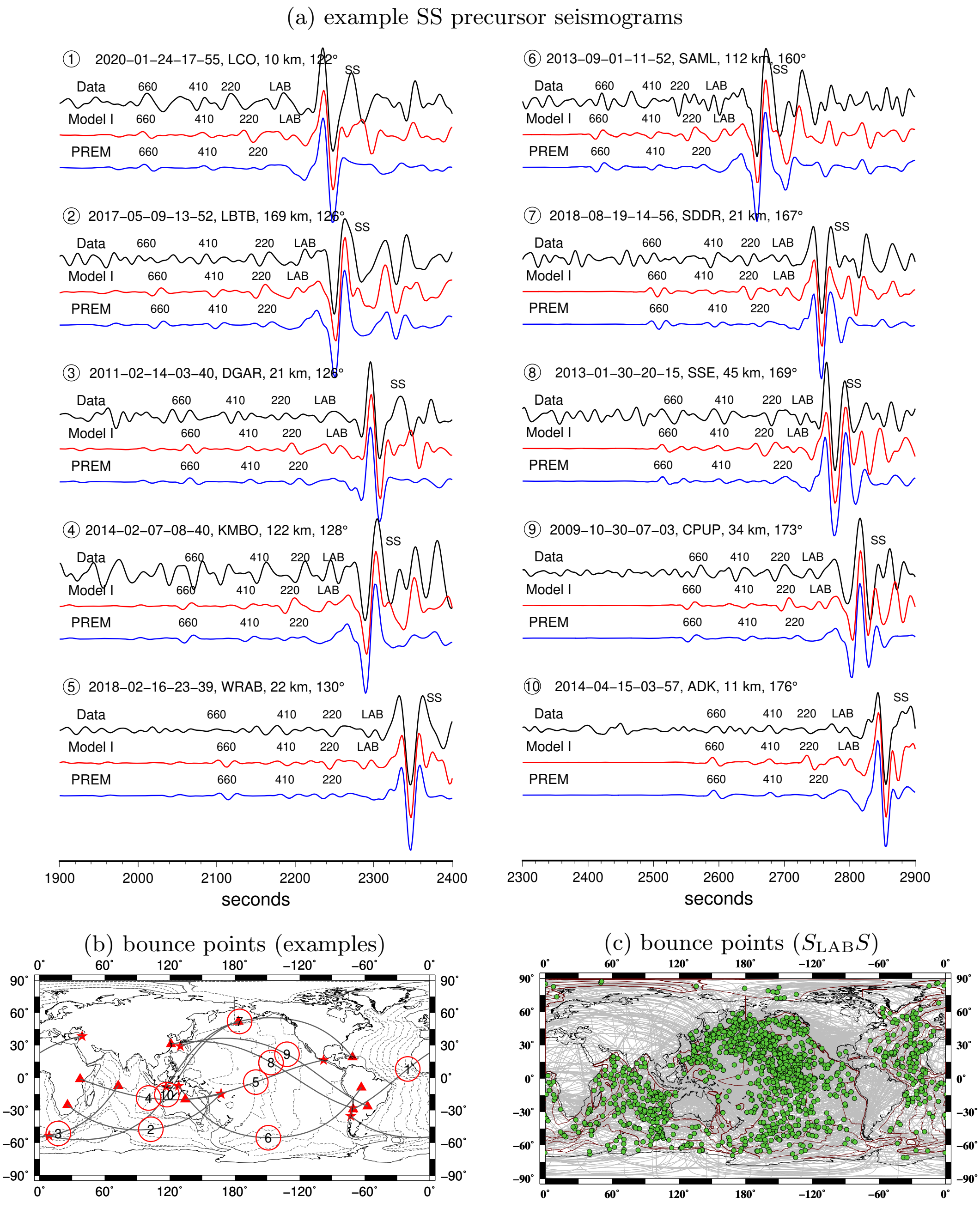

Figure 1: (a) example transverse-component seismograms with large-amplitude $S_{\mathrm{LAB}}S$ and $S_{220}S$ phases. The black seismograms are data, the red seismograms are synthetics calculated in a reference 1-D model (Model I) with 12.5% of the velocity jump across the LAB, and the blue synthetics are calculated in PREM in which there is no discontinuity at the LAB depth. The reference models are plotted in Fig. 3. The seismograms have been band-pass filtered between 10 and 80 mHz and aligned using their SS arrivals for better illustration. The precursor closest to the main SS wave is labeled as $S_{\mathrm{LAB}}S$ as we investigate possible reflections from the top of the asthenosphere. The arrivals of the $S_{220}S$, $S_{410}S$ and $S_{660}S$ waves are also labeled. The earthquake event date/time and station name as well as depth and epicentral distance are denoted on each seismogram. The corresponding geographic ray paths (black lines) and bounce points (red circles) of the $S_{\mathrm{LAB}}S$ waves are plotted in (b). Ray paths and bounce points of the 1,380 $S_{\mathrm{LAB}}S$ waves with anomalously large amplitudes are plotted in (c). Seafloor age contours are plotted at 20, 60, 100 and 140 Ma.

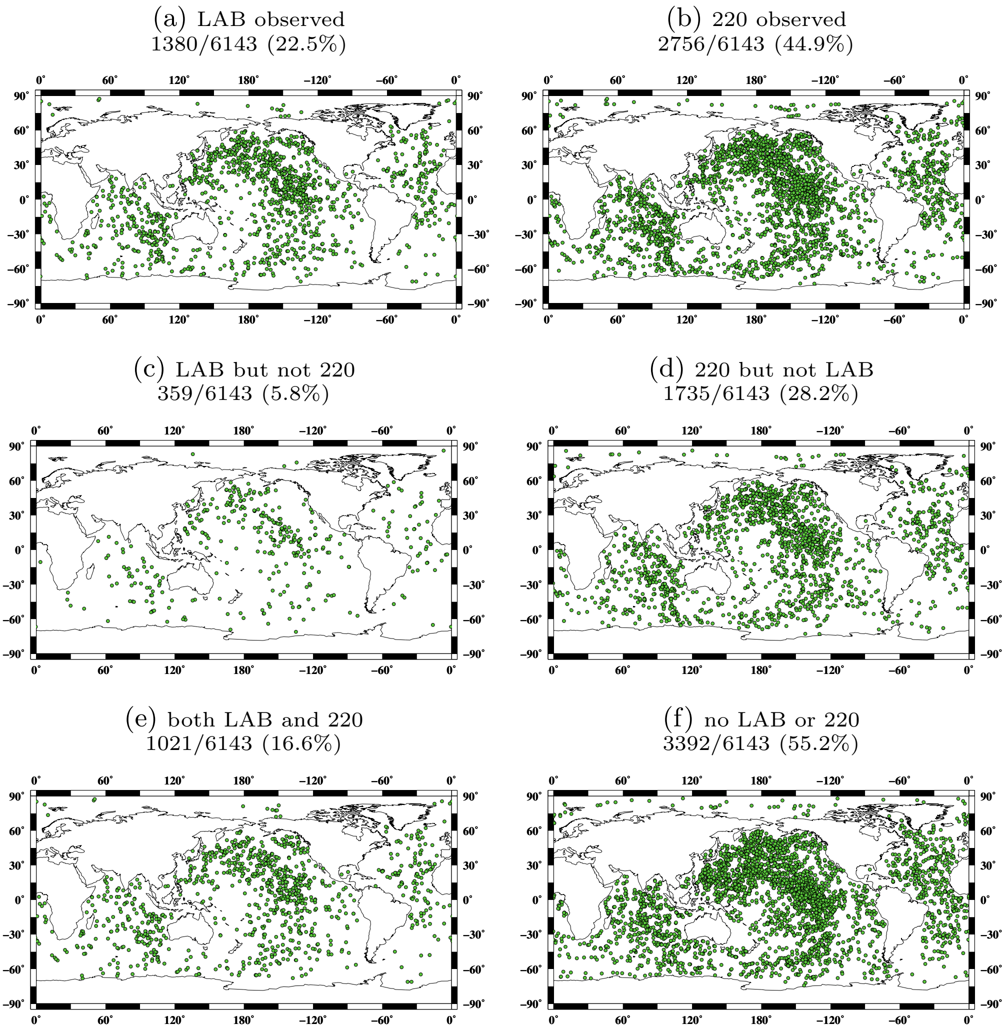

Figure 2: Geographic distribution of subsets of the data plotted at SS bounce points. (a) clear $S_{\mathrm{LAB}}S$ observed, (b) clear $S_{220}S$ observed, (c) $S_{\mathrm{LAB}}S$ observed but not $S_{220}S$, (d) $S_{220}S$ observed but not $S_{\mathrm{LAB}}S$, (e) both $S_{\mathrm{LAB}}S$ and $S_{220}S$ observed, (f) no $S_{\mathrm{LAB}}S$ or $S_{220}S$ observed. There is no apparent geographic pattern associated with either the presence or absence of the $S_{\mathrm{LAB}}S$ and $S_{220}S$.

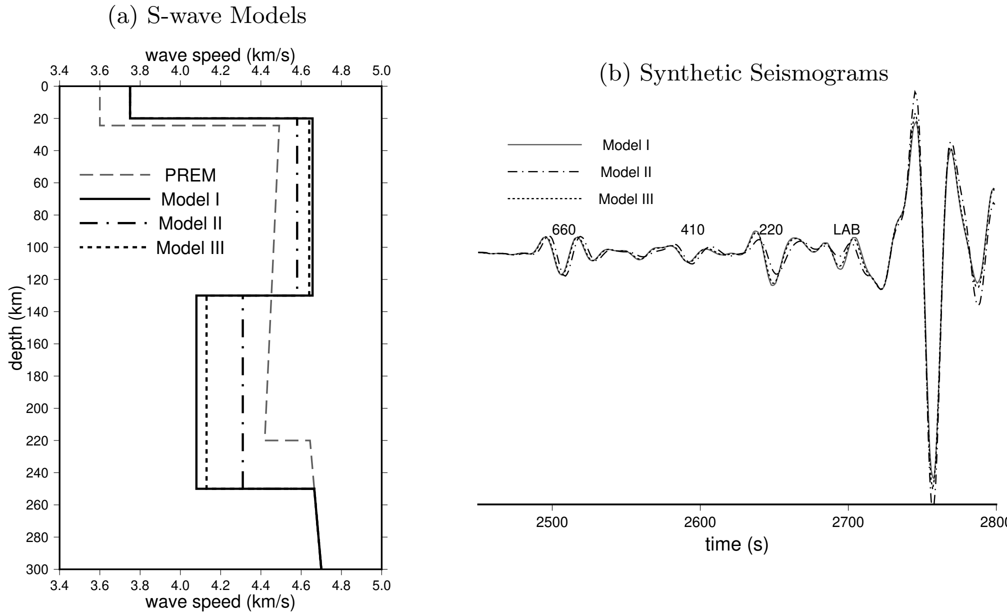

Figure 3: (a) Three 1-D reference earth models Model I, Model II and Model III used in this study and their corresponding example synthetic seismograms are plotted in (b). Model PREM is also plotted in (a) for reference. The synthetic seismograms are calculated using the three reference models for a magnitude 6.9 Indonesia earthquake occurred in August 2018 recorded at a GSN station SDDR (https://doi.org/10.7914/SN/CU). The observed seismogram is plotted in Fig. 1. The seismograms have been band-pass filtered between 10 and 80 mHz and have been aligned using the main SS wave arrivals for better illustration. The velocity contrast across the LAB at a depth of 130 km is 12.5% in Model I, 6% in Model II and 11% in Model III. The corresponding $S_{\mathrm{LAB}}S$ wave amplitude in Model I is much larger than that in Model II and slightly larger than that in Model III, as expected.

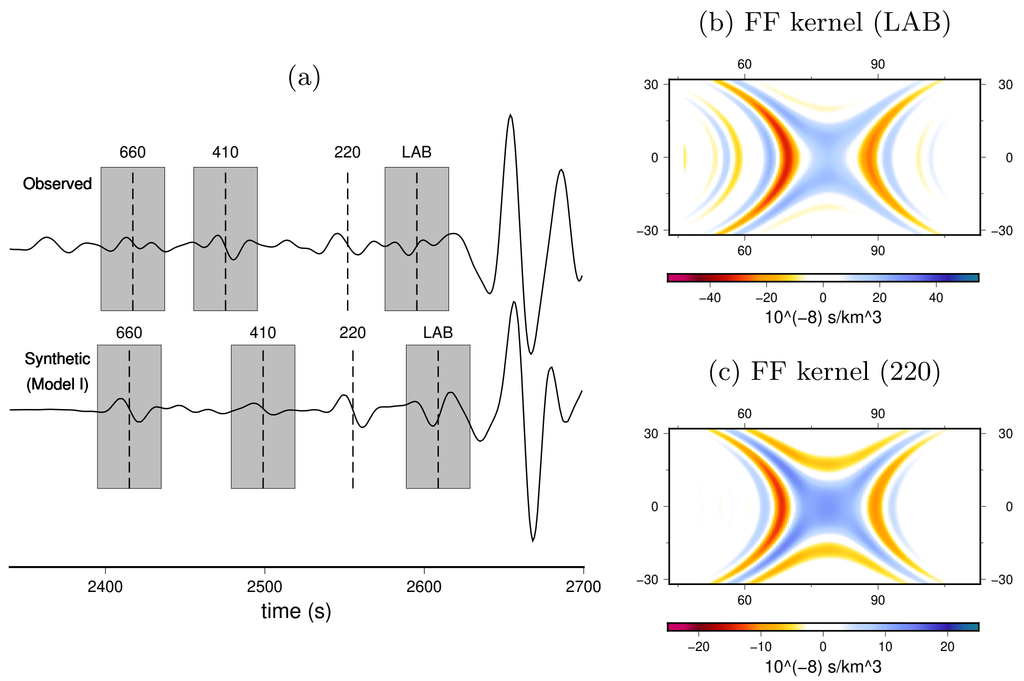

Figure 4: (a) shows example measurement windows used for LAB amplitude ratio measurements $A_{S_{\mathrm{LAB}}S}/A_{S_{410}S}$ and $A_{S_{\mathrm{LAB}}S}/A_{S_{660}S}$. The seismograms are for a magnitude 6.6 Mexico earthquake occurred in January 2016 recorded at a GSN station MSEY (https://doi.org/10.7914/SN/II), and the epicentral distance is 158°. The synthetic seismogram is calculated for Model I as in Fig. 3 and both seismograms have been band-pass filtered between 10 and 80 mHz. (b) and (c) are finite-frequency traveltime boundary sensitivity kernels for the $S_{\mathrm{LAB}}S$ and $S_{220}S$ waves, respectively. The sensitivity kernels are plotted in map view in the ray coordinates, centered at the bounce point which is about 79° away from the source and the receiver.

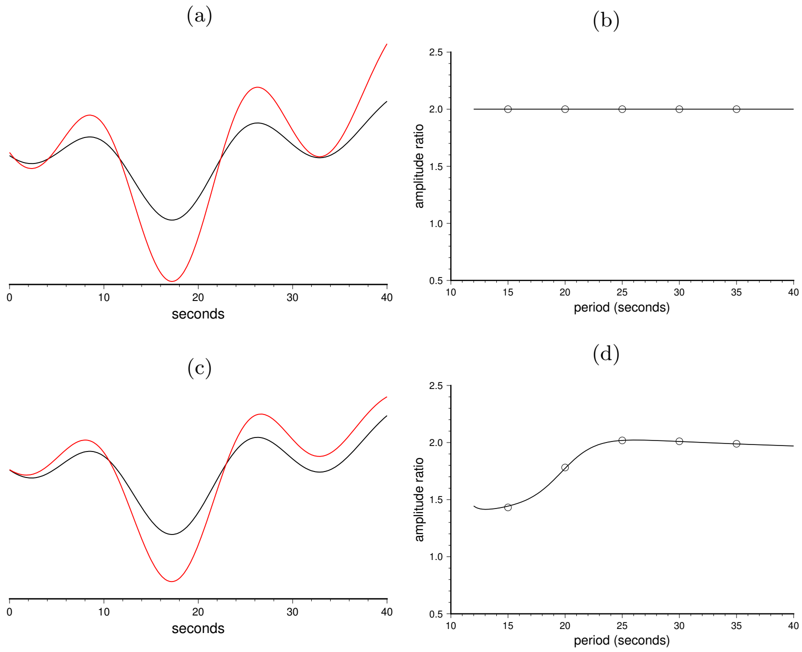

Figure 5: Synthetic amplitude measurement experiment using the same 40-second time window as applied in data. (a) The black seismogram is the LAB phase from the observed seismogram in Fig. 4, and we multiply the seismogram by a constant factor of two (frequency-independent) to obtain the red seismogram. (b) Theoretical amplitude spectral ratio (black line) and measurements made at periods of 15, 20, 25, 30 and 35 seconds (circles). (c) The black seismogram is the same as in (a) and the red seismogram is obtained by multiplying the amplitude spectrum of the black seismogram with a frequency-dependent function. The corresponding theoretical amplitude ratios and measurements made at 15, 20, 25, 30 and 35 seconds period are plotted in (d). The experiment confirms that amplitude ratios at the measurement frequency (25 seconds) can be determined using a 40-second time window.

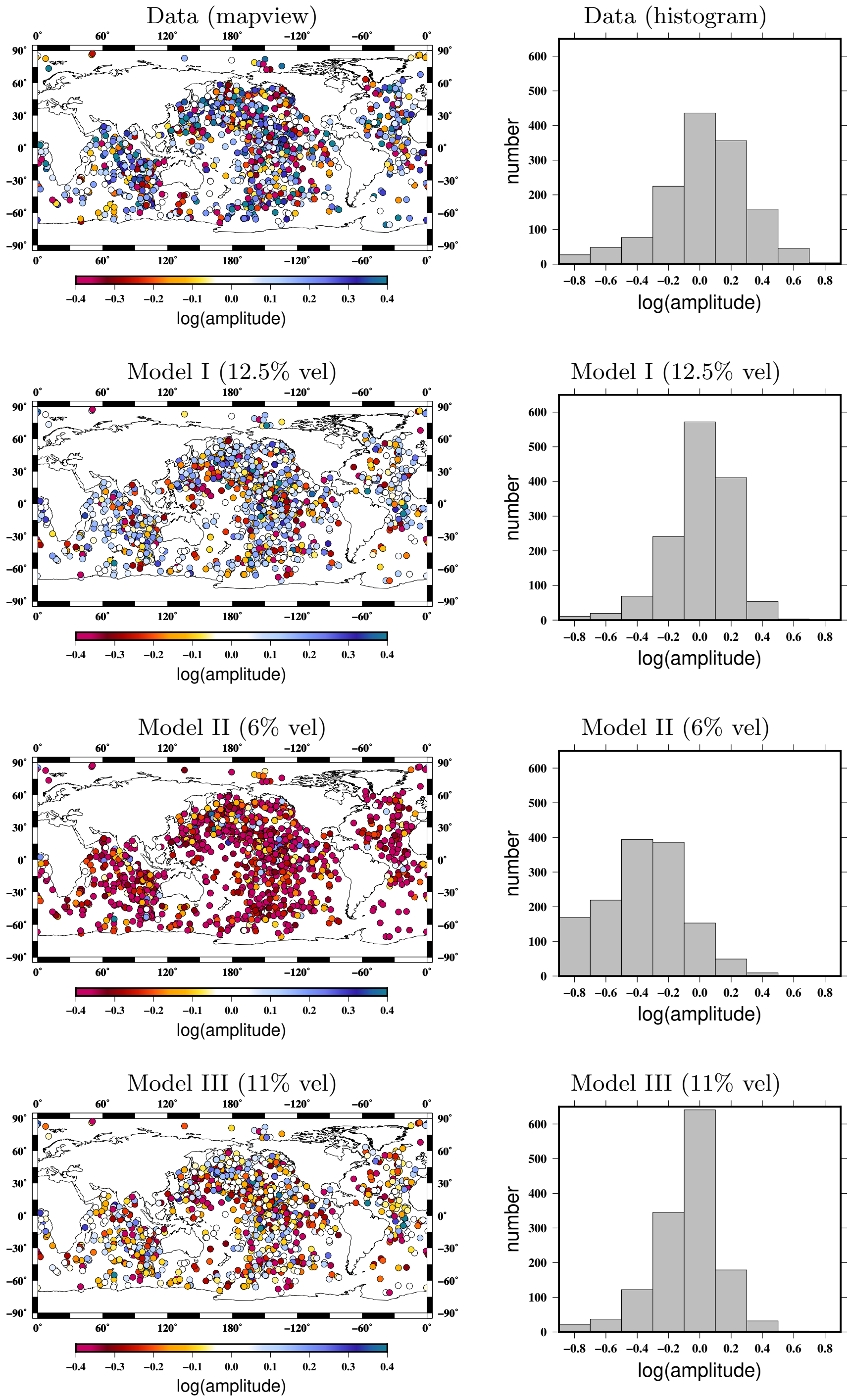

Figure 6: $S_{\text{LAB}}S$ amplitude measurements $\gamma = \text{minimum}\,[\log(A_{S_{\text{LAB}}S}/A_{S_{410}S}), \log(A_{S_{\text{LAB}}S}/A_{S_{660}S})]$ obtained using observed seismograms (top) as well as synthetic seismograms calculated for three reference models (Model I, II and III) plotted at the bounce points in mapviews and histograms. The observed $S_{\text{LAB}}S$ amplitudes show a similar distribution (histogram) to the amplitude ratios calculated for Model I (12.5% velocity drop across the LAB). The amplitude ratios calculated in Model II (6% velocity drop across the LAB) are overall much smaller than the observations, and the amplitude ratios calculated in Model III (11% velocity drop across the LAB) are slightly smaller than the observed amplitude ratios. We conclude that the observed large amplitude of the $S_{\text{LAB}}S$ waves can be explained by 12.5% of velocity drop across the LAB.

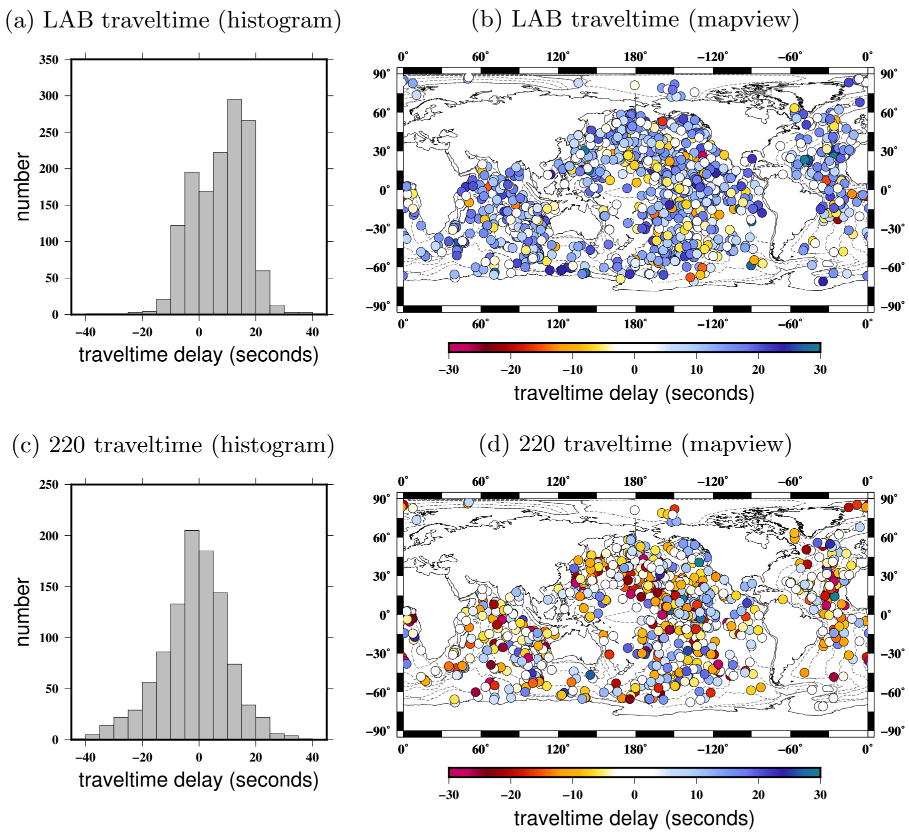

Figure 7: (a) and (b) are $S_{\mathrm{LAB}}S$ traveltime measurements plotted in histograms and mapviews at their bounce points. The measurements are made with respect to Model I synthetic seismograms. 3-D mantle wavespeed and crustal corrections have been applied. (c) and (d) are the same as (a) and (b) but for $S_{220}S$.

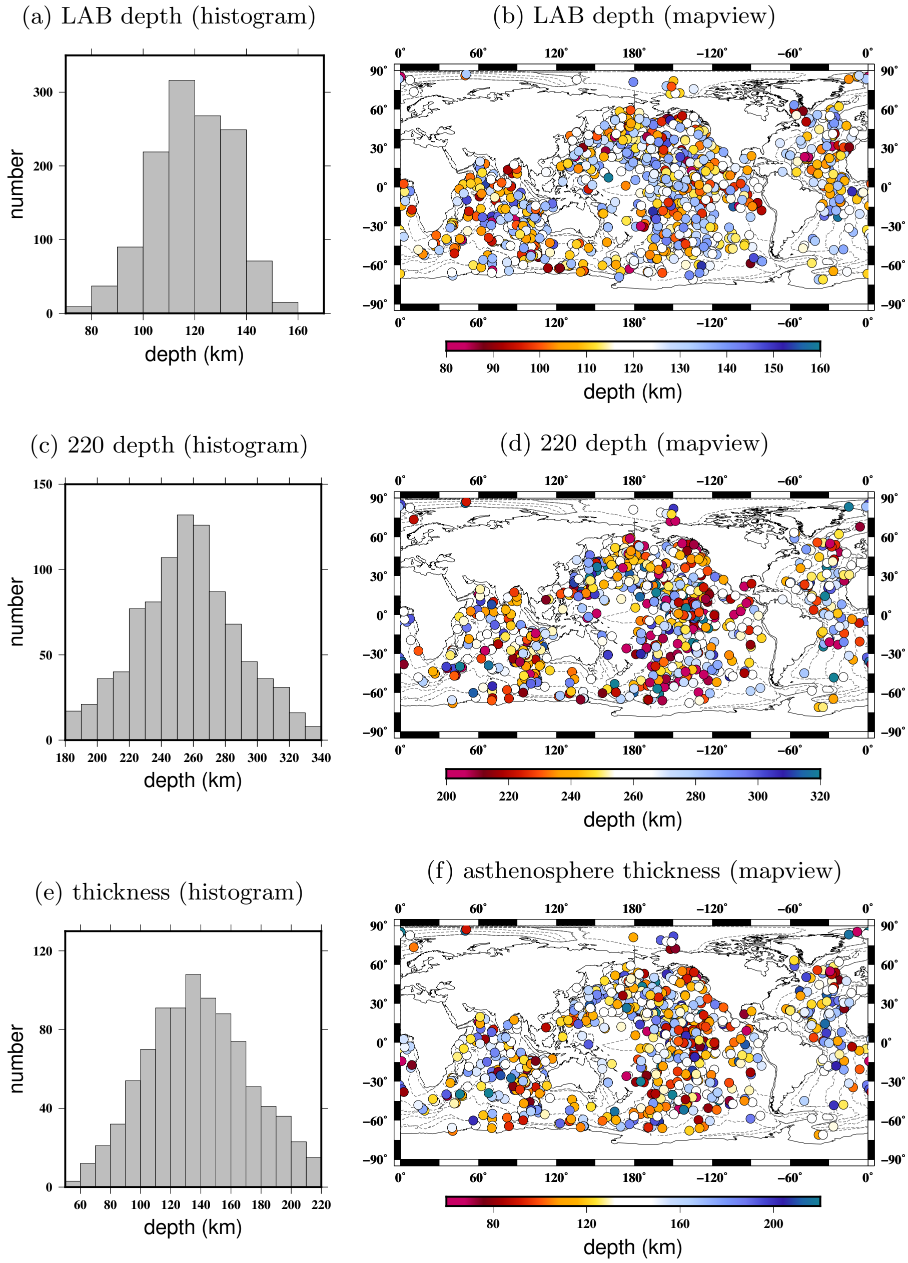

Figure 8: (a) and (b) are the depths of the LAB calculated from traveltime measurements, plotted in histogram and mapview at $S_{\mathrm{LAB}}S$ bounce points. (c) and (d) are the depths of the 220-km discontinuity. (e) and (f) are the asthenosphere thicknesses calculated from the depths of the LAB and the 220.

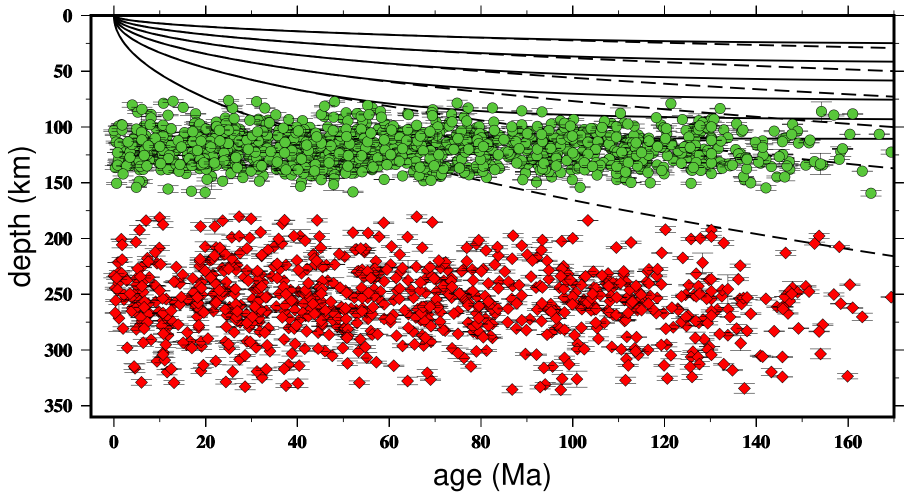

Figure 9: **Age-independent thickness of the oceanic plate.** Green circles and red diamonds are depths of the LAB and the 220-km discontinuity obtained from this study, plotted as a function of the seafloor age. Isotherms at an interval of 200°C (starting at 300°C) from the half space cooling model (dashed line) and the plate model (solid line) are plotted for reference. The observed depths of the two discontinuities show significant local variations. The average depths of the LAB and the 220-km discontinuity are at 120 km and 255 km, independent of seafloor age. The depth uncertainties estimated from frequency-dependent measurements are plotted as error bars.

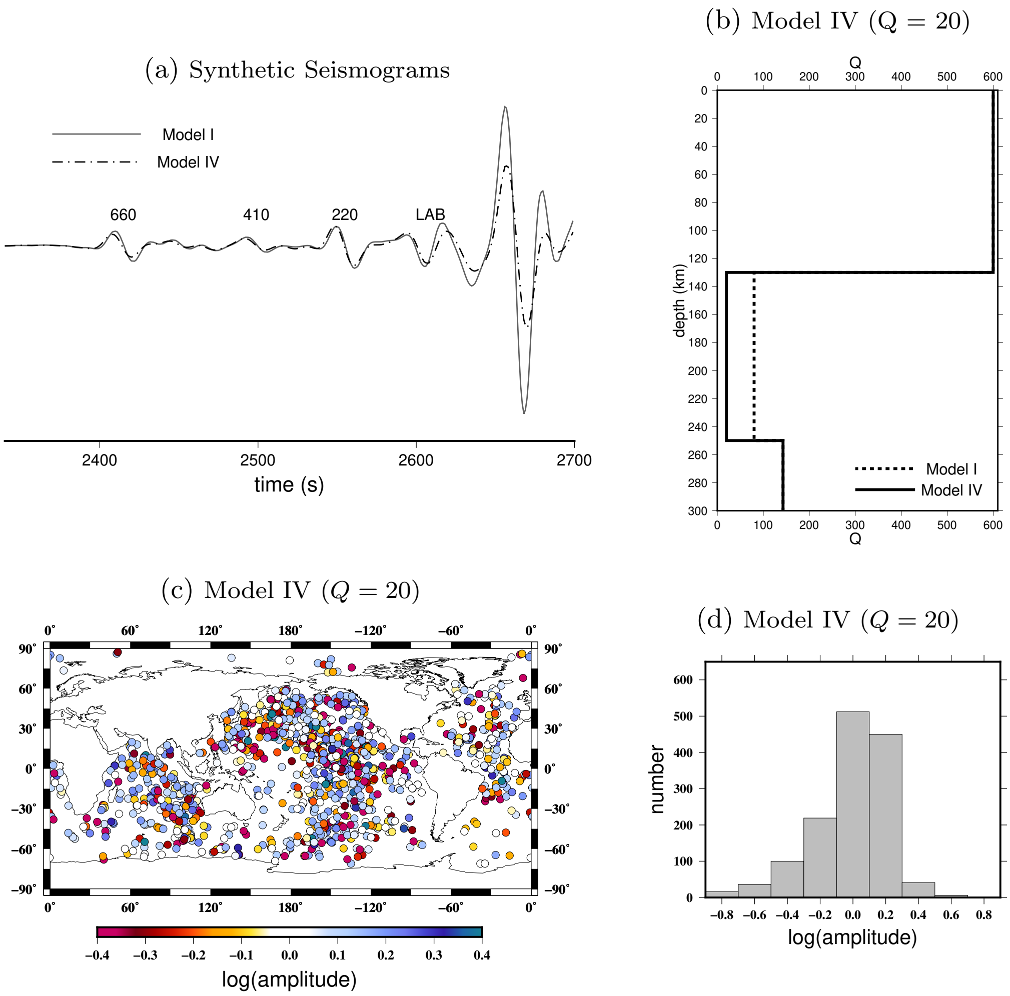

Figure 10: (a) Synthetic seismograms calculate for Model I and Model IV as in Fig. 3. (b) Q structure in the 1-D reference models Model I and Model IV. Model IV is identical to Model I in velocity and density but has a much smaller Q value (Q=20) in the asthenosphere than in Model I (Q=80). The amplitude of the main SS wave becomes smaller in Model IV synthetics due to the overall stronger attenuation associated with the lower Q value in the asthenosphere but its impact on the amplitude of the SS precursor $S_{\mathrm{LAB}}S$ is very limited. This is because anelasticity also reduces the effective wave speed in the low Q region. Therefore, velocity contrast across the LAB increases, resulting a larger reflection coefficient which increases the amplitude of the $S_{\mathrm{LAB}}S$ wave. The observed large amplitudes of the $S_{\mathrm{LAB}}S$ waves therefore can not be fully explained by a reduction of Q values in the asthenosphere.

Acknowledgments

We thank the Editor Dr. Douglas Schmitt, the Associate Editor and an anonymous reviewer for their constructive comments, which helped improve the manuscript. The facilities of the IRIS Data Management System, and specifically the IRIS Data Management Center, were used for access to waveform and metadata required in this study. The authors acknowledge Advanced Research Computing at Virginia Tech for providing computational resources and technical support. This research was supported by the US National Science Foundation under Grant EAR-2017218.

Data Availability Statement

Raw seismic waveforms used in this study are available from the IRIS platform (https://ds.iris.edu/ds/nodes/dmc/). All GSN stations were used (Network codes are CU, GT, IC, II, IU). Data preparation and preprocessing were performed using the Seismic Analysis Code (https://ds.iris.edu/ds/nodes/dmc/software/downloads/sac/). Figures were made with the Generic Mapping Tools (GMT) package (Wessel & Smith, 1995).

References

Auer, L., Becker, T. W., Boschi, L., & Schmerr, N. (2015). Thermal structure, radial anisotropy, and dynamics of oceanic boundary layers. *Geophysical Research Letters*, *42*(22), 9740–9749.

Beghein, C., Yuan, K., Schmerr, N., & Xing, Z. (2014). Changes in seismic anisotropy shed light on the nature of the gutenberg discontinuity. *Science*, *343*(6176), 1237–1240.

Burgos, G., Montagner, J.-P., Beucler, E., Capdeville, Y., Mocquet, A., & Drilleau, M. (2014). Oceanic lithosphere-asthenosphere boundary from surface wave dispersion data. *Journal of Geophysical Research: Solid Earth*, *119*(2), 1079–1093.

Chantel, J., Manthilake, G., Andrault, D., Novella, D., Yu, T., & Wang, Y. (2016). Experimental evidence supports mantle partial melting in the asthenosphere. *Science Advances*, *2*(5), e1600246. doi: 10.1126/sciadv.1600246

Dahlen, F. (2005). Finite-frequency sensitivity kernels for boundary topography perturbations. *Geophysical Journal International*, *162*(2), 525–540.

Debayle, E., Bodin, T., Durand, S., & Ricard, Y. (2020). Seismic evidence for partial melt below tectonic plates. *Nature*, *586*(7830), 555–559.

Deng, K., & Zhou, Y. (2015). Wave diffraction and resolution of mantle transition zone discontinuities in receiver function imaging. *Geophysical Journal International*, *201*(3), 2008–2025.

Deuss, A., & Woodhouse, J. H. (2002). A systematic search for mantle discontinuities using ss-precursors. *Geophysical Research Letters*, *29*(8), 90–1.

Deuss, A., & Woodhouse, J. H. (2004). The nature of the lehmann discontinuity from its seismological clapeyron slopes. *Earth and Planetary Science Letters*, *225*(3-4), 295–304.

Dziewonski, A. M., & Anderson, D. L. (1981). Preliminary reference earth model. *Physics of the earth and planetary interiors*, *25*(4), 297–356.

Faul, U. H., & Jackson, I. (2005). The seismological signature of temperature and grain size variations in the upper mantle. *Earth and Planetary Science Letters*, *234*(1-2), 119–134.

Fischer, K. M., Ford, H. A., Abt, D. L., & Rychert, C. A. (2010). The lithosphere-asthenosphere boundary. *Annual Review of Earth and Planetary Sciences*, *38*, 551–575.

Fischer, K. M., Rychert, C. A., Dalton, C. A., Miller, M. S., Beghein, C., & Schutt, D. L. (2020). A comparison of oceanic and continental mantle lithosphere. *Physics of the Earth and Planetary Interiors*, 106600.

French, S., Lekic, V., & Romanowicz, B. (2013). Waveform tomography reveals channeled flow at the base of the oceanic asthenosphere. *Science*, *342*(6155), 227–230.

Gaherty, J. B., & Jordan, T. H. (1995). Lehmann discontinuity as the base of an anisotropic layer beneath continents. *Science*, *268*(5216), 1468–1471.

Godfrey, K. E., Dalton, C. A., & Ritsema, J. (2017). Seafloor age dependence of rayleigh wave phase velocities in the indian ocean. *Geochemistry, Geophysics, Geosystems*, *18*(5), 1926–1942.

Goncz, J. H., & Cleary, J. R. (1976). Variations in the structure of the upper mantle beneath australia, from rayleigh wave observations. *Geophysical Journal International*, *44*(2), 507–516.

Gu, Y. J., Dziewonski, A. M., & Ekström, G. (2001). Preferential detection of the lehmann discontinuity beneath continents. *Geophysical Research Letters*, *28*(24), 4655–4658.

Guo, Z., & Zhou, Y. (2020). Finite-frequency imaging of the global 410-and 660-km discontinuities using ss precursors. *Geophysical Journal International*, *220*(3), 1978–1994.

Guo, Z., & Zhou, Y. (2021). Stagnant slabs and their return flows from finite-frequency tomography of the 410-km and 660-km discontinuities. *Journal of Geophysical Research: Solid Earth*, *126*(5), e2020JB021099.

Hales, A., Muirhead, K., & Rynn, J. (1980). A compressional velocity distribution for the upper mantle. *Tectonophysics*, *63*(1-4), 309–348.

Hammond, W. C., & Humphreys, E. D. (2000). Upper mantle seismic wave velocity: Effects of realistic partial melt geometries. *Journal of Geophysical Research: Solid Earth*, *105*(B5), 10975–10986.

Holtzman, B. K. (2016). Questions on the existence, persistence, and mechanical effects of a very small melt fraction in the asthenosphere. *Geochemistry, Geophysics, Geosystems*, *17*(2), 470–484.

James, E. K., Dalton, C. A., & Gaherty, J. B. (2014). Rayleigh wave phase velocities in the a tlantic upper mantle. *Geochemistry, Geophysics, Geosystems*, *15*(11), 4305–4324.

Karato, S.-i. (1992). On the lehmann discontinuity. *Geophysical Research Letters*, *19*(22), 2255–2258.

Karato, S.-i. (2012). On the origin of the asthenosphere. *Earth and Planetary Science Letters*, *321*, 95–103.

Karato, S.-i., & Jung, H. (1998). Water, partial melting and the origin of the seismic low velocity and high attenuation zone in the upper mantle. *Earth and Planetary Science*

Letters, *157*(3-4), 193–207.

Karato, S.-i., & Wu, P. (1993). Rheology of the upper mantle: A synthesis. *Science*, *260*(5109), 771–778.

Kawakatsu, H., Kumar, P., Takei, Y., Shinohara, M., Kanazawa, T., Araki, E., & Suyehiro, K. (2009). Seismic evidence for sharp lithosphere-asthenosphere boundaries of oceanic plates. *Science*, *324*(5926), 499–502.

Kawakatsu, H., & Utada, H. (2017). Seismic and electrical signatures of the lithosphere–asthenosphere system of the normal oceanic mantle. *Annual Review of Earth and Planetary Sciences*, *45*.

Korenaga, T., & Korenaga, J. (2008). Subsidence of normal oceanic lithosphere, apparent thermal expansivity, and seafloor flattening. *Earth and Planetary Science Letters*, *268*(1-2), 41–51.

Laske, G., Masters, G., Ma, Z., & Pasyanos, M. (2013). Update on crust1. 0—a 1-degree global model of earth's crust. In *Geophys. res. abstr* (Vol. 15, p. 2658).

Lehmann, I. (1959). Velocities of longitudinal waves in the upper part of the earth's mantle. In *Annales de géophysique* (Vol. 15, p. 93).

Lehmann, I. (1961). S and the structure of the upper mantle. *Geophysical Journal International*, *4*(Supplement_1), 124–138.

Li, X., Kind, R., Priestley, K., Sobolev, S. V., Tilmann, F., Yuan, X., & Weber, M. (2000). Mapping the hawaiian plume conduit with converted seismic waves. *Nature*, *405*(6789), 938–941.

Li, X., Kind, R., Yuan, X., Wölbern, I., & Hanka, W. (2004). Rejuvenation of the lithosphere by the hawaiian plume. *Nature*, *427*(6977), 827–829.

Liu, K., & Zhou, Y. (2016). Travelling-wave green tensor and near-field rayleigh-wave sensitivity. *Geophysical Supplements to the Monthly Notices of the Royal Astronomical Society*, *205*(1), 134–145.

Ma, Z., & Dalton, C. A. (2019). Evidence for dehydration-modulated small-scale convection in the oceanic upper mantle from seafloor bathymetry and rayleigh wave phase velocity. *Earth and Planetary Science Letters*, *510*, 12–25.

Maggi, A., Debayle, E., Priestley, K., & Barruol, G. (2006). Multimode surface waveform tomography of the pacific ocean: a closer look at the lithospheric cooling signature. *Geophysical Journal International*, *166*(3), 1384–1397.

Mehouachi, F., & Singh, S. C. (2018). Water-rich sublithospheric melt channel in the equatorial atlantic ocean. *Nature Geoscience*, *11*(1), 65–69.

Nettles, M., & Dziewoński, A. M. (2008). Radially anisotropic shear velocity structure of the upper mantle globally and beneath north america. *Journal of Geophysical Research: Solid Earth*, *113*(B2).

Ni, H., Keppler, H., & Behrens, H. (2011). Electrical conductivity of hydrous basaltic melts: implications for partial melting in the upper mantle. *Contributions to Mineralogy and Petrology*, *162*(3), 637–650.

Parsons, B., & Sclater, J. G. (1977). An analysis of the variation of ocean floor bathymetry and heat flow with age. *Journal of geophysical research*, *82*(5), 803–827.

Revenaugh, J., & Jordan, T. H. (1991). Mantle layering from scs reverberations: 3. the upper mantle. *Journal of Geophysical Research: Solid Earth*, *96*(B12), 19781–19810.

Richards, F., Hoggard, M., Crosby, A., Ghelichkhan, S., & White, N. (2020). Structure and dynamics of the oceanic lithosphere-asthenosphere system. *Physics of the Earth and Planetary Interiors*, 106559.

Richter, F. M. (1973). Convection and the large-scale circulation of the mantle. *Journal of Geophysical Research*, *78*(35), 8735–8745.

Richter, F. M., & Parsons, B. (1975). On the interaction of two scales of convection in the mantle. *Journal of Geophysical Research*, *80*(17), 2529–2541.

Ritsema, J., Deuss, a. A., Van Heijst, H., & Woodhouse, J. (2011). S40rts: a degree-40 shear-velocity model for the mantle from new rayleigh wave dispersion, teleseismic traveltime and normal-mode splitting function measurements. *Geophysical Journal International*, *184*(3), 1223–1236.

Rost, S., & Weber, M. (2001). A reflector at 200 km depth beneath the northwest pacific. *Geophysical Journal International*, *147*(1), 12–28.

Rychert, C. A., Harmon, N., Constable, S., & Wang, S. (2020). The nature of the lithosphere-asthenosphere boundary. *Journal of Geophysical Research: Solid Earth*, *125*(10), e2018JB016463.

Rychert, C. A., Schmerr, N., & Harmon, N. (2012). The pacific lithosphere-asthenosphere boundary: Seismic imaging and anisotropic constraints from ss waveforms. *Geochemistry, Geophysics, Geosystems*, *13*(9).

Rychert, C. A., & Shearer, P. M. (2009). A global view of the lithosphere-asthenosphere boundary. *Science*, *324*(5926), 495–498.

Rychert, C. A., & Shearer, P. M. (2011). Imaging the lithosphere-asthenosphere boundary beneath the pacific using ss waveform modeling. *Journal of Geophysical Research: Solid Earth*, *116*(B7).

Rychert, C. A., Tharimena, S., Harmon, N., Wang, S., Constable, S., Kendall, J. M., . . . Schlaphorst, D. (2021). A dynamic lithosphere–asthenosphere boundary near the equatorial mid-atlantic ridge. *Earth and Planetary Science Letters*, *566*, 116949.

Sacks, I., Snoke, J., & Husebye, E. (1979). Lithosphere thickness beneath the baltic shield. *Tectonophysics*, *56*(1-2), 101–110.

Schmerr, N. (2012). The gutenberg discontinuity: Melt at the lithosphere-asthenosphere boundary. *Science*, *335*(6075), 1480–1483.

Schmerr, N., & Garnero, E. (2006). Investigation of upper mantle discontinuity structure beneath the central pacific using ss precursors. *Journal of Geophysical Research: Solid Earth*, *111*(B8).

Shearer, P. M. (1991). Constraints on upper mantle discontinuities from observations of long-period reflected and converted phases. *Journal of Geophysical Research: Solid Earth*, *96*(B11), 18147–18182.

Stern, T., Henrys, S. A., Okaya, D., Louie, J. N., Savage, M. K., Lamb, S., . . . Iwasaki, T. (2015). A seismic reflection image for the base of a tectonic plate. *Nature*, *518*(7537), 85–88.

Team, T. M. S. (1998). Imaging the deep seismic structure beneath a mid-ocean ridge: The melt experiment. *Science*, *280*(5367), 1215–1218.

Tharimena, S., Rychert, C., Harmon, N., & White, P. (2017). Imaging pacific lithosphere seismic discontinuities—insights from ss precursor modeling. *Journal of Geophysical Research: Solid Earth*, *122*(3), 2131–2152.

Turcotte, D., & Oxburgh, E. (1967). Finite amplitude convective cells and continental drift. *Journal of Fluid Mechanics*, *28*(1), 29–42.

Turcotte, D. L., & Schubert, G. (2002). *Geodynamics*. Cambridge university press.

Vidale, J. E., & Benz, H. M. (1992). Upper-mantle seismic discontinuities and the thermal structure of subduction zones. *Nature*, *356*(6371), 678–683.

Wang, S., Constable, S., Rychert, C. A., & Harmon, N. (2020). A lithosphere-asthenosphere boundary and partial melt estimated using marine magnetotelluric data at the central middle atlantic ridge. *Geochemistry, Geophysics, Geosystems*, *21*(9), e2020GC009177.

Wessel, P., & Smith, W. H. F. (1995). New version of the generic mapping tools released. *Eos Trans. AGU*, *76*, 329.

Xue, J., Zhou, Y., & Chen, Y. J. (2015). Tomographic resolution of plume anomalies in the lowermost mantle. *Geophysical Journal International*, *201*(2), 979–995.

Yamauchi, H., & Takei, Y. (2016). Polycrystal anelasticity at near-solidus temperatures. *Journal of Geophysical Research: Solid Earth*, *121*(11), 7790–7820.

Zhou, Y. (2009). Multimode surface wave sensitivity kernels in radially anisotropic earth media. *Geophysical Journal International*, *176*(3), 865–888.

Zhou, Y., Dahlen, F., Nolet, G., & Laske, G. (2005). Finite-frequency effects in global surface-wave tomography. *Geophysical Journal International*, *163*(3), 1087–1111.

Zhou, Y., Nolet, G., Dahlen, F. A., & Laske, G. (2006). Global upper-mantle structure from finite-frequency surface-wave tomography. *Journal of Geophys. Res.*, *111*, doi:10.1029/2005JB003677.

Supporting Information for "Age-Independent Oceanic Plate Thickness and Asthenosphere Melting from SS Precursor Imaging"

Shuyang Sun and Ying Zhou

Department of Geosciences, Virginia Tech, Blacksburg, VA 24061, USA

This Supplementary Information includes 15 Figures (Figure S1-S15) and 1 Table (Table S1).

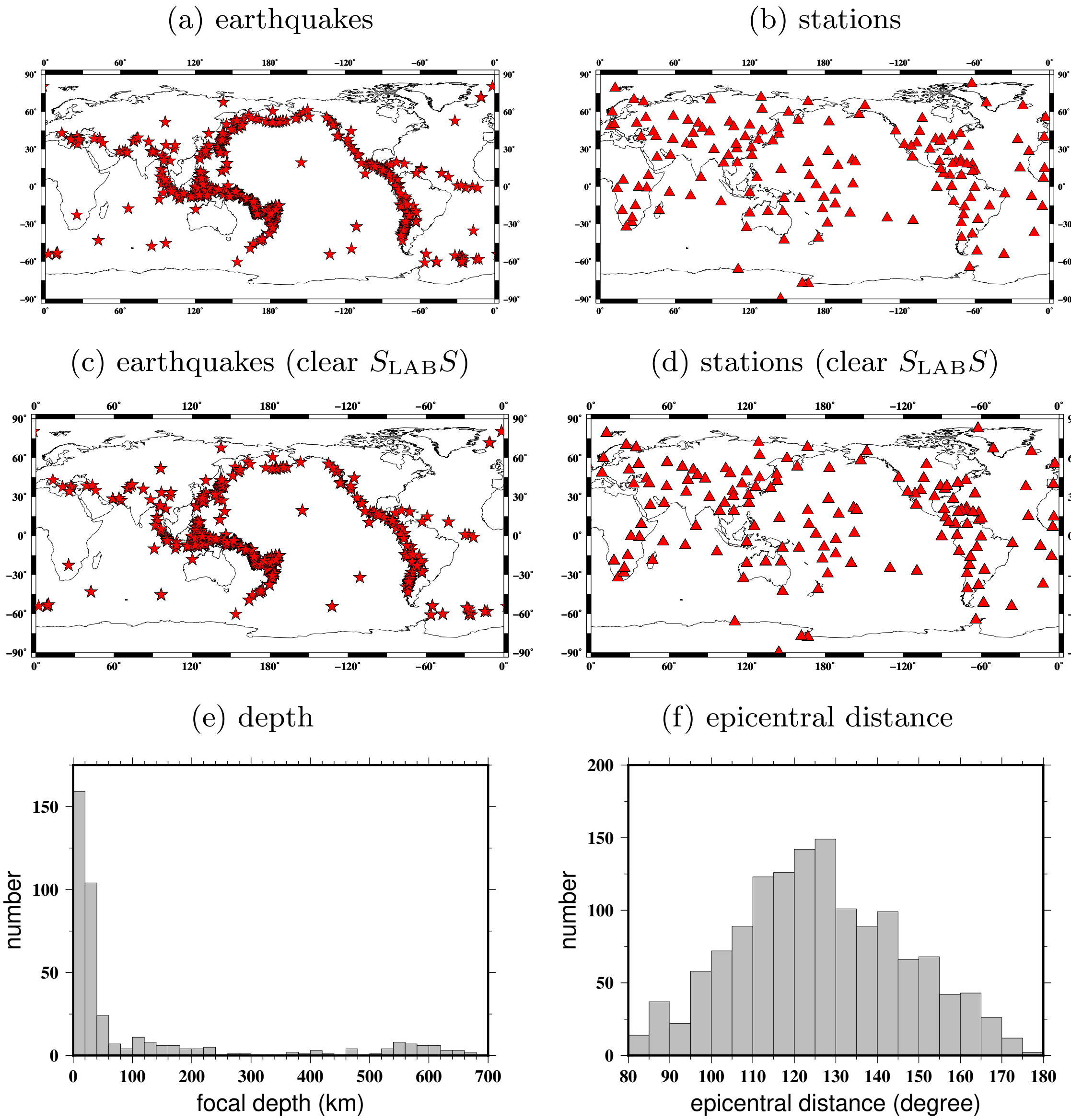

Figure S1: (a) and (b) are distributions of the 543 earthquakes and 151 GSN stations used in this study. (c) and (d) are distributions of the 395 earthquakes and 144 GSN stations in the subset in which large $S_{\mathrm{LAB}}S$ waves were observed. (e) and (f) are histograms of the focal depths and epicentral distances of the same subset.

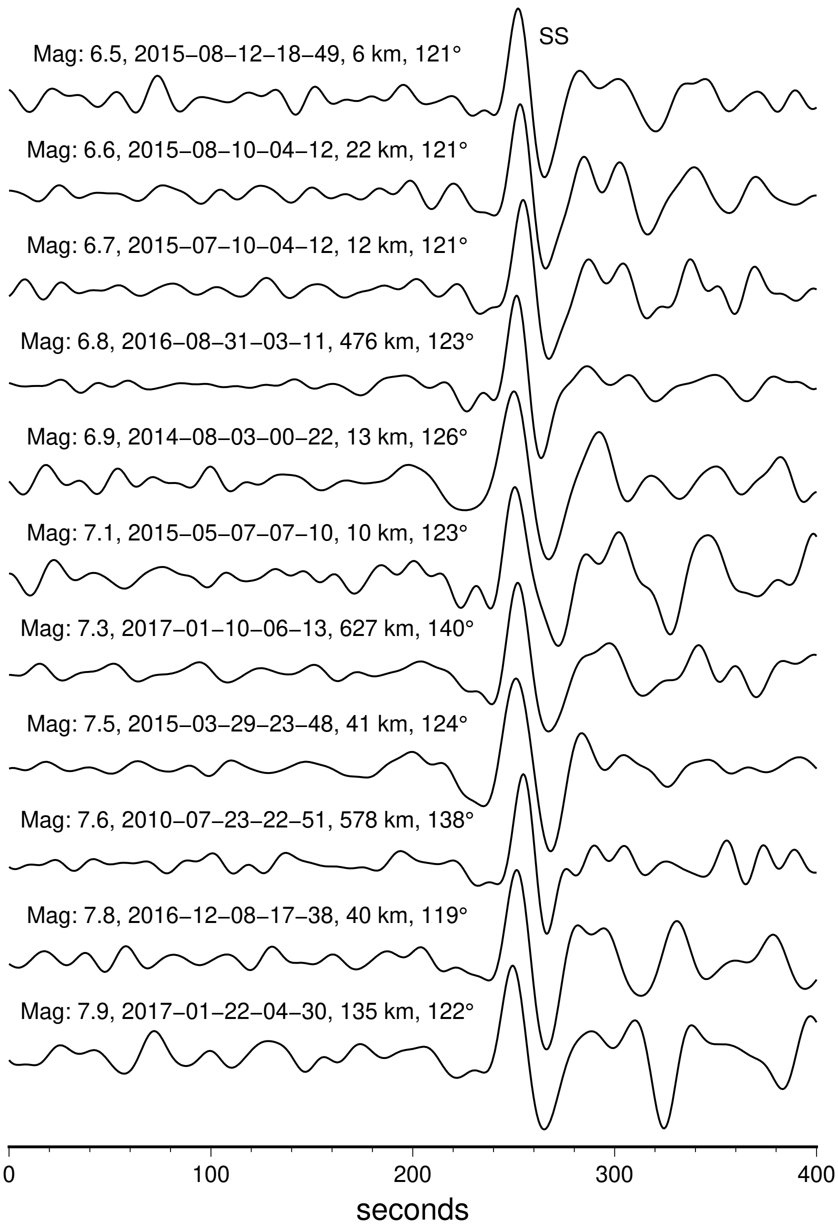

Figure S2: Example SS seismograms with simple source time functions recorded at a GSN station DWPF (https://doi.org/10.7914/SN/IU) for earthquakes with different magnitudes ranging from 6.5 to 7.9. The event magnitude, date/time, depth and epicentral distance are denoted. The SS waves have been aligned with polarities corrected for better illustration. The dataset used in this study includes 6,143 high-quality SS seismograms with bounce points in oceanic regions.

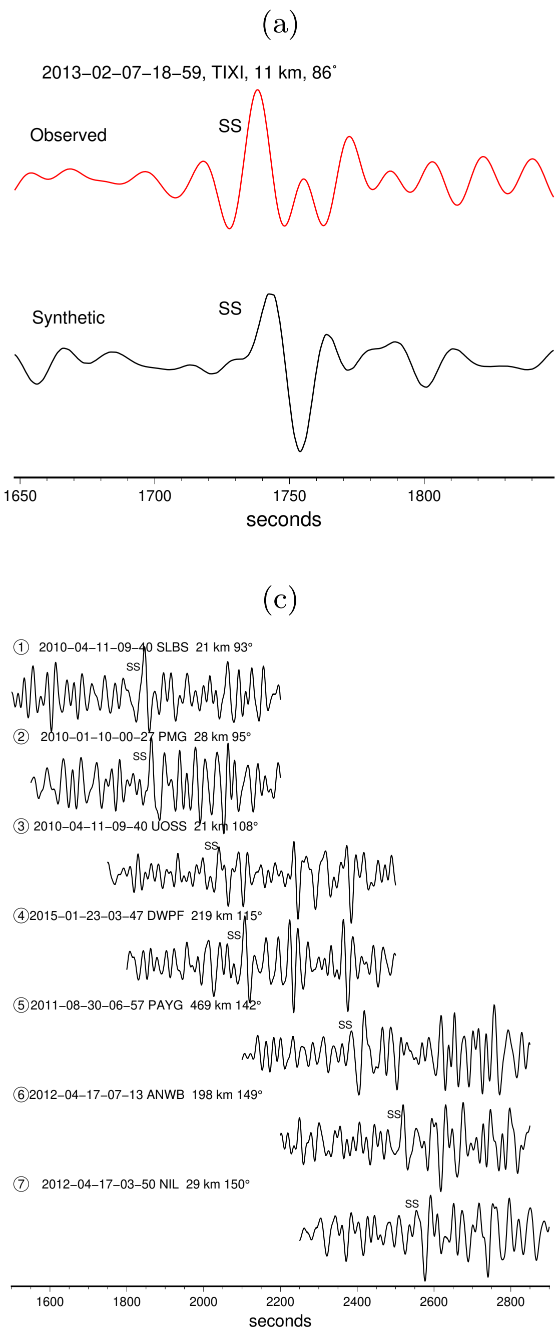

Figure S3: (a) and (b) are example seismograms with SS waves significantly different from the synthetics. SS precursors on those seismograms are not used in this study. (c) example seismograms with noisy SS waves and precursors, SS precursors on those seismograms are not used in this study. (d) example seismograms with clear SS precursors but weak (or absent) $S_{\mathrm{LAB}}S$ waves, their bounce points are plotted in Fig. 2.

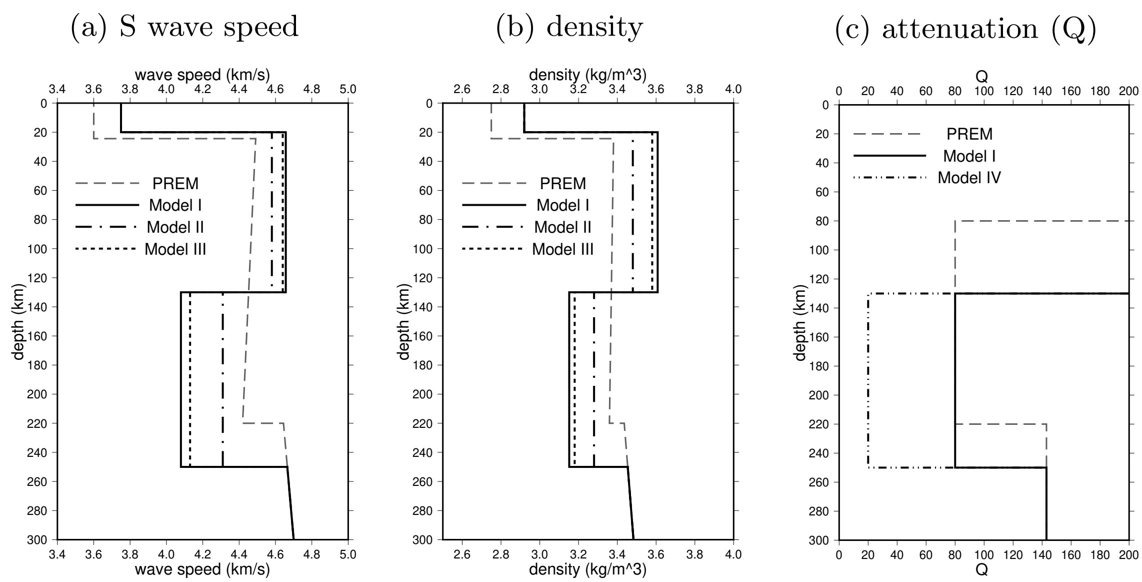

Figure S4: 1-D reference earth models used in this study: PREM, Models I, II, III and IV. (a) S-wave speed profiles. The velocity contrast across the LAB is 12.5% in Model I, 6% in Model II and 11% in Model III. (b) density profiles of the models. The density is scaled with velocity in the uppermost 250 km in Models I-IV , with a scaling parameter of ∼0.77, similar to that in PREM, which varies between 0.75 and 0.78. (c) Seismic Q profiles of the models. $Q = 80$ in Model I at depths between 130 and 250 km and $Q = 20$ in Model IV at those depths. PREM Q values are plotted as the dashed line for reference.

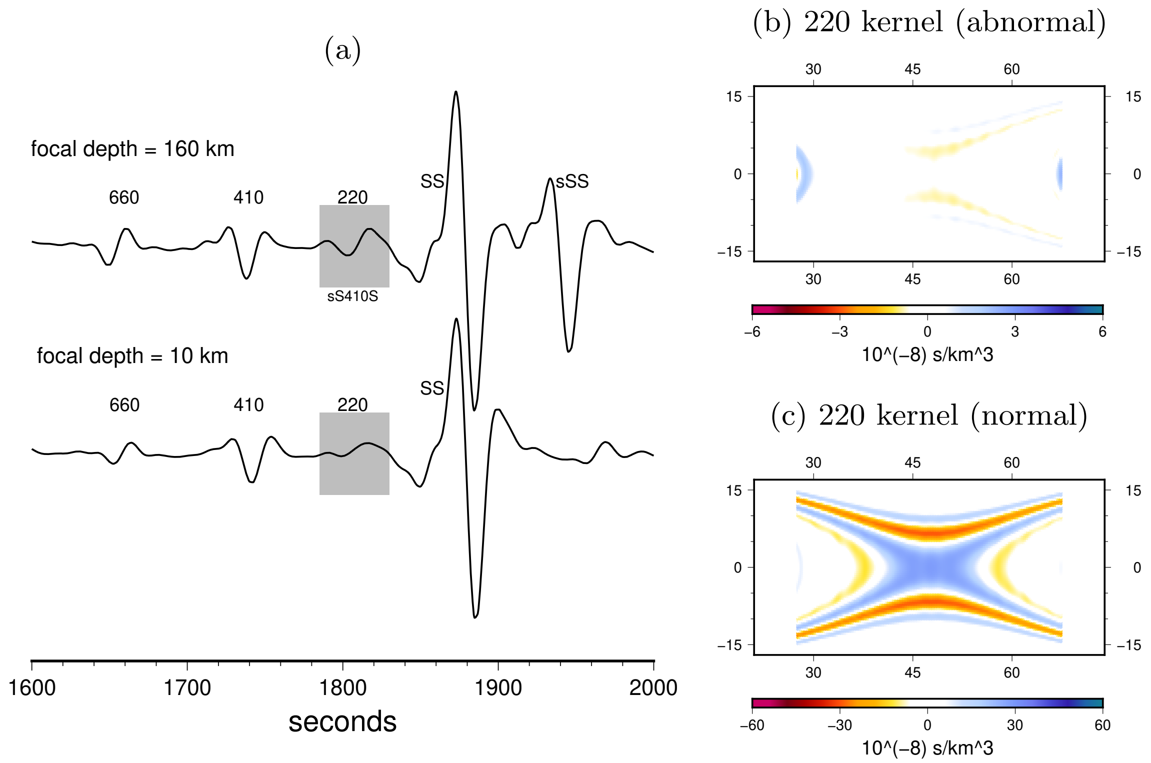

Figure S5: (a) example seismograms with (top) and without (bottom) an interfering depth phase. The measurement windows (shaded) are centered at the expected arrival of the $S_{220}S$ waves. The epicentral distance is 96° and the depths of the earthquakes are denoted on each seismogram. The SS waves have been aligned and a strong depth phase sSS arrives after the main SS wave for the deep earthquake (depth=160 km). The precursor of the depth phase $sS_{410}S$ arrives about the same time as the the SS precursor $S_{220}S$. The calculated sensitivity kernel is abnormal when there is $sS_{410}S$ interference – the sensitivity is about 10 times smaller than values expected for an $S_{220}S$ wave. This is because the $sS_{410}S$ wave is not reflected at the 220-km discontinuity and therefore it has no sensitivity to depth perturbations of the 220-km discontinuity at the bounce point.

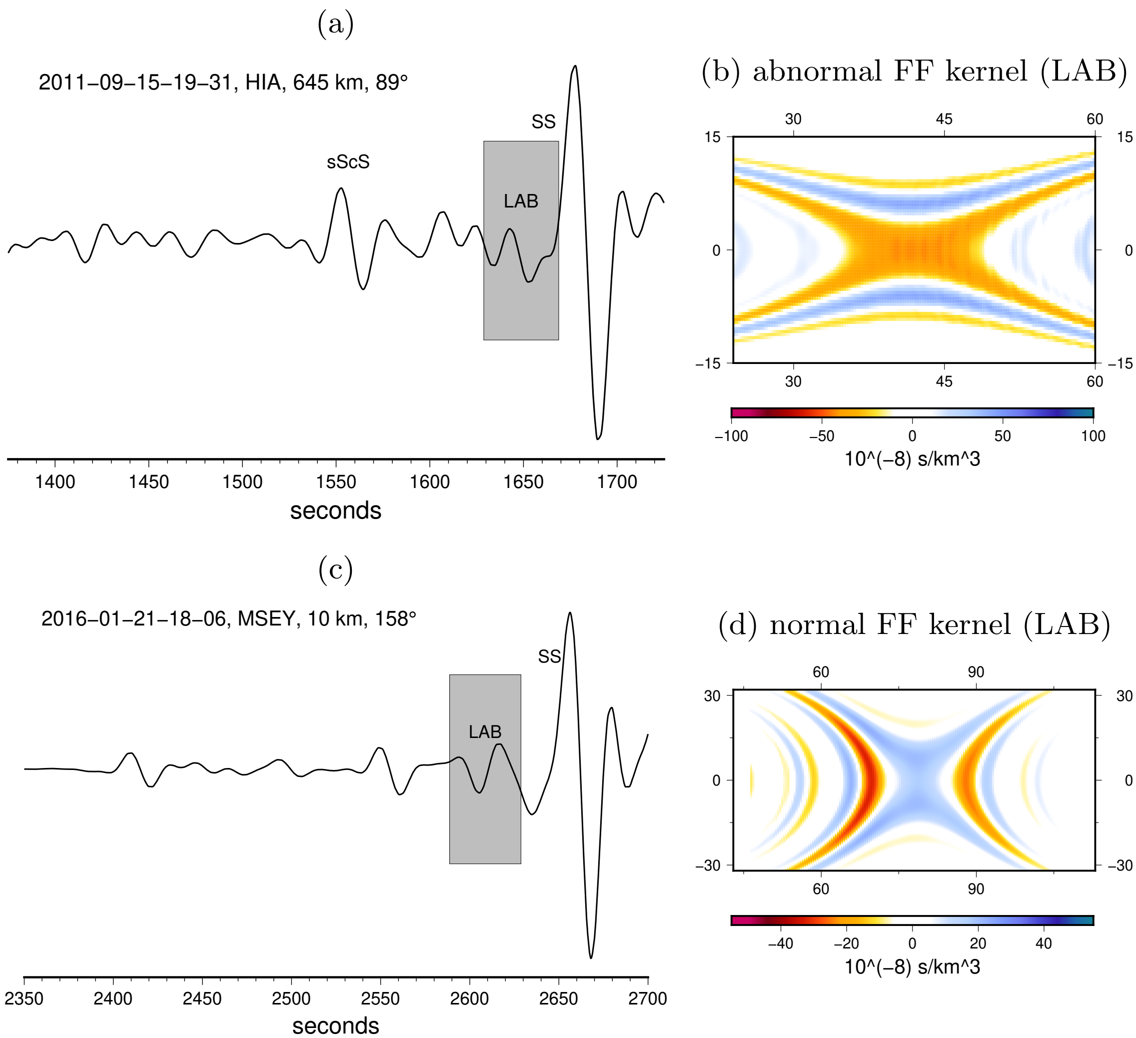

Figure S6: Example traveltime sensitivity kernels with (top) and without (bottom) phase interference. (a) and (c) are synthetic seismograms with measurement windows (shaded) centered at the expected arrival of the $S_{\mathrm{LAB}}S$ waves, and (b) and (d) are the corresponding traveltime sensitivity kernels. (c) and (d) are the same as in Fig. 4 (a) and (b). The interferences between the $S_{\mathrm{LAB}}S$ and $sScS$ coda waves (shallow multiples) in the measurement window in (a) result in a polarity change in the traveltime sensitivity in (b). The sensitivity kernels are always associated with measurement time windows not any particular seismic phases, and the kernels are used to identify possible phase interferences in measurement windows.

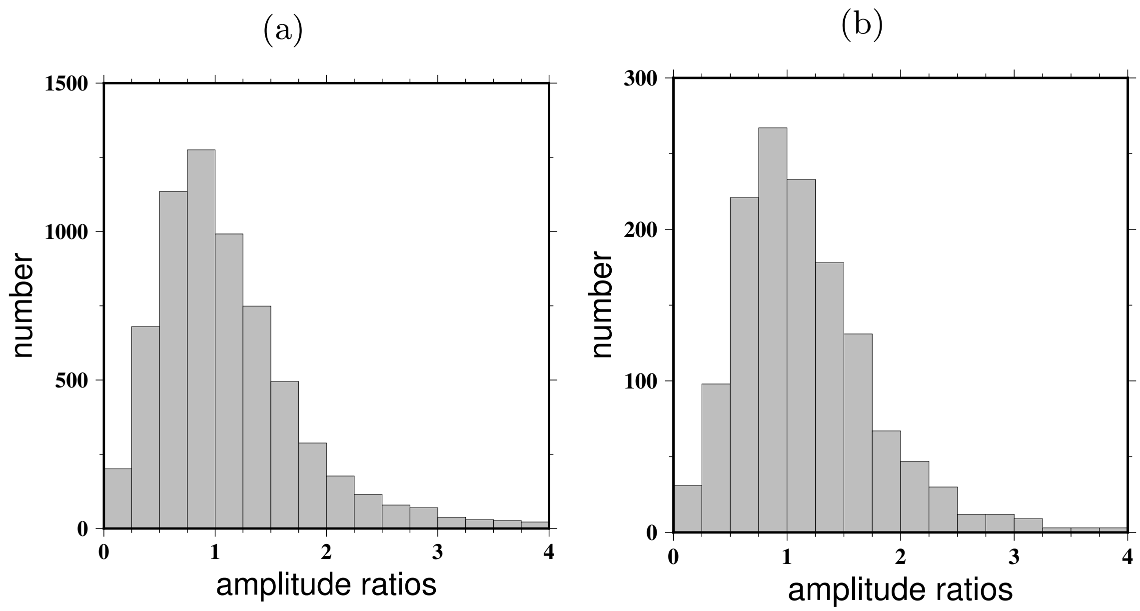

Figure S7: (a) histogram of amplitude ratios between the observed and the synthetic SS waves for the entire dataset (6143 seismograms). (b) the same as (a) but for the subset (1380 seismograms) in which anomalously large $S_{\mathrm{LAB}}S$ were observed. The distribution of the SS amplitude measurements is very similar in (a) and (b), indicating that the observed large amplitudes of the $S_{\mathrm{LAB}}S$ waves in the subset are not a result of focusing caused by mantle heterogeneities because the focusing effects (anomalously large amplitudes) are not observed on the SS waves which travel through the same regions in the mantle sampled by the $S_{\mathrm{LAB}}S$ waves.

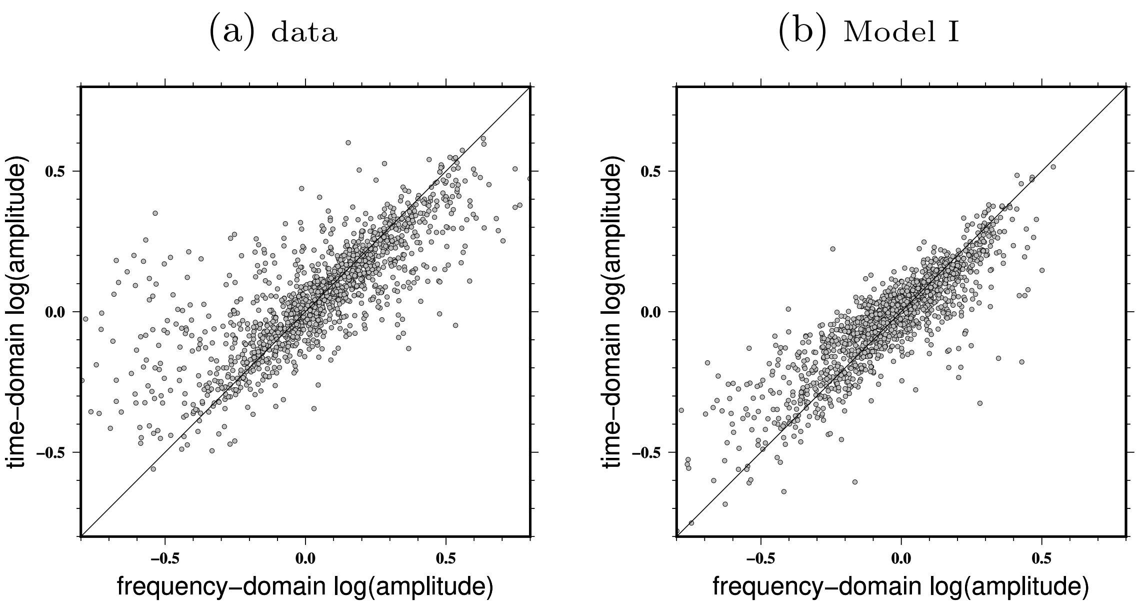

Figure S8: Scatter plots of the LAB amplitude measurements made in the frequency domain versus those obtained in the time domain using envelope functions of the observed seismograms. (b) is the same as (a) but for measurements made on synthetic seismograms calculated for Model I. It is worth noting that the frequency-domain measurements are made at a period of 25 seconds while the envelope functions include much broader frequency content. In this paper, we focus on measurements at a period of 25 seconds, and the envelope function results are plotted for reference only. The 45° line with a slope of 1.0 is also plotted for reference only, it is not expected to be the best fitting line for the scatter plots.

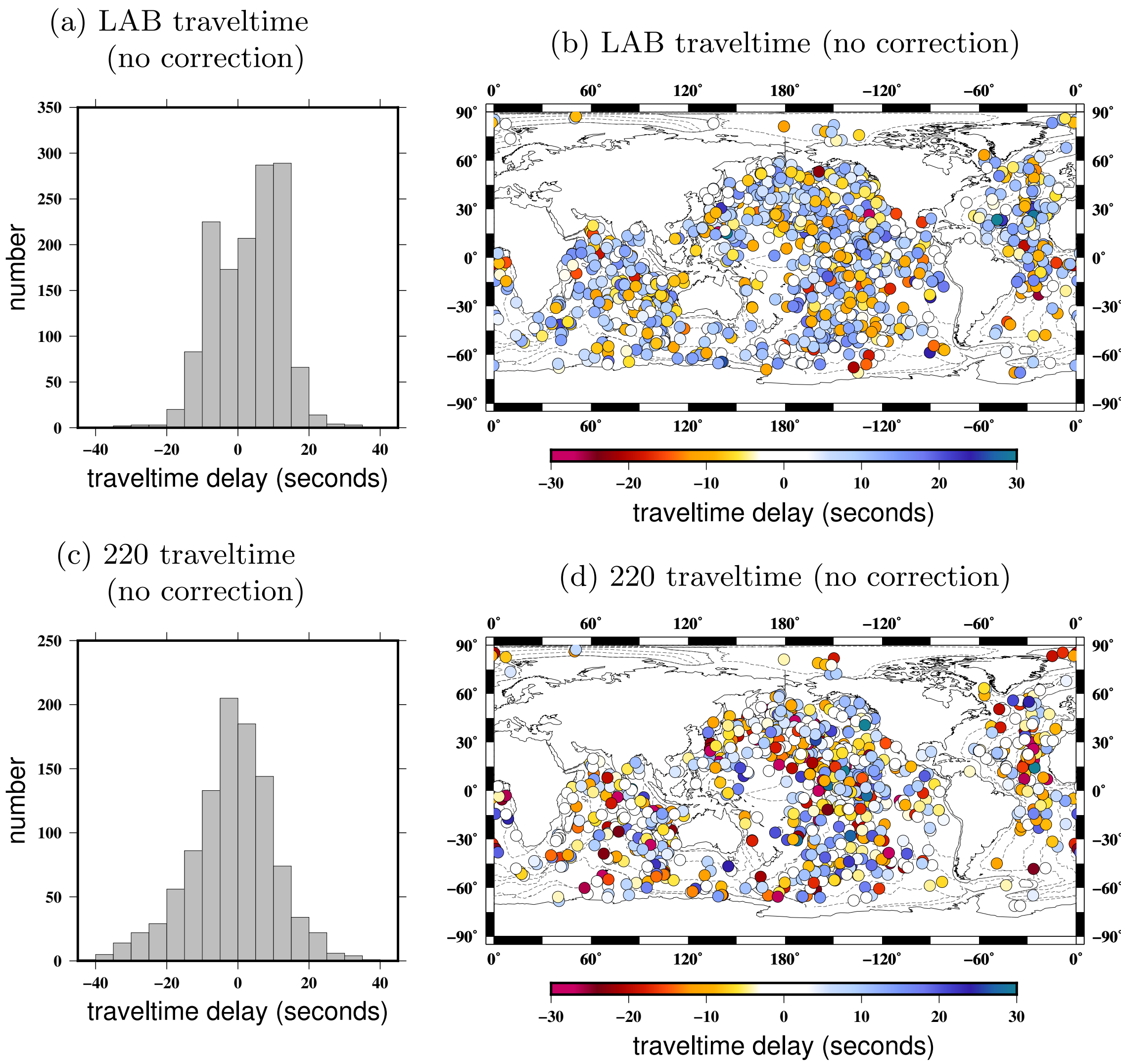

Figure S9: The same as Fig. 7 but for traveltime measurements made without 3-D crustal and mantle corrections.

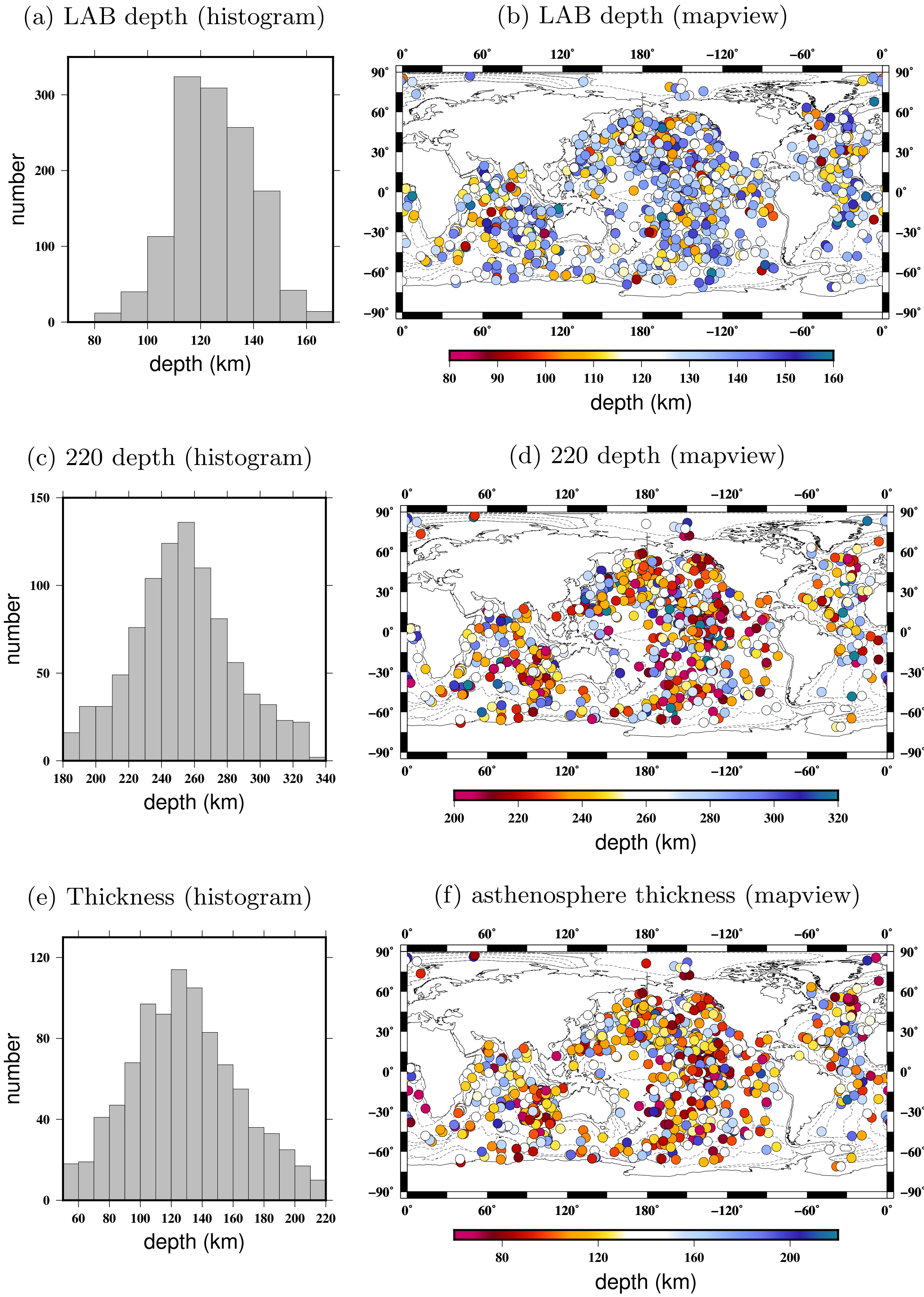

Figure S10: The same as Fig. 8 but for depths of the LAB and the 220-km discontinuity obtained using traveltime measurements without 3-D crust and mantle corrections.

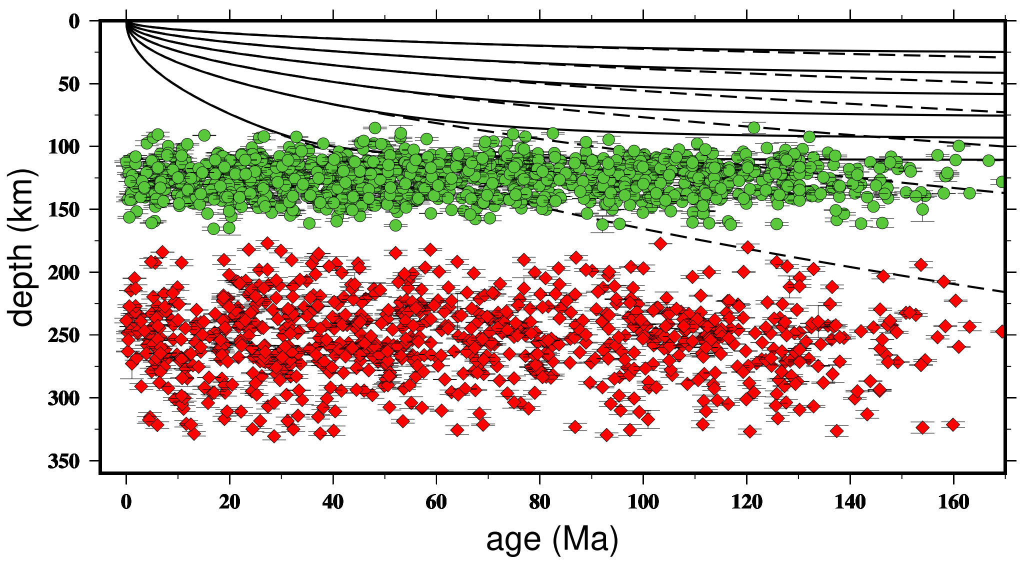

Figure S11: The same as Fig. 9 but for depths of the LAB and the 220-km discontinuity obtained using traveltime measurements without 3-D crust and mantle corrections.

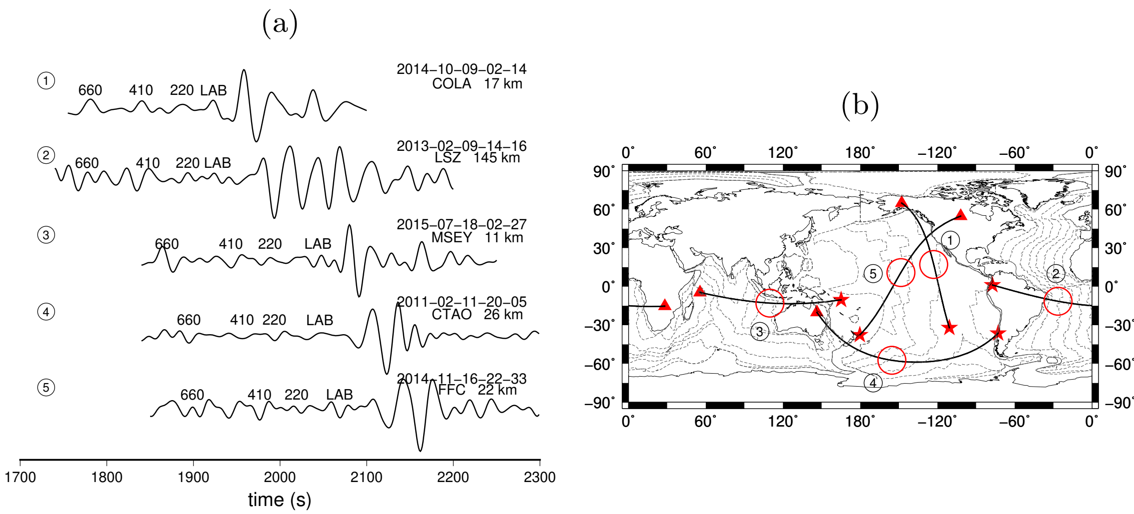

Figure S12: (a), example radial-component seismograms with large-amplitude SS precursors. The corresponding geographic ray paths are plotted in (b).

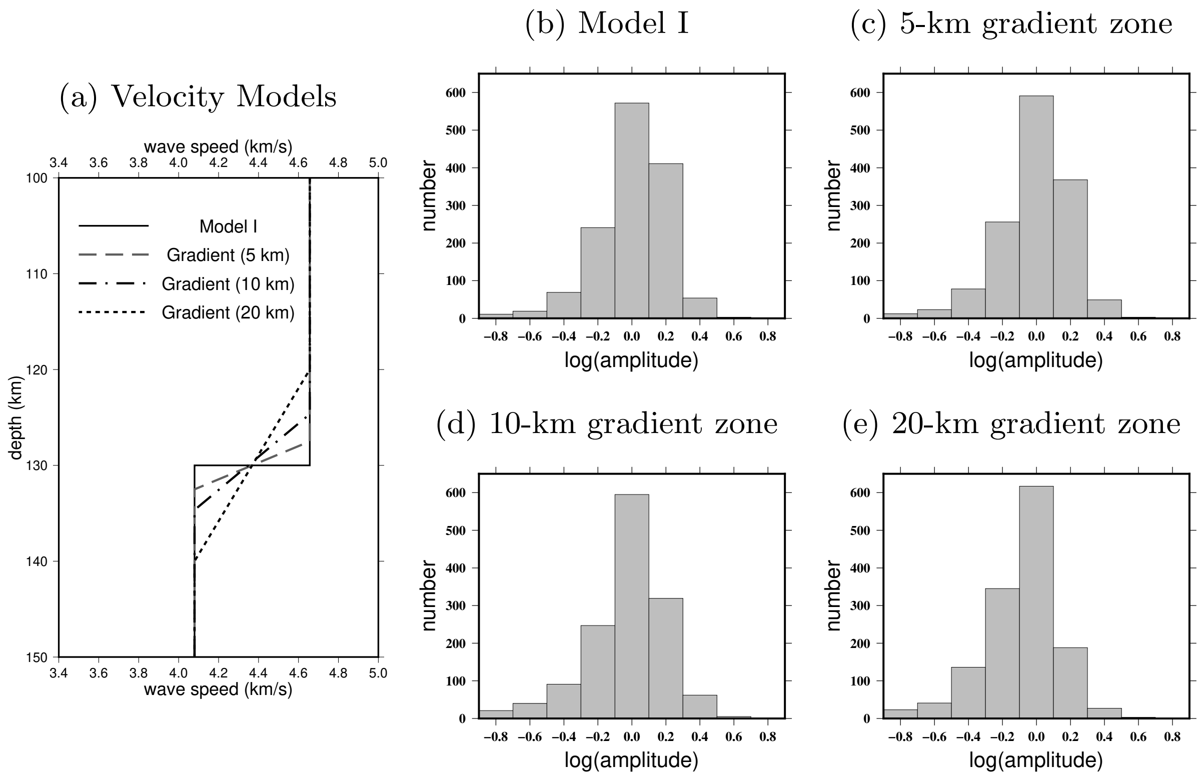

Figure S13: (a) velocity models with a 12.5% of velocity change across the LAB at a depth of 130 km over a first-order discontinuity (Model I) as well as a gradient zone of 5 km, 10 km and 20 km. (b), (c), (d) and (e) are the corresponding histograms of the amplitude measurements γ = minimum $[\log(A_{S_{\mathrm{LAB}}S}/A_{S_{410}S}), \log(A_{S_{\mathrm{LAB}}S}/A_{S_{660}S})]$ made on the synthetic seismograms calculated for the four reference models as in Fig. 6. The $S_{\mathrm{LAB}}S$ amplitudes become smaller when the velocity change occurs over a gradient zone. The average amplitude difference between a first-order discontinuity and a 5-km gradient zone for this dataset is about 2%, and it is about 6% if the velocity change occurs over a 10-km gradient zone. For a gradient zone over a depth range of 20 km, the mean $S_{\mathrm{LAB}}S$ amplitude is about 17% smaller than that for a first-order discontinuity, and the overall amplitude distribution also becomes significantly different. The calculations suggest that a 12.5% velocity change over a gradient zone of 5 km or less can explain the observed amplitude data in Fig. 6.

(a) (b)

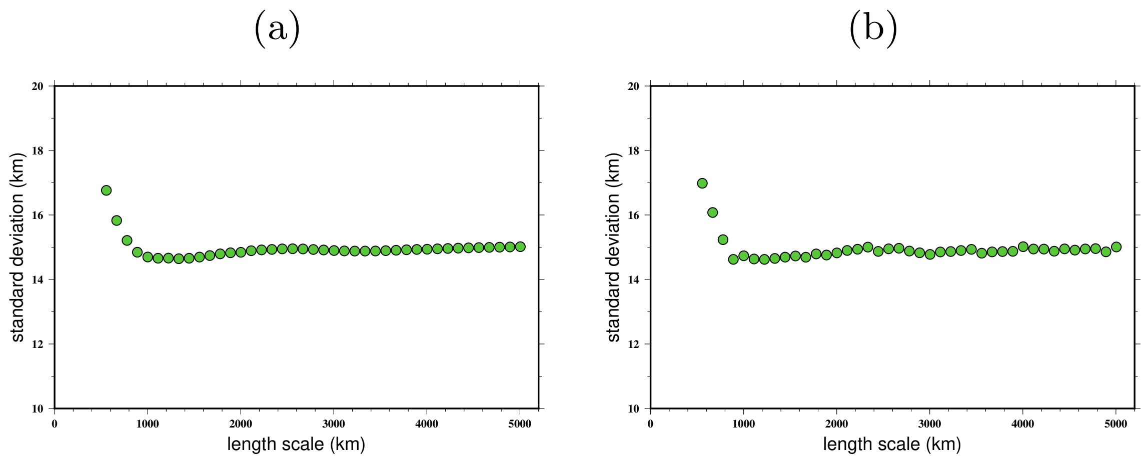

Figure S14: (a) standard deviation at different length scales calculated for the LAB depths obtained in this study. The LAB depths are plotted in histogram and mapview in Fig. 8 (a) and (b). The average standard deviations of the LAB depth are calculated for moving square cells over the global surface, plotted as a function of the length of the cell. The center of the cell moves at a one degree interval in latitude and longitude directions. Only cells that contain more than 30 data points are used in the calculation. (b) same as (a) but calculated for moving cells that are not overlapping.

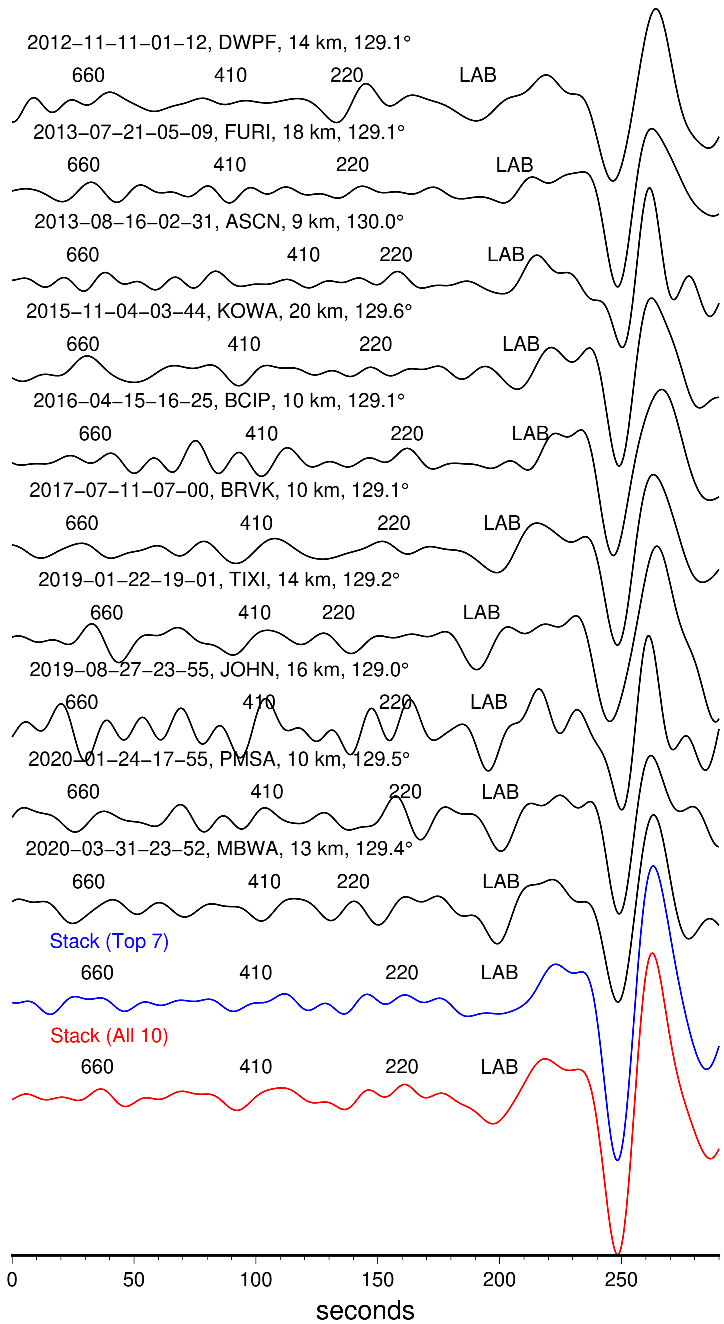

Figure S15: A simple example illustrating the concept the large amplitudes of SS precursors may not be picked up in stacking results when large variations in SS precursor amplitudes and arrival times are present. The black seismograms are observed data with close epicentral distances between 129° and 130°. In a 1-D earth model, the SS precursors arrive at about the same time when the SS waves are aligned (with arrival time differences less than 0.2 seconds). We align the SS waves and produce a stack using only the top seven seismograms (blue) and a second stack using all ten seismograms (red). The SS precursors on the two stacked seismograms are significantly different.

Table S1: Supplementary information of the 1380 $S_{\rm LAB}S$ amplitude measurements (see main text). The amplitudes are measured as $\gamma = \text{minimum}[\log(A_{S_{\rm LAB}S}/A_{S_{410}S}), \log(A_{S_{\rm LAB}S}/A_{S_{660}S})]$. The columns are measurement index, $S_{\rm LAB}S$ bounce-point longitude and latitude, $S_{\rm LAB}S$ amplitude measurement (γ), earthquake date (year-month-day), longitude and latitude as well as the name of the station recorded the $S_{\rm LAB}S$ wave.

Measurement Index	Bounce Point (Longitude°)	Bounce Point (Latitude°)	$S_{\rm LAB}S$ Amplitude	Earthquake Date	Earthquake (Longitude°)	Earthquake (Latitude°)	Station Name
1	-150.3	19.0	-0.0	2009-01-03	133.3	-0.7	SDV
2	177.9	38.5	0.1	2009-01-03	133.3	-0.7	RSSD
3	172.9	32.4	-0.1	2009-01-03	133.3	-0.7	COR
4	-152.6	-0.8	0.3	2009-01-03	133.3	-0.7	OTAV
5	-172.5	21.1	0.1	2009-01-03	133.3	-0.7	SLBS
6	-135.0	-52.3	-0.0	2009-01-15	170.6	-22.4	TRQA
7	107.8	-38.5	-0.0	2009-01-15	170.6	-22.4	ABPO
8	109.8	-24.1	0.0	2009-01-15	170.6	-22.4	MSEY
9	98.8	-27.6	-0.2	2009-01-15	170.6	-22.4	KMBO
10	144.5	14.8	0.1	2009-01-15	170.6	-22.4	ULN
11	100.5	-16.1	0.3	2009-01-15	170.6	-22.4	FURI
12	-149.9	0.8	0.3	2009-01-15	170.6	-22.4	SLBS
13	-134.7	-52.4	-0.0	2009-01-19	170.9	-22.6	TRQA
14	109.8	-24.4	0.2	2009-01-19	170.9	-22.6	MSEY
15	98.8	-28.0	0.4	2009-01-19	170.9	-22.6	KMBO
16	135.8	19.5	0.1	2009-01-19	170.9	-22.6	KURK
17	100.5	-16.5	0.4	2009-01-19	170.9	-22.6	FURI
18	165.3	-59.0	0.0	2009-02-11	126.4	3.9	PLCA
19	172.0	44.6	0.0	2009-02-11	126.4	3.9	RSSD
20	-171.5	49.2	-0.0	2009-02-11	126.4	3.9	DWPF
21	-90.1	-24.5	-0.2	2009-02-18	-176.3	-27.4	SACV
22	125.5	17.3	-0.9	2009-02-18	-176.3	-27.4	GNI
23	-167.5	15.4	0.1	2009-02-18	-176.3	-27.4	KDAK
24	-167.2	19.1	-0.2	2009-02-18	-176.3	-27.4	COLA
25	101.6	-28.1	-0.2	2009-02-18	-176.3	-27.4	FURI
26	176.0	46.0	-0.4	2009-02-18	-176.3	-27.4	KONO
27	-130.8	12.1	-0.0	2009-02-18	-176.3	-27.4	HRV
28	-31.1	37.9	0.0	2009-03-06	-1.9	80.3	RCBR
29	-1.6	-4.8	-0.3	2009-03-06	-1.9	80.3	QSPA
30	139.0	27.2	0.3	2009-03-06	-1.9	80.3	TAU
31	85.9	10.7	0.2	2009-03-06	-1.9	80.3	CASY
32	-123.4	13.4	0.1	2009-04-07	151.6	46.0	TRQA
33	155.1	-15.9	-1.1	2009-04-07	151.6	46.0	SBA
34	-6.7	-6.3	-0.1	2009-04-16	-26.9	-60.2	BFO
35	-128.2	-60.5	0.0	2009-04-16	-26.9	-60.2	RAR
36	141.1	-64.4	-0.5	2009-04-16	-26.9	-60.2	PMG
37	4.8	-5.4	0.1	2009-04-16	-26.9	-60.2	KIEV
38	7.3	-3.0	0.1	2009-04-16	-26.9	-60.2	OBN
39	-123.5	13.4	-0.2	2009-04-18	151.4	46.0	TRQA
40	-117.8	29.3	0.4	2009-04-18	151.4	46.0	LVC
41	-122.0	35.0	-0.6	2009-04-18	151.4	46.0	NNA
42	-149.1	14.4	0.5	2009-05-16	-178.8	-31.5	FFC
43	-132.5	7.0	0.1	2009-05-16	-178.8	-31.5	SSPA
44	149.3	10.0	-0.2	2009-05-16	-178.8	-31.5	ULN
45	145.8	46.1	0.0	2009-06-23	153.8	-5.2	KBS

Measurement Index	Bounce Point (Longitude°)	Bounce Point (Latitude°)	$S_{\mathrm{LAB}}S$ Amplitude	Earthquake Date	Earthquake (Longitude°)	Earthquake (Latitude°)	Station Name
46	167.9	51.4	-0.1	2009-06-23	153.8	-5.2	SFJD
47	158.7	45.1	0.2	2009-06-23	153.8	-5.2	ALE
48	96.6	-38.9	0.1	2009-07-15	166.6	-45.8	MSEY
49	175.9	25.4	0.1	2009-08-03	-112.9	29.0	KAPI
50	-165.8	7.0	-0.2	2009-08-03	-112.9	29.0	CTAO
51	-174.7	51.8	0.0	2009-08-03	-112.9	29.0	SSE
52	-177.7	48.1	-0.1	2009-08-03	-112.9	29.0	TATO
53	-175.3	-4.6	0.3	2009-08-03	-112.9	29.0	NWAO
54	80.2	4.6	-0.1	2009-08-09	137.9	33.2	BOSA
55	-136.1	43.1	0.1	2009-08-09	137.9	33.2	OTAV
56	89.8	10.5	-0.3	2009-08-09	137.9	33.2	ABPO
57	-6.1	67.9	0.2	2009-08-09	137.9	33.2	RCBR
58	40.5	-41.5	-0.0	2009-08-10	92.9	14.1	TRQA
59	81.0	4.0	0.1	2009-08-12	140.4	32.8	BOSA
60	70.5	-58.9	-0.1	2009-08-16	99.5	-1.5	EFI
61	88.0	-57.0	0.2	2009-08-16	99.5	-1.5	PMSA
62	99.5	-45.7	-0.5	2009-08-16	99.5	-1.5	QSPA
63	174.2	58.0	0.1	2009-08-17	123.5	23.5	RSSD
64	179.3	81.2	-0.0	2009-08-17	123.5	23.5	BBSR
65	163.0	28.1	0.2	2009-08-17	123.5	23.5	KIP
66	-173.4	44.2	-0.0	2009-08-17	123.5	23.5	SLBS
67	75.0	-20.8	-0.0	2009-08-28	123.4	-7.2	TSUM
68	128.4	-58.6	0.3	2009-08-28	123.4	-7.2	PMSA
69	165.3	51.7	-0.2	2009-08-28	123.4	-7.2	SSPA
70	61.2	-0.8	0.0	2009-08-28	123.4	-7.2	DBIC
71	-161.4	-43.6	-0.0	2009-08-28	123.4	-7.2	NNA
72	80.2	-23.1	-0.3	2009-08-28	123.4	-7.2	LBTB
73	177.2	46.1	0.1	2009-08-30	-172.6	-15.2	KEV
74	156.6	23.4	-0.0	2009-08-30	-172.6	-15.2	TLY
75	104.2	-34.4	-0.7	2009-08-30	-172.6	-15.2	MBAR
76	-131.2	3.4	-0.4	2009-08-30	-172.6	-15.2	TEIG
77	156.6	45.8	-0.1	2009-08-30	-172.6	-15.2	OBN
78	143.8	-2.4	0.3	2009-09-30	99.9	-0.7	KNTN
79	150.9	1.1	0.2	2009-09-30	99.9	-0.7	XMAS
80	159.3	42.6	0.3	2009-10-01	101.5	-2.5	TUC
81	167.0	34.3	0.2	2009-10-01	101.5	-2.5	SLBS
82	171.8	54.9	0.4	2009-10-04	123.4	6.7	WCI
83	141.4	-64.5	0.1	2009-10-04	123.4	6.7	TRQA
84	-164.6	10.5	0.3	2009-10-04	123.4	6.7	PAYG
85	94.9	-46.8	0.2	2009-10-08	165.9	-13.3	TSUM
86	120.3	20.1	-0.1	2009-10-08	165.9	-13.3	ABKT
87	106.2	-53.9	0.2	2009-10-08	165.9	-13.3	SUR
88	133.8	24.6	0.4	2009-10-08	165.9	-13.3	KURK
89	-141.3	-11.2	-0.1	2009-10-08	165.9	-13.3	PAYG
90	-111.6	1.0	-0.6	2009-10-13	-167.0	52.8	EFI
91	-104.8	11.8	-0.1	2009-10-13	-167.0	52.8	TRQA
92	-46.0	51.1	0.5	2009-10-13	-167.0	52.8	ASCN
93	148.0	12.4	0.1	2009-10-13	-167.0	52.8	NWAO
94	165.5	41.7	0.4	2009-10-24	130.4	-6.1	FFC
95	140.6	-59.3	-0.1	2009-10-24	130.4	-6.1	PMSA
96	-153.7	-11.7	-0.5	2009-10-24	130.4	-6.1	OTAV

Measurement Index	Bounce Point (Longitude°)	Bounce Point (Latitude°)	$S_{\mathrm{LAB}}S$ Amplitude	Earthquake Date	Earthquake (Longitude°)	Earthquake (Latitude°)	Station Name
97	65.1	-27.5	-0.0	2009-10-24	130.4	-6.1	SHEL
98	82.6	-30.9	-0.1	2009-10-24	130.4	-6.1	SUR
99	47.5	-41.3	0.2	2009-10-24	130.4	-6.1	RCBR
100	80.8	-16.7	0.1	2009-10-24	130.4	-6.1	LSZ
101	70.4	8.9	0.2	2009-10-30	129.8	29.2	TSUM
102	-155.2	78.0	0.2	2009-10-30	129.8	29.2	BBSR
103	-149.8	36.1	0.1	2009-10-30	129.8	29.2	PAYG
104	-131.8	21.7	-0.2	2009-10-30	129.8	29.2	CPUP
105	-158.0	-25.1	-0.3	2009-11-08	118.6	-8.2	OTAV
106	162.4	31.6	0.0	2009-11-08	118.6	-8.2	COR
107	171.7	25.7	0.3	2009-11-08	118.6	-8.2	PFO
108	174.2	26.7	0.1	2009-11-08	118.6	-8.2	TUC
109	-153.5	8.0	0.4	2009-11-09	178.3	-17.2	PFO
110	137.5	18.5	0.1	2009-11-09	178.3	-17.2	AAK
111	-44.6	24.8	-0.2	2009-11-13	-70.3	-19.4	KONO
112	-128.5	30.2	-0.1	2009-11-13	-70.3	-19.4	MAJO
113	-31.8	37.3	0.5	2009-11-13	-70.3	-19.4	BRVK
114	176.6	26.9	0.1	2009-11-17	-131.4	52.1	PMG
115	-118.3	12.8	0.3	2009-11-17	-131.4	52.1	RPN
116	-52.0	36.0	-0.3	2009-11-17	-131.4	52.1	ASCN
117	-123.5	10.0	0.4	2009-11-24	-174.0	-20.7	BBSR
118	152.7	41.3	0.2	2009-11-24	-174.0	-20.7	OBN
119	93.5	-10.3	0.1	2010-01-03	157.5	-8.7	MBAR
120	-153.1	-47.3	-0.1	2010-01-03	157.5	-8.7	PLCA
121	70.8	-64.1	-0.2	2010-01-03	157.5	-8.7	ASCN
122	-138.8	-46.2	0.5	2010-01-03	157.5	-8.7	CPUP
123	93.4	-10.4	0.1	2010-01-03	157.3	-8.8	MBAR
124	-138.9	-46.4	0.2	2010-01-03	157.3	-8.8	CPUP
125	51.5	-33.9	0.2	2010-01-05	-14.7	-58.2	PALK
126	-84.4	-0.6	0.1	2010-01-05	-14.7	-58.2	KDAK
127	-8.6	-9.4	0.3	2010-01-05	-14.7	-58.2	PAB
128	65.6	-31.0	0.3	2010-01-05	-14.7	-58.2	CHTO
129	86.7	-33.8	0.2	2010-01-05	-14.7	-58.2	TATO
130	-17.5	26.8	0.1	2010-01-05	-14.7	-58.2	BILL
131	135.6	42.3	0.4	2010-01-05	157.6	-9.0	LVZ
132	147.8	34.2	-0.2	2010-01-10	-124.7	40.6	COCO
133	-35.9	29.2	-0.1	2010-01-10	-124.7	40.6	TSUM
134	-142.3	-2.5	-0.4	2010-01-12	-72.5	18.4	CTAO
135	-21.6	2.5	0.1	2010-01-12	-72.5	18.4	LSZ
136	-14.8	83.3	-0.1	2010-01-12	-72.5	18.4	KMI
137	-145.0	72.6	-0.3	2010-01-12	-72.5	18.4	TATO
138	-10.9	42.6	0.0	2010-01-12	-72.5	18.4	UOSS
139	71.5	10.1	-0.2	2010-02-18	130.7	42.6	SUR
140	-145.3	51.9	0.4	2010-02-26	128.4	25.9	BCIP
141	-149.8	48.4	-0.1	2010-02-26	128.4	25.9	JTS
142	104.1	-45.4	0.2	2010-02-26	128.4	25.9	HOPE
143	-152.4	33.8	-0.0	2010-02-26	128.4	25.9	PAYG
144	-143.6	28.8	-0.0	2010-02-26	128.4	25.9	NNA
145	105.3	-49.4	-0.1	2010-03-04	167.2	-13.6	BOSA
146	131.7	38.0	0.0	2010-03-04	167.2	-13.6	OBN
147	102.8	-46.6	0.2	2010-03-04	167.2	-13.6	LBTB

Measurement Index	Bounce Point (Longitude°)	Bounce Point (Latitude°)	$S_{\text{LAB}}S$ Amplitude	Earthquake Date	Earthquake (Longitude°)	Earthquake (Latitude°)	Station Name
148	-43.3	14.9	-0.1	2010-03-05	-73.4	-36.7	KONO
149	-60.2	24.5	0.2	2010-03-05	-73.4	-36.7	KBS
150	-45.8	23.0	0.5	2010-03-05	-73.4	-36.7	LVZ
151	63.6	-56.0	-0.1	2010-03-05	-73.4	-36.7	CHTO
152	18.4	-52.5	0.3	2010-03-05	-73.4	-36.7	DGAR
153	57.8	-63.7	-0.1	2010-03-05	101.0	-3.8	TRQA
154	48.3	2.4	0.2	2010-03-05	101.0	-3.8	DBIC
155	43.7	-10.8	-0.0	2010-03-05	101.0	-3.8	ASCN
156	159.6	-30.7	-0.3	2010-03-05	101.0	-3.8	PTCN
157	-145.6	9.7	0.1	2010-03-11	-71.9	-34.3	INCN
158	2.5	-38.1	0.2	2010-03-11	-71.9	-34.3	MSEY
159	-129.6	32.1	-0.3	2010-03-11	-71.9	-34.3	BJT
160	-118.1	-8.8	-0.5	2010-03-11	-71.9	-34.3	KIP
161	-139.4	-15.0	-0.6	2010-03-11	-71.9	-34.3	WAKE
162	16.1	-50.1	-0.3	2010-03-11	-71.9	-34.3	DGAR
163	-134.8	12.5	-0.0	2010-03-11	-71.9	-34.3	ERM
164	24.9	-43.5	0.2	2010-03-11	-71.8	-34.3	PALK
165	-134.8	12.4	0.0	2010-03-11	-71.8	-34.3	ERM
166	-132.9	49.7	0.2	2010-03-14	141.6	37.7	BCIP
167	-173.2	-30.4	0.1	2010-03-14	141.6	37.7	EFI
168	-140.9	36.7	0.1	2010-03-14	141.6	37.7	PAYG
169	-43.3	15.1	-0.2	2010-03-16	-73.3	-36.2	KONO
170	-45.9	23.3	0.7	2010-03-16	-73.3	-36.2	LVZ
171	-147.1	0.6	-0.1	2010-03-16	-73.3	-36.2	MAJO
172	-166.6	-64.9	0.3	2010-03-16	-73.3	-36.2	WRAB
173	-45.2	11.5	-0.3	2010-03-16	-73.3	-36.2	ESK
174	-130.8	16.4	0.1	2010-03-16	-73.3	-36.2	YSS
175	-160.3	31.6	-0.0	2010-03-20	152.2	-3.4	WCI
176	-175.5	36.0	0.3	2010-03-20	152.2	-3.4	FFC
177	92.6	-4.1	0.2	2010-03-20	152.2	-3.4	MBAR
178	-141.0	7.4	-0.2	2010-03-20	152.2	-3.4	SDV
179	-160.3	36.8	0.2	2010-03-20	152.2	-3.4	SSPA
180	75.4	8.2	0.1	2010-03-20	152.2	-3.4	DBIC
181	-144.6	20.0	-0.4	2010-03-20	152.2	-3.4	SDDR
182	-161.5	41.1	0.5	2010-03-20	152.2	-3.4	HRV
183	-137.7	-35.4	-0.0	2010-04-11	161.1	-10.9	LVC
184	-115.0	-44.8	0.0	2010-04-11	161.1	-10.9	RCBR
185	58.5	0.5	-0.1	2010-04-13	96.5	33.2	SUR
186	146.7	13.7	-0.1	2010-04-13	96.5	33.2	AFI
187	-142.4	26.4	0.1	2010-04-26	123.7	22.2	LPAZ
188	69.9	2.5	0.6	2010-04-26	123.7	22.2	TSUM
189	-173.9	43.2	0.4	2010-04-26	123.7	22.2	SLBS
190	75.4	-2.1	-0.1	2010-04-26	123.7	22.2	LBTB
191	-93.6	9.1	0.0	2010-04-30	-177.9	60.5	HOPE
192	-29.5	53.8	0.2	2010-04-30	-177.9	60.5	ASCN
193	138.7	15.7	-0.1	2010-05-05	101.1	-4.0	MIDW
194	40.1	-68.1	-0.3	2010-05-05	101.1	-4.0	LVC
195	48.4	2.2	0.1	2010-05-05	101.1	-4.0	DBIC
196	159.7	-30.9	-0.0	2010-05-05	101.1	-4.0	PTCN
197	62.1	-61.8	0.1	2010-05-09	96.0	3.8	PLCA
198	159.0	-42.4	0.0	2010-05-09	96.0	3.8	RPN

Measurement Index	Bounce Point (Longitude°)	Bounce Point (Latitude°)	$S_{\mathrm{LAB}}S$ Amplitude	Earthquake Date	Earthquake (Longitude°)	Earthquake (Latitude°)	Station Name
199	-155.5	-49.4	-0.6	2010-05-24	-71.6	-8.1	KAPI
200	-37.6	44.6	0.3	2010-05-24	-71.6	-8.1	BRVK
201	-132.0	50.0	-0.4	2010-05-24	-71.6	-8.1	TATO
202	-116.5	-51.8	0.1	2010-05-24	-71.6	-8.1	TAU
203	-139.8	-47.6	0.3	2010-05-24	-71.6	-8.1	WRAB
204	-140.2	8.4	-0.1	2010-05-24	-71.6	-8.1	GUMO
205	-145.2	50.4	-0.0	2010-05-26	129.9	25.8	BCIP
206	146.7	-49.4	0.6	2010-05-26	129.9	25.8	EFI
207	78.6	-2.3	0.5	2010-05-26	129.9	25.8	BOSA
208	-145.2	9.5	0.1	2010-05-26	129.9	25.8	LVC
209	-143.6	27.2	-0.1	2010-05-26	129.9	25.8	NNA
210	146.9	26.0	-0.1	2010-05-31	93.5	11.1	POHA
211	41.3	-46.9	0.2	2010-06-12	91.9	7.9	TRQA
212	-179.5	36.2	0.1	2010-06-16	136.5	-2.2	RSSD
213	-155.4	11.3	0.2	2010-06-16	136.5	-2.2	JTS
214	93.5	-14.7	-0.3	2010-06-16	136.5	-2.2	ABPO
215	-155.3	25.6	0.6	2010-06-16	136.5	-2.2	MTDJ
216	-170.6	19.1	0.0	2010-06-16	136.5	-2.2	SLBS
217	-151.9	23.4	0.3	2010-06-26	161.4	-10.6	WCI
218	-168.0	20.9	0.1	2010-06-26	161.4	-10.6	COR
219	-141.8	-0.3	-0.4	2010-06-26	161.4	-10.6	JTS
220	-130.6	2.0	-0.3	2010-06-26	161.4	-10.6	GRGR
221	116.8	-12.6	-0.7	2010-06-26	161.4	-10.6	DGAR
222	111.9	11.6	-0.1	2010-06-26	161.4	-10.6	UOSS
223	-42.8	14.0	-1.0	2010-07-14	-73.3	-38.1	KONO
224	-169.1	-65.4	0.2	2010-07-14	-73.3	-38.1	WRAB
225	-105.6	12.3	0.1	2010-07-18	-169.7	52.9	TRQA
226	-129.8	-9.5	0.3	2010-07-18	-169.7	52.9	PMSA
227	-146.2	17.5	-0.1	2010-07-18	150.4	-6.0	GTBY
228	100.5	-53.2	0.4	2010-07-23	123.4	6.7	HOPE
229	-163.7	-39.5	-0.2	2010-07-23	123.5	6.5	LPAZ
230	-158.1	17.3	-0.0	2010-07-23	123.5	6.5	OTAV
231	100.6	-53.5	0.4	2010-07-23	123.5	6.5	HOPE
232	-176.7	53.8	0.3	2010-07-23	123.5	6.5	DWPF
233	100.4	-53.0	-0.3	2010-07-23	123.3	6.8	HOPE
234	-163.7	-40.2	-0.0	2010-07-24	123.5	6.2	LPAZ
235	-158.0	16.6	0.5	2010-07-24	123.5	6.2	OTAV
236	-164.3	9.6	-0.2	2010-07-24	123.5	6.2	PAYG
237	61.1	14.5	0.2	2010-07-24	123.5	6.2	DBIC
238	-166.2	49.4	-0.5	2010-07-24	123.5	6.2	MTDJ
239	-161.2	34.6	-1.3	2010-07-29	123.2	6.5	BCIP
240	-164.7	10.2	-0.4	2010-07-29	123.2	6.5	PAYG
241	-154.4	-20.3	-0.1	2010-07-29	123.2	6.5	SAML
242	-166.7	34.5	-0.0	2010-07-29	123.2	6.5	TGUH
243	-177.2	54.0	-0.3	2010-07-29	123.2	6.5	DWPF
244	-162.9	-55.3	0.5	2010-08-04	146.8	-5.5	TRQA
245	93.1	-31.8	0.1	2010-08-04	146.8	-5.5	BOSA
246	-155.8	40.0	-0.2	2010-08-04	146.8	-5.5	BBSR
247	-148.4	-38.9	0.1	2010-08-04	146.8	-5.5	LVC
248	-166.2	42.8	0.0	2010-08-04	146.8	-5.5	HRV
249	-145.1	4.0	0.2	2010-08-04	150.8	-5.8	BCIP

Measurement Index	Bounce Point (Longitude°)	Bounce Point (Latitude°)	$S_{\mathrm{LAB}}S$ Amplitude	Earthquake Date	Earthquake (Longitude°)	Earthquake (Latitude°)	Station Name
250	90.6	-6.3	0.4	2010-08-04	150.8	-5.8	MBAR
251	-168.7	29.2	0.2	2010-08-04	150.8	-5.8	RSSD
252	-146.1	17.6	0.1	2010-08-04	150.8	-5.8	GTBY
253	-140.6	4.4	0.6	2010-08-04	150.8	-5.8	SDV
254	-151.4	36.9	0.3	2010-08-04	150.8	-5.8	BBSR
255	-145.1	-36.5	0.0	2010-08-04	150.8	-5.8	LVC
256	-163.2	-24.6	-0.1	2010-08-04	150.8	-5.8	RPN
257	-146.4	14.9	-0.1	2010-08-04	150.8	-5.8	MTDJ
258	-129.3	0.6	0.1	2010-08-10	168.1	-17.5	SJG
259	167.6	25.2	0.1	2010-08-10	168.1	-17.5	BILL
260	-20.6	-2.2	-0.4	2010-08-12	-77.3	-1.3	KMBO
261	-18.7	-20.9	0.0	2010-08-12	-77.3	-1.3	ABPO
262	-34.4	-24.4	0.3	2010-08-12	-77.3	-1.3	SUR
263	-20.4	7.1	0.0	2010-08-12	-77.3	-1.3	FURI
264	-124.6	44.6	0.3	2010-08-12	-77.3	-1.3	ERM
265	61.7	10.8	-0.0	2010-08-13	141.5	12.5	ASCN
266	-146.7	17.8	0.2	2010-08-14	141.4	12.3	OTAV
267	-149.8	-19.0	-0.1	2010-08-14	141.4	12.3	LVC
268	-147.6	0.4	-0.0	2010-08-14	141.4	12.3	NNA
269	-117.2	-0.2	0.0	2010-09-03	-175.9	51.5	EFI
270	-108.8	12.0	-0.0	2010-09-03	-175.9	51.5	TRQA
271	-134.4	-4.2	-0.2	2010-09-03	171.8	-43.5	WCI
272	83.7	-44.8	-0.2	2010-09-03	171.8	-43.5	KMBO
273	-107.0	-30.9	-0.4	2010-09-03	171.8	-43.5	BBGH
274	99.4	-39.4	0.1	2010-09-03	171.8	-43.5	MSEY
275	-120.3	-42.4	-0.2	2010-09-03	171.8	-43.5	NNA
276	-127.8	-22.1	-0.0	2010-09-03	171.8	-43.5	TGUH
277	-127.3	-12.7	0.2	2010-09-03	171.8	-43.5	DWPF
278	-170.8	33.6	0.0	2010-09-03	171.8	-43.5	BORG
279	170.0	12.3	0.1	2010-09-03	171.8	-43.5	BILL
280	154.5	38.9	-0.3	2010-09-03	171.8	-43.5	ESK
281	104.0	-16.8	0.2	2010-09-03	171.8	-43.5	UOSS
282	-129.1	-1.0	0.3	2010-09-03	171.8	-43.5	HRV
283	-143.7	-12.7	0.1	2010-09-03	171.8	-43.5	SLBS
284	-174.3	39.7	0.5	2010-09-29	133.8	-5.0	WCI
285	169.1	41.5	0.2	2010-09-29	133.8	-5.0	FFC
286	175.5	-65.5	0.2	2010-09-29	133.8	-5.0	TRQA
287	-152.0	-8.5	-0.3	2010-09-29	133.8	-5.0	OTAV
288	-164.8	33.6	0.1	2010-09-29	133.8	-5.0	DWPF
289	-88.8	-14.8	-0.3	2010-10-21	-109.2	24.7	EFI
290	-31.8	31.7	0.1	2010-10-21	-109.2	24.7	MBAR
291	-122.5	-30.8	-0.2	2010-10-21	-109.2	24.7	VNDA
292	179.6	22.6	-0.2	2010-10-21	-109.2	24.7	KAPI
293	-81.9	-17.9	0.0	2010-10-21	-109.2	24.7	HOPE
294	177.2	59.4	-0.0	2010-10-21	-109.2	24.7	KMI
295	-121.8	-30.4	-0.0	2010-10-21	-109.2	24.7	SBA
296	-132.4	-37.3	-0.1	2010-10-21	-109.2	24.7	CASY
297	-152.1	50.3	-0.0	2010-10-21	-109.2	24.7	YSS
298	-34.7	-71.1	0.1	2010-11-10	96.4	-45.5	LPAZ
299	-164.0	-23.5	-0.4	2010-11-10	96.4	-45.5	ANMO
300	132.9	16.6	0.2	2010-11-10	96.4	-45.5	COLA

Measurement Index	Bounce Point (Longitude°)	Bounce Point (Latitude°)	$S_{\mathrm{LAB}}S$ Amplitude	Earthquake Date	Earthquake (Longitude°)	Earthquake (Latitude°)	Station Name
301	-18.9	-47.9	0.2	2010-11-10	96.4	-45.5	BBGH
302	-43.3	-58.5	0.0	2010-11-10	96.4	-45.5	SDV
303	69.4	-3.0	-0.1	2010-11-10	96.4	-45.5	GNI
304	-26.6	-64.7	0.5	2010-11-10	96.4	-45.5	SAML
305	-173.8	-19.4	0.8	2010-11-10	96.4	-45.5	PFO
306	179.6	-59.8	0.1	2010-11-10	96.4	-45.5	PTCN
307	124.9	4.4	0.1	2010-11-10	96.4	-45.5	PET
308	59.5	16.9	0.5	2010-11-10	96.4	-45.5	BORG
309	53.6	7.5	0.5	2010-11-10	96.4	-45.5	ESK
310	-157.2	-36.3	0.3	2010-11-10	96.4	-45.5	SLBS
311	-142.1	-31.1	0.2	2010-12-02	150.0	-6.0	LPAZ
312	-176.2	35.8	-0.0	2010-12-02	150.0	-6.0	FFC
313	-144.6	-21.7	0.4	2010-12-02	150.0	-6.0	NNA
314	-160.9	36.3	0.5	2010-12-02	150.0	-6.0	SSPA
315	-22.7	48.3	-0.0	2010-12-20	59.2	28.4	JTS
316	-12.8	38.3	0.1	2010-12-20	59.2	28.4	SDV
317	-28.4	6.4	-0.2	2010-12-20	59.2	28.4	RPN
318	61.2	19.8	0.3	2010-12-21	143.7	26.9	SHEL
319	-106.6	-47.4	0.2	2010-12-25	167.9	-19.7	RCBR
320	-145.2	47.5	-0.5	2010-12-25	167.9	-19.7	CMLA
321	175.5	47.2	0.1	2010-12-25	167.9	-19.7	BORG
322	167.5	24.1	0.5	2010-12-25	167.9	-19.7	BILL
323	174.6	37.1	0.0	2010-12-25	167.9	-19.7	ALE
324	-145.8	-51.3	0.3	2011-01-01	-63.1	-26.8	PMG
325	-118.1	0.3	0.1	2011-01-01	-63.1	-26.8	MIDW
326	-140.4	-59.7	0.5	2011-01-01	-63.1	-26.8	CTAO
327	-109.1	-6.2	-0.2	2011-01-01	-63.1	-26.8	POHA
328	-130.1	-9.6	0.0	2011-01-01	-63.1	-26.8	WAKE
329	-63.0	25.8	0.1	2011-01-01	-63.1	-26.8	ALE
330	-169.5	-65.5	0.2	2011-01-02	-73.3	-38.4	WRAB
331	-28.6	19.9	0.2	2011-01-02	-73.3	-38.4	ARU
332	-48.1	21.6	0.5	2011-01-02	-73.3	-38.4	KEV
333	-135.2	-42.2	-0.3	2011-01-02	-73.3	-38.4	MSVF
334	-122.2	15.8	-0.3	2011-01-02	-73.3	-38.4	PET
335	-137.6	-67.9	-0.0	2011-01-02	-73.3	-38.4	TAU
336	-133.2	13.3	-0.2	2011-01-02	-73.3	-38.4	YSS
337	-144.8	47.6	0.4	2011-01-09	168.3	-19.2	CMLA
338	107.8	-35.1	0.3	2011-01-09	168.3	-19.2	ABPO
339	133.5	17.5	0.3	2011-01-13	168.5	-20.6	MAKZ
340	150.5	39.9	0.2	2011-01-13	168.5	-20.6	KEV
341	176.5	46.7	-0.3	2011-01-13	168.5	-20.6	BORG
342	162.7	39.5	-0.0	2011-01-13	168.5	-20.6	KBS
343	-30.0	13.8	0.2	2011-01-18	63.9	28.8	RPN
344	0.2	85.1	-0.0	2011-01-18	63.9	28.8	TUC
345	2.3	2.6	0.6	2011-01-18	63.9	28.8	CPUP
346	171.7	53.6	-0.1	2011-02-10	123.0	4.2	WCI
347	-165.4	-46.7	-0.4	2011-02-10	123.0	4.2	LPAZ
348	124.6	-60.5	-0.2	2011-02-10	123.0	4.2	EFI
349	155.5	-60.3	0.2	2011-02-10	123.0	4.2	PLCA
350	174.3	39.1	0.1	2011-02-10	123.0	4.2	ANMO
351	-175.3	-55.2	-0.9	2011-02-10	123.0	4.2	LVC

Measurement Index	Bounce Point (Longitude°)	Bounce Point (Latitude°)	$S_{\mathrm{LAB}}S$ Amplitude	Earthquake Date	Earthquake (Longitude°)	Earthquake (Latitude°)	Station Name
352	174.9	35.2	-0.0	2011-02-10	123.0	4.2	TUC
353	-43.1	15.0	-0.2	2011-02-11	-73.1	-36.5	KONO
354	-29.6	21.6	0.1	2011-02-11	-73.1	-36.5	ARU
355	-87.6	3.9	0.5	2011-02-11	-73.1	-36.5	RSSD
356	-48.4	22.8	0.3	2011-02-11	-73.1	-36.5	KEV
357	-59.9	24.6	0.1	2011-02-11	-73.1	-36.5	KBS
358	-130.8	16.2	0.1	2011-02-11	-73.1	-36.5	YSS
359	26.4	-45.3	-0.0	2011-02-14	-72.8	-35.4	PALK
360	-30.2	22.5	0.1	2011-02-14	-72.8	-35.4	ARU
361	-157.4	-49.4	0.1	2011-02-14	-72.8	-35.4	PMG
362	-48.6	23.4	-0.0	2011-02-14	-72.8	-35.4	KEV
363	-55.7	16.0	-0.2	2011-02-14	-72.8	-35.4	BORG
364	17.1	-51.4	-0.1	2011-02-14	-72.8	-35.4	DGAR
365	-136.7	10.5	-0.0	2011-02-14	-72.8	-35.4	ERM
366	-59.9	25.2	0.5	2011-02-14	-72.8	-35.4	KBS
367	-129.6	17.7	0.1	2011-02-14	-72.8	-35.4	YSS
368	-32.1	16.2	0.3	2011-02-14	-72.8	-35.4	OBN
369	141.9	25.2	0.1	2011-02-21	178.4	-26.1	ARU
370	123.5	16.1	0.5	2011-02-21	178.4	-26.1	GNI
371	-121.5	24.4	0.0	2011-02-21	178.4	-26.1	CMLA
372	-174.1	31.4	0.3	2011-02-21	178.4	-26.1	ALE
373	3.1	-3.5	0.1	2011-03-06	-27.1	-56.4	KIEV
374	70.3	-22.5	0.2	2011-03-06	-27.1	-56.4	BJT
375	-130.0	43.5	0.0	2011-03-09	142.8	38.4	OTAV
376	-130.1	43.4	0.0	2011-03-09	142.8	38.3	OTAV
377	-167.3	-15.8	-0.2	2011-03-10	116.7	-6.9	PAYG
378	-123.6	33.8	0.0	2011-03-12	142.7	37.6	LPAZ
379	-137.5	46.9	-0.4	2011-03-12	142.7	37.6	JTS
380	-140.8	36.1	-0.6	2011-03-12	142.7	37.6	PAYG
381	-140.2	48.3	0.2	2011-03-12	142.7	37.6	TGUH
382	-170.1	8.6	0.0	2011-03-12	142.7	37.6	PTCN
383	47.2	-40.4	-0.2	2011-03-24	99.8	20.7	TRQA
384	99.9	-34.6	0.1	2011-03-24	99.8	20.7	QSPA
385	-6.8	86.1	-0.1	2011-03-24	99.8	20.7	MTDJ
386	110.6	-31.1	0.2	2011-03-24	99.8	20.7	SBA
387	-26.1	19.1	-0.3	2011-04-07	-94.3	17.2	KMBO
388	-33.0	2.1	-0.3	2011-04-07	-94.3	17.2	LSZ
389	-137.2	47.9	-0.3	2011-04-07	141.6	38.3	JTS
390	132.1	-43.9	-0.4	2011-04-11	140.4	37.0	HOPE
391	-152.3	23.6	0.4	2011-04-23	161.2	-10.4	WCI
392	-142.1	-0.1	-0.0	2011-04-23	161.2	-10.4	JTS
393	-130.1	3.9	0.1	2011-04-23	161.2	-10.4	BBGH
394	-142.1	26.1	0.5	2011-04-23	161.2	-10.4	BBSR
395	-151.7	21.7	0.1	2011-04-23	161.2	-10.4	WVT
396	144.7	-1.4	0.0	2011-06-22	142.2	40.0	TAU
397	144.3	25.5	0.0	2011-07-06	-176.3	-29.5	ARU
398	156.8	11.5	0.4	2011-07-06	-176.3	-29.5	HIA
399	142.8	16.7	-0.6	2011-07-06	-176.3	-29.5	KURK
400	145.1	33.3	0.3	2011-07-06	-176.3	-29.5	OBN
401	-130.3	43.0	-0.2	2011-07-10	143.3	38.0	OTAV
402	89.5	14.0	0.1	2011-07-10	143.3	38.0	ABPO

Measurement Index	Bounce Point (Longitude°)	Bounce Point (Latitude°)	$S_{\mathrm{LAB}}S$ Amplitude	Earthquake Date	Earthquake (Longitude°)	Earthquake (Latitude°)	Station Name
403	-161.2	49.5	-0.9	2011-07-10	143.3	38.0	TUC
404	-135.8	14.5	-0.0	2011-07-29	179.8	-23.8	HRV
405	-175.6	48.9	0.1	2011-07-29	179.8	-23.8	ESK
406	-140.4	-24.3	0.1	2011-07-31	144.8	-3.5	SAML
407	-156.6	28.8	-0.5	2011-07-31	144.8	-3.5	DWPF
408	-169.1	22.6	-0.2	2011-07-31	144.8	-3.5	TUC
409	-171.8	22.3	-0.8	2011-07-31	144.8	-3.5	PFO
410	144.8	-46.7	0.2	2011-07-31	144.8	-3.5	QSPA
411	-145.7	25.5	0.1	2011-07-31	144.8	-3.5	SJG
412	-151.6	-53.2	0.3	2011-07-31	144.8	-3.5	CPUP
413	129.1	17.2	-0.2	2011-08-20	168.1	-18.4	AAK
414	150.5	41.1	-0.1	2011-08-20	168.1	-18.4	KEV
415	133.7	24.7	0.4	2011-08-20	168.1	-18.4	BRVK
416	134.0	29.3	0.1	2011-08-20	168.2	-18.3	ARU
417	129.1	17.3	-0.1	2011-08-20	168.2	-18.3	AAK
418	-115.0	-19.2	-0.3	2011-08-24	-74.5	-7.6	RAR
419	-39.0	55.9	0.3	2011-08-24	-74.5	-7.6	WMQ
420	-52.5	39.9	0.0	2011-08-24	-74.5	-7.6	LVZ
421	-24.6	-17.9	0.2	2011-08-24	-74.5	-7.6	LSZ
422	-139.5	-35.2	-0.1	2011-08-24	-74.5	-7.6	CTAO
423	177.2	42.3	-0.8	2011-08-30	126.8	-6.4	WCI
424	-165.4	39.6	-0.1	2011-08-30	126.8	-6.4	GRTK
425	160.8	42.1	0.0	2011-08-30	126.8	-6.4	FFC
426	177.9	28.6	0.0	2011-08-30	126.8	-6.4	ANMO
427	148.1	34.1	0.0	2011-08-30	126.8	-6.4	COLA
428	171.2	36.2	-0.1	2011-08-30	126.8	-6.4	RSSD
429	167.0	29.6	0.1	2011-08-30	126.8	-6.4	COR
430	-163.6	31.5	0.3	2011-08-30	126.8	-6.4	GTBY
431	80.2	-16.1	-0.1	2011-08-30	126.8	-6.4	LSZ
432	-172.1	37.0	0.4	2011-08-30	126.8	-6.4	DWPF
433	178.2	24.8	-0.5	2011-08-30	126.8	-6.4	TUC
434	171.4	50.1	0.0	2011-08-30	126.8	-6.4	SSPA
435	175.6	24.0	-0.2	2011-08-30	126.8	-6.4	PFO
436	-162.2	41.6	-0.3	2011-08-30	126.8	-6.4	SJG
437	-162.6	25.9	0.2	2011-08-30	126.8	-6.4	MTDJ
438	-177.3	17.3	-0.3	2011-08-30	126.8	-6.4	SLBS
439	-27.9	52.5	0.4	2011-09-02	-171.7	52.2	SHEL
440	-179.2	5.6	0.2	2011-09-02	-171.7	52.2	SNZO
441	-177.2	-12.9	0.0	2011-09-02	-171.7	52.2	SBA
442	-21.1	25.6	0.1	2011-09-02	-63.1	-28.4	BRVK
443	-127.6	19.8	-0.5	2011-09-02	-63.1	-28.4	MAJO
444	130.0	15.6	-0.2	2011-09-03	169.7	-20.7	AAK
445	-144.7	11.9	0.0	2011-09-03	169.7	-20.7	WVT
446	144.5	15.2	-0.1	2011-09-03	169.7	-20.7	ULN
447	-143.4	17.1	0.1	2011-09-03	169.7	-20.7	SSPA
448	-98.1	-16.0	-0.2	2011-09-15	-179.5	-21.6	SACV
449	145.6	28.8	0.1	2011-09-15	-179.5	-21.6	ARU
450	162.5	38.6	0.3	2011-09-15	-179.5	-21.6	LVZ
451	-121.2	-27.7	0.2	2011-09-15	-179.5	-21.6	SAML
452	152.3	14.1	-0.7	2011-09-15	-179.5	-21.6	ULN
453	106.5	-19.3	-0.2	2011-09-15	-179.5	-21.6	FURI

Measurement Index	Bounce Point (Longitude°)	Bounce Point (Latitude°)	$S_{\mathrm{LAB}}S$ Amplitude	Earthquake Date	Earthquake (Longitude°)	Earthquake (Latitude°)	Station Name
454	146.1	36.5	0.2	2011-09-15	-179.5	-21.6	OBN
455	-128.2	44.7	0.3	2011-09-16	142.8	40.3	OTAV
456	-22.4	62.2	0.3	2011-09-18	88.1	27.7	OTAV
457	93.7	-38.0	-0.1	2011-10-14	147.9	-6.6	SUR
458	-151.0	-7.4	-0.1	2011-10-14	147.9	-6.6	PAYG
459	-111.9	16.6	-0.5	2011-10-21	-176.2	-29.0	CMLA
460	-131.8	8.8	0.2	2011-10-21	-176.2	-29.0	SSPA
461	-155.9	38.8	0.1	2011-10-21	-176.2	-29.0	BORG
462	-130.4	-6.1	-0.2	2011-10-21	-176.2	-29.0	TEIG
463	-163.7	46.7	-0.0	2011-10-21	-176.2	-29.0	ESK
464	145.2	35.0	-0.5	2011-10-23	43.5	38.7	RAR
465	-88.0	-54.5	0.2	2011-10-28	-76.0	-14.4	VNDA
466	-163.9	-51.3	-0.9	2011-10-28	-76.0	-14.4	KAPI
467	-111.3	27.1	-0.2	2011-10-28	-76.0	-14.4	ADK
468	0.6	-35.3	-0.1	2011-10-28	-76.0	-14.4	DGAR
469	133.9	-49.6	-0.2	2011-11-08	125.6	27.3	EFI
470	176.6	58.9	-0.1	2011-11-08	125.6	27.3	RSSD
471	-152.7	37.3	-0.2	2011-11-08	125.6	27.3	PAYG
472	-153.3	53.0	-0.1	2011-11-08	125.6	27.3	TGUH
473	-134.3	75.7	0.4	2011-11-08	125.6	27.3	SJG
474	-31.4	33.9	0.2	2011-11-22	-65.1	-15.4	ARU
475	-28.7	60.0	-0.0	2011-11-22	-65.1	-15.4	ENH
476	-26.9	39.7	0.3	2011-11-22	-65.1	-15.4	KURK
477	-161.9	-2.1	-0.2	2011-12-11	-100.0	17.8	WRAB
478	-16.2	28.5	-0.0	2011-12-11	-100.0	17.8	MSEY
479	-165.3	48.1	-0.2	2011-12-11	-100.0	17.8	TATO
480	-156.1	-1.9	-0.0	2011-12-11	-100.0	17.8	CTAO
481	-168.3	-4.6	0.4	2011-12-11	-100.0	17.8	MBWA
482	-147.1	2.0	0.2	2011-12-14	146.8	-7.6	BCIP
483	-164.0	-52.3	0.3	2011-12-14	146.8	-7.6	PLCA
484	-162.2	-56.9	0.1	2011-12-14	146.8	-7.6	TRQA
485	74.5	-41.2	-0.1	2011-12-14	146.8	-7.6	SHEL
486	-149.9	3.1	0.1	2011-12-14	146.8	-7.6	JTS
487	85.5	-28.9	-0.0	2011-12-14	146.8	-7.6	TSUM
488	91.2	-30.6	0.0	2011-12-14	146.8	-7.6	LBTB
489	-43.2	51.5	0.4	2011-12-27	95.9	51.8	LPAZ
490	162.7	23.4	-0.5	2011-12-27	95.9	51.8	RAR
491	-29.9	57.0	0.5	2011-12-27	95.9	51.8	PTGA
492	96.0	-19.0	0.3	2011-12-27	95.9	51.8	QSPA
493	-140.3	48.4	-0.6	2012-01-01	138.1	31.5	BCIP
494	-144.6	45.9	-0.6	2012-01-01	138.1	31.5	JTS
495	-148.3	72.3	-0.9	2012-01-01	138.1	31.5	BBSR
496	-147.4	47.3	0.1	2012-01-01	138.1	31.5	TGUH
497	-159.9	52.7	0.2	2012-01-01	138.1	31.5	HKT
498	-130.0	18.6	0.4	2012-01-01	138.1	31.5	CPUP
499	-18.3	-7.4	-0.1	2012-01-15	-56.1	-61.0	BFO
500	-22.5	-0.8	-0.0	2012-01-15	-56.1	-61.0	KONO
501	-98.0	2.8	-0.5	2012-01-15	-56.1	-61.0	COLA
502	-96.9	-9.7	0.1	2012-01-15	-56.1	-61.0	COR
503	0.8	-14.3	-0.4	2012-01-15	-56.1	-61.0	ANTO
504	-23.9	-11.8	-0.2	2012-01-15	-56.1	-61.0	PAB

Measurement Index	Bounce Point (Longitude°)	Bounce Point (Latitude°)	$S_{\mathrm{LAB}}S$ Amplitude	Earthquake Date	Earthquake (Longitude°)	Earthquake (Latitude°)	Station Name
505	-18.1	4.9	0.2	2012-01-15	-56.1	-61.0	LVZ
506	-141.8	-51.8	0.0	2012-01-15	-56.1	-61.0	AFI
507	117.7	-43.9	0.0	2012-01-15	-56.1	-61.0	SSE
508	-107.3	-2.4	-0.1	2012-01-15	-56.1	-61.0	KDAK
509	-38.4	10.4	0.1	2012-01-15	-56.1	-61.0	KBS
510	-27.4	-3.2	0.1	2012-01-15	-56.1	-61.0	ESK
511	-4.9	-4.2	0.3	2012-01-15	-56.1	-61.0	OBN
512	157.9	27.8	-0.2	2012-02-02	167.1	-17.8	TIXI
513	-103.8	-14.9	-0.1	2012-02-02	167.1	-17.8	SACV
514	133.1	29.3	0.3	2012-02-02	167.1	-17.8	ARU
515	145.5	39.5	0.0	2012-02-02	167.1	-17.8	LVZ
516	-132.5	1.2	-0.0	2012-02-02	167.1	-17.8	SDDR
517	-129.7	0.3	0.4	2012-02-02	167.1	-17.8	SJG
518	173.9	48.2	-0.7	2012-02-02	167.1	-17.8	BORG
519	93.3	-51.9	0.4	2012-02-02	167.1	-17.8	TSUM
520	166.9	25.1	0.0	2012-02-02	167.1	-17.8	BILL
521	-141.2	1.9	0.1	2012-02-02	167.1	-17.8	TEIG
522	173.7	38.1	-0.7	2012-02-02	167.1	-17.8	ALE
523	159.1	-57.3	-0.0	2012-02-06	123.2	10.0	PLCA
524	169.8	50.2	0.3	2012-02-06	123.2	10.0	RSSD
525	76.4	-3.9	0.3	2012-02-06	123.2	10.0	LSZ
526	54.0	2.9	0.2	2012-02-06	123.2	10.0	ASCN
527	162.6	23.3	0.4	2012-02-26	96.0	51.7	RAR
528	111.5	-14.6	-0.9	2012-02-26	96.0	51.7	VNDA
529	-104.1	-47.3	-0.2	2012-03-03	170.3	-22.1	RCBR
530	107.7	-38.2	-0.3	2012-03-03	170.3	-22.1	ABPO
531	164.9	38.8	-0.1	2012-03-03	170.3	-22.1	KBS
532	177.3	35.7	0.4	2012-03-03	170.3	-22.1	ALE
533	152.2	41.0	0.0	2012-03-09	169.6	-19.1	KEV
534	-106.7	-44.9	-0.1	2012-03-09	169.6	-19.1	RCBR
535	101.4	-12.2	-0.2	2012-03-09	169.6	-19.1	FURI
536	164.2	40.3	-0.2	2012-03-09	169.6	-19.1	KBS
537	-132.1	-26.9	-0.3	2012-03-09	169.6	-19.1	NNA
538	10.1	73.5	0.6	2012-03-14	144.9	40.9	SACV
539	-162.5	-23.1	0.3	2012-03-14	144.9	40.9	EFI
540	-50.9	22.2	0.6	2012-03-20	-98.2	16.5	KOWA
541	-156.8	6.5	-1.0	2012-03-20	-98.2	16.5	PMG
542	-152.3	77.4	-0.3	2012-03-20	-98.2	16.5	LSA
543	-168.7	29.2	-0.1	2012-03-20	-98.2	16.5	DAV
544	-27.6	31.5	-0.2	2012-03-20	-98.2	16.5	FURI
545	-163.9	32.2	-0.4	2012-03-21	146.0	-6.2	WCI
546	-139.6	-27.9	-0.1	2012-03-21	146.0	-6.2	SAML
547	85.2	-27.3	-0.1	2012-03-21	146.0	-6.2	TSUM
548	-150.3	-54.5	0.1	2012-03-21	146.0	-6.2	CPUP
549	90.8	-29.2	0.3	2012-03-21	146.0	-6.2	LBTB
550	-29.7	22.4	0.1	2012-03-25	-72.2	-35.2	ARU
551	-145.2	2.5	-0.2	2012-03-25	-72.2	-35.2	MAJO
552	-119.0	19.1	-0.3	2012-03-25	-72.2	-35.2	PET
553	-59.4	25.2	-0.1	2012-03-25	-72.2	-35.2	KBS
554	122.7	-62.3	0.1	2012-03-25	-72.2	-35.2	QIZ
555	-128.8	18.2	0.4	2012-03-25	-72.2	-35.2	YSS

Measurement Index	Bounce Point (Longitude°)	Bounce Point (Latitude°)	$S_{\mathrm{LAB}}S$ Amplitude	Earthquake Date	Earthquake (Longitude°)	Earthquake (Latitude°)	Station Name
556	-175.9	50.3	-0.0	2012-04-11	-102.7	18.2	QIZ
557	-170.1	-4.0	0.2	2012-04-11	-102.7	18.2	MBWA
558	-117.3	-7.7	-0.1	2012-04-17	-71.4	-32.6	KIP
559	-18.3	26.3	-0.1	2012-04-17	-71.4	-32.6	MAKZ
560	-32.2	18.1	0.1	2012-04-17	-71.4	-32.6	OBN
561	-163.3	32.2	-0.1	2012-04-17	147.1	-5.5	WCI
562	-148.1	23.1	-0.0	2012-04-17	147.1	-5.5	GRTK
563	-162.4	-55.1	0.4	2012-04-17	147.1	-5.5	TRQA
564	166.0	-55.7	-0.0	2012-04-17	147.1	-5.5	PMSA
565	-155.4	39.8	0.1	2012-04-17	147.1	-5.5	BBSR
566	-162.2	30.0	0.4	2012-04-17	147.1	-5.5	WVT
567	71.8	2.5	-0.0	2012-04-17	147.1	-5.5	DBIC
568	-139.3	-25.8	0.1	2012-04-17	147.1	-5.5	SAML
569	-155.3	25.6	0.3	2012-04-17	147.1	-5.5	DWPF
570	-170.9	20.2	-0.2	2012-04-17	147.1	-5.5	PFO
571	-144.4	21.0	-0.1	2012-04-17	147.1	-5.5	SJG
572	-146.6	-22.3	0.0	2012-04-17	147.1	-5.5	NNA
573	-174.0	42.2	0.0	2012-04-21	134.3	-1.6	WCI
574	179.8	-56.8	0.6	2012-04-21	134.3	-1.6	PLCA
575	176.3	-63.0	0.3	2012-04-21	134.3	-1.6	TRQA
576	155.1	36.9	0.0	2012-04-21	134.3	-1.6	COLA
577	-152.1	-2.5	0.5	2012-04-21	134.3	-1.6	OTAV
578	178.7	37.4	-0.3	2012-04-21	134.3	-1.6	RSSD
579	-157.1	32.2	0.0	2012-04-21	134.3	-1.6	GTBY
580	121.8	-62.7	0.2	2012-04-21	134.3	-1.6	HOPE
581	-155.5	34.4	0.2	2012-04-21	134.3	-1.6	SDDR
582	-169.8	-65.2	0.2	2012-04-21	134.3	-1.6	CPUP
583	-179.6	50.3	0.1	2012-04-28	-174.7	-18.7	KONO
584	-143.7	9.5	-0.0	2012-04-28	-174.7	-18.7	ANMO
585	-140.3	54.0	-0.2	2012-04-28	-174.7	-18.7	PAB
586	-132.4	18.3	-0.1	2012-04-28	-174.7	-18.7	HRV
587	-167.1	36.1	0.2	2012-04-28	-174.7	-18.7	ALE
588	-127.2	20.5	0.2	2012-05-28	-63.1	-28.0	MAJO
589	-3.7	-4.0	0.3	2012-05-28	-63.1	-28.0	UOSS
590	89.3	-29.1	0.3	2012-07-28	153.2	-4.7	TSUM
591	-159.6	-43.1	-0.1	2012-08-26	126.8	2.2	LPAZ
592	79.9	-17.5	-1.2	2012-08-26	126.8	2.2	LBTB
593	165.9	-59.7	-0.4	2012-08-26	126.8	2.2	PLCA
594	80.9	-20.2	0.3	2012-08-26	126.8	2.2	BOSA
595	-139.6	24.7	-0.7	2012-08-27	-88.6	12.1	WAKE
596	-51.1	33.3	0.1	2012-08-30	-10.6	71.4	SAML
597	-159.1	34.4	0.1	2012-08-31	126.6	10.8	JTS
598	-55.8	62.6	-0.3	2012-09-05	-85.3	10.1	BRVK
599	-44.1	49.8	-0.2	2012-09-30	-76.4	1.9	ARU
600	-23.3	1.1	-0.2	2012-09-30	-76.4	1.9	MBAR
601	-33.7	-22.1	0.1	2012-09-30	-76.4	1.9	SUR
602	-119.1	-30.9	-0.4	2012-09-30	-76.4	1.9	SNZO
603	-29.4	-17.8	0.0	2012-09-30	-76.4	1.9	LBTB
604	-157.1	13.6	-0.2	2012-10-09	153.7	-60.3	SFJD
605	-152.5	-44.1	0.1	2012-10-12	134.0	-4.9	LPAZ
606	179.7	-59.2	0.1	2012-10-12	134.0	-4.9	PLCA

Measurement Index	Bounce Point (Longitude°)	Bounce Point (Latitude°)	$S_{\text{LAB}}S$ Amplitude	Earthquake Date	Earthquake (Longitude°)	Earthquake (Latitude°)	Station Name
607	64.8	2.5	0.1	2012-10-12	134.0	-4.9	DBIC
608	-146.2	-39.0	-0.5	2012-10-12	134.0	-4.9	SAML
609	-151.8	-14.2	0.4	2012-10-24	-85.3	10.1	WRAB
610	-34.8	-15.9	-0.2	2012-10-24	-85.3	10.1	BOSA
611	-128.0	26.5	-0.0	2012-10-24	-85.3	10.1	MIDW
612	-160.7	29.5	0.1	2012-10-24	-85.3	10.1	DAV
613	107.0	-29.6	0.1	2012-11-11	95.9	23.0	VNDA
614	80.2	-43.5	0.2	2012-11-11	95.9	23.0	PMSA
615	49.9	86.2	-0.2	2012-11-11	95.9	23.0	DWPF
616	151.0	33.9	0.3	2012-11-11	95.9	23.0	POHA
617	-165.2	30.0	-0.2	2012-11-11	-92.2	14.1	DAV
618	-158.9	50.6	-0.2	2012-11-11	-92.2	14.1	TATO
619	-152.1	-32.1	0.1	2012-11-11	-92.2	14.1	NWAO
620	-151.3	-6.1	-0.0	2012-11-11	-92.2	14.1	CTAO
621	-162.3	-12.6	-0.4	2012-11-11	-92.2	14.1	MBWA
622	155.4	-20.3	0.1	2012-11-16	155.4	49.3	QSPA
623	64.8	-27.7	0.4	2012-12-10	129.8	-6.5	SHEL
624	80.5	-16.9	0.5	2012-12-10	129.8	-6.5	LSZ
625	58.4	-22.4	0.1	2012-12-10	129.8	-6.5	ASCN
626	161.6	42.0	-0.0	2012-12-21	167.3	-14.3	KBS
627	95.9	-49.0	0.1	2012-12-21	167.3	-14.3	TSUM
628	165.8	23.8	0.0	2013-01-05	-134.7	55.4	WRAB
629	-91.7	10.6	0.1	2013-01-05	-134.7	55.4	TRQA
630	-67.8	34.0	-0.0	2013-01-05	-134.7	55.4	RCBR
631	-127.9	21.9	-0.3	2013-01-30	-70.7	-28.1	ERM
632	-174.8	-50.6	0.1	2013-01-30	-70.7	-28.1	DAV
633	-19.2	33.0	0.2	2013-01-30	-70.7	-28.1	WMQ
634	-0.9	-32.8	0.2	2013-01-30	-70.7	-28.1	MSEY
635	-28.4	30.2	0.2	2013-01-30	-70.7	-28.1	BRVK
636	-146.5	14.1	-0.1	2013-01-30	-70.7	-28.1	SSE
637	35.2	-39.9	0.2	2013-01-30	-70.7	-28.1	CHTO
638	-126.3	-64.7	0.0	2013-01-30	-70.7	-28.1	TAU
639	87.5	17.5	0.0	2013-02-02	143.1	42.8	ABPO
640	-149.0	22.2	0.2	2013-02-07	165.7	-11.0	WCI
641	100.4	-13.7	-0.3	2013-02-07	165.7	-11.0	KMBO
642	-169.7	-54.6	0.1	2013-02-07	165.7	-11.0	PMSA
643	110.0	-13.5	-0.0	2013-02-07	165.7	-11.0	MSEY
644	-142.5	15.2	0.3	2013-02-07	165.7	-11.0	DWPF
645	114.2	11.9	0.3	2013-02-07	165.7	-11.0	UOSS
646	-148.8	22.2	0.2	2013-02-08	166.0	-10.8	WCI
647	-132.4	-27.9	-0.0	2013-02-08	166.0	-10.8	LPAZ
648	133.1	23.3	0.0	2013-02-08	166.0	-10.8	MAKZ
649	-145.8	-44.8	-0.2	2013-02-08	166.0	-10.8	PLCA
650	-136.7	8.9	-0.6	2013-02-08	166.0	-10.8	GTBY
651	-132.0	-2.1	-0.1	2013-02-08	166.0	-10.8	SDV
652	134.0	26.1	0.1	2013-02-08	166.0	-10.8	KURK
653	98.4	-32.8	0.2	2013-02-08	166.0	-10.8	LSZ
654	-147.6	26.2	0.3	2013-02-08	166.0	-10.8	SSPA
655	-134.7	8.4	-0.4	2013-02-08	166.0	-10.8	SDDR
656	-132.0	8.2	-0.7	2013-02-08	166.0	-10.8	SJG
657	-137.4	7.0	-0.3	2013-02-08	166.0	-10.8	MTDJ

Measurement Index	Bounce Point (Longitude°)	Bounce Point (Latitude°)	$S_{\mathrm{LAB}}S$ Amplitude	Earthquake Date	Earthquake (Longitude°)	Earthquake (Latitude°)	Station Name
658	-142.9	7.7	-0.1	2013-02-08	166.0	-10.8	TEIG
659	-132.3	-42.1	0.1	2013-02-08	166.0	-10.8	CPUP
660	-163.1	29.2	0.5	2013-02-08	166.0	-10.9	FFC
661	-136.7	8.8	0.6	2013-02-08	166.0	-10.9	GTBY
662	134.0	26.1	0.2	2013-02-08	166.0	-10.9	KURK
663	130.5	39.7	0.3	2013-02-08	166.0	-10.9	OBN
664	-89.0	-46.0	0.0	2013-02-09	-77.4	1.1	VNDA
665	-26.4	-11.5	-0.0	2013-02-09	-77.4	1.1	LSZ
666	-20.9	24.4	0.4	2013-02-09	-77.4	1.1	RAYN
667	-124.0	-43.0	0.5	2013-02-09	-77.4	1.1	TAU
668	-29.9	-18.6	-0.0	2013-02-09	-77.4	1.1	LBTB
669	-135.6	10.9	0.2	2013-02-09	165.7	-11.0	GRTK
670	-169.6	-54.6	-0.0	2013-02-09	165.7	-11.0	PMSA
671	-142.5	15.2	0.2	2013-02-09	165.7	-11.0	DWPF
672	-147.8	26.2	-0.0	2013-02-09	165.7	-11.0	SSPA
673	95.6	-44.5	-0.2	2013-02-09	165.7	-11.0	TSUM
674	-153.9	8.5	-0.1	2013-02-09	165.7	-11.0	SLBS
675	102.0	-43.5	0.2	2013-02-09	165.7	-11.0	LBTB
676	-134.5	28.8	-0.1	2013-02-14	142.5	67.6	RPN
677	-34.6	29.0	-0.5	2013-02-14	142.5	67.6	HOPE
678	-34.9	53.3	0.4	2013-02-14	142.5	67.6	RCBR
679	-125.0	12.3	0.3	2013-02-28	157.3	51.0	PLCA
680	-56.6	59.0	-0.0	2013-02-28	157.3	51.0	RCBR
681	-170.5	-26.0	-0.2	2013-04-06	138.5	-3.5	RPN
682	69.9	-29.1	0.3	2013-04-06	138.5	-3.5	SHEL
683	87.7	-31.7	0.1	2013-04-06	138.5	-3.5	SUR
684	-154.5	-44.0	0.2	2013-04-06	138.5	-3.5	LVC
685	63.1	-23.1	0.1	2013-04-06	138.5	-3.5	ASCN
686	-160.9	-61.0	0.4	2013-04-06	138.5	-3.5	CPUP
687	169.5	-64.7	-0.2	2013-04-14	154.6	-6.5	HOPE
688	75.0	0.5	-0.2	2013-04-14	154.6	-6.5	DBIC
689	-149.9	22.0	-0.6	2013-04-14	154.6	-6.5	DWPF
690	-151.3	24.4	0.0	2013-04-16	142.5	-3.2	GTBY
691	83.2	-23.2	0.0	2013-04-16	142.5	-3.2	TSUM
692	156.7	36.4	0.0	2013-04-20	102.9	30.3	POHA
693	-158.5	-46.8	0.2	2013-04-23	152.1	-3.9	PLCA
694	-164.0	23.5	-0.1	2013-04-23	152.1	-3.9	ANMO
695	96.0	-32.9	0.5	2013-04-23	152.1	-3.9	BOSA
696	-123.1	-50.5	0.1	2013-04-23	152.1	-3.9	RCBR
697	92.0	-19.8	-0.3	2013-04-23	152.1	-3.9	LSZ
698	-151.6	25.3	-0.1	2013-04-23	152.1	-3.9	DWPF
699	88.6	-27.8	-0.0	2013-04-23	152.1	-3.9	TSUM
700	94.3	-29.7	0.4	2013-04-23	152.1	-3.9	LBTB
701	-164.7	50.1	0.2	2013-05-14	145.3	18.7	WCI
702	178.5	50.2	-0.4	2013-05-14	145.3	18.7	FFC
703	69.6	6.0	0.2	2013-05-14	145.3	18.7	SHEL
704	-136.8	10.4	0.1	2013-05-23	-177.2	-23.0	WCI
705	-124.2	-1.5	-0.0	2013-05-23	-177.2	-23.0	GRTK
706	104.9	-21.9	-0.8	2013-05-23	-177.2	-23.0	FURI
707	51.8	-22.7	0.0	2013-06-13	107.2	-10.0	SHEL
708	-153.1	-11.4	0.3	2013-06-15	-86.9	11.8	WRAB

Measurement Index	Bounce Point (Longitude°)	Bounce Point (Latitude°)	$S_{\mathrm{LAB}}S$ Amplitude	Earthquake Date	Earthquake (Longitude°)	Earthquake (Latitude°)	Station Name
709	-49.1	-45.0	0.6	2013-06-24	-42.6	10.7	VNDA
710	-26.4	-48.3	-0.2	2013-06-24	-42.6	10.7	CASY
711	-42.6	-39.7	0.2	2013-06-24	-42.6	10.7	QSPA
712	-108.1	9.2	0.0	2013-06-24	-42.6	10.7	KNTN
713	81.2	-44.5	0.0	2013-07-07	153.9	-3.9	SHEL
714	-133.8	-8.0	-0.1	2013-07-07	153.9	-3.9	PTGA
715	179.4	-54.0	0.3	2013-07-15	-25.1	-60.9	KWAJ
716	-134.3	-2.7	0.5	2013-07-21	174.3	-41.7	WCI
717	157.4	10.9	0.1	2013-07-21	174.3	-41.7	YAK
718	147.2	34.1	0.0	2013-07-21	174.3	-41.7	KONO
719	-150.4	8.6	0.2	2013-07-21	174.3	-41.7	FFC
720	-134.2	-4.3	0.1	2013-07-21	174.3	-41.7	WVT
721	-131.2	-0.9	-0.2	2013-07-21	174.3	-41.7	SSPA
722	87.7	-36.5	0.1	2013-07-21	174.3	-41.7	FURI
723	-136.8	-2.7	-0.1	2013-07-21	174.3	-41.7	CCM
724	-31.0	-18.0	0.3	2013-08-13	-78.2	5.8	BOSA
725	-26.2	46.0	-0.6	2013-08-13	-78.2	5.8	ABKT
726	-45.6	53.0	0.3	2013-08-13	-78.2	5.8	ARU
727	-18.3	-14.2	-0.5	2013-08-13	-78.2	5.8	ABPO
728	-132.8	6.1	-0.4	2013-08-13	-78.2	5.8	TARA
729	-134.3	-2.7	0.5	2013-08-16	174.2	-41.7	WCI
730	-150.4	8.6	0.6	2013-08-16	174.2	-41.7	FFC
731	-145.9	1.6	0.1	2013-08-16	174.2	-41.7	RSSD
732	-107.0	-39.4	0.3	2013-08-16	174.2	-41.7	PTGA
733	146.2	26.6	0.1	2013-08-16	174.2	-41.7	LVZ
734	-134.2	-4.3	-0.0	2013-08-16	174.2	-41.7	WVT
735	-82.9	-56.3	0.2	2013-08-16	174.2	-41.7	RCBR
736	-38.0	-71.1	0.4	2013-08-16	174.2	-41.7	ASCN
737	142.6	6.0	-0.3	2013-08-16	174.2	-41.7	TLY
738	-129.7	-16.0	-0.0	2013-08-16	174.2	-41.7	TEIG
739	-134.9	-11.2	0.2	2013-08-30	-175.4	51.6	PMSA
740	-120.8	32.3	0.4	2013-08-30	-175.4	51.6	PAYG
741	-156.9	-55.7	-0.2	2013-09-01	128.2	-7.4	LPAZ
742	176.1	57.9	-0.3	2013-09-01	128.2	-7.4	BBSR
743	-164.2	-60.2	0.2	2013-09-01	128.2	-7.4	LVC
744	-149.0	-55.4	-0.1	2013-09-01	128.2	-7.4	SAML
745	-120.6	32.2	0.1	2013-09-04	-174.7	51.6	PAYG
746	-174.8	-19.2	0.2	2013-09-04	-174.7	51.6	QSPA
747	-122.7	9.8	0.3	2013-09-25	-74.6	-15.8	MIDW
748	-16.6	47.4	-0.1	2013-09-28	65.6	27.3	BCIP
749	8.7	-17.3	0.1	2013-09-28	65.6	27.3	PLCA
750	-22.2	0.6	-0.0	2013-09-28	65.6	27.3	RPN
751	-27.6	47.3	-0.1	2013-09-28	65.6	27.3	PAYG
752	131.4	13.6	-0.1	2013-09-28	65.6	27.3	AFI
753	-148.9	14.7	0.6	2013-09-30	-178.4	-30.9	FFC
754	-111.6	14.0	-0.0	2013-09-30	-178.4	-30.9	CMLA
755	-132.4	7.5	0.3	2013-09-30	-178.4	-30.9	SSPA
756	-130.8	9.5	-0.0	2013-09-30	-178.4	-30.9	HRV
757	-158.6	38.2	0.2	2013-09-30	-178.4	-30.9	BORG
758	60.7	-7.1	0.4	2013-10-15	124.1	9.9	SHEL
759	130.2	-52.3	-0.2	2013-10-15	124.1	9.9	PMSA

Measurement Index	Bounce Point (Longitude°)	Bounce Point (Latitude°)	$S_{\mathrm{LAB}}S$ Amplitude	Earthquake Date	Earthquake (Longitude°)	Earthquake (Latitude°)	Station Name
760	72.5	-7.8	0.5	2013-10-15	124.1	9.9	TSUM
761	175.8	50.4	0.5	2013-10-19	-110.3	26.1	QIZ
762	168.6	58.4	0.3	2013-10-19	-110.3	26.1	CHTO
763	-26.1	49.3	0.1	2013-10-19	-110.3	26.1	FURI
764	-123.0	-29.6	0.2	2013-10-19	-110.3	26.1	SBA
765	-124.0	-40.0	-0.1	2013-10-24	-12.8	-58.1	POHA
766	-133.1	47.6	0.2	2013-10-25	144.7	37.2	BCIP
767	-158.2	8.3	-0.2	2013-10-25	144.7	37.2	RPN
768	-130.6	18.5	-0.8	2013-10-31	-71.6	-30.3	ERM
769	-158.9	-64.1	0.2	2013-10-31	-71.6	-30.3	WRAB
770	168.4	-69.2	-0.4	2013-10-31	-71.6	-30.3	KAPI
771	-153.0	3.6	-0.3	2013-10-31	-71.6	-30.3	SSE
772	-125.6	-32.3	0.1	2013-10-31	-71.6	-30.3	AFI
773	42.5	-46.7	-0.1	2013-10-31	-71.6	-30.3	CHTO
774	-149.5	-55.3	-0.6	2013-10-31	-71.6	-30.3	CTAO
775	-20.9	-11.1	-0.9	2013-11-16	-47.1	-60.3	PAB
776	26.9	-43.2	0.0	2013-11-16	-47.1	-60.3	MSEY
777	-124.9	-9.5	-0.7	2013-11-16	-47.1	-60.3	ADK
778	-35.2	2.3	-0.7	2013-11-16	-47.1	-60.3	BORG
779	-31.6	10.4	-0.1	2013-11-16	-47.1	-60.3	KBS
780	140.2	20.3	-0.1	2013-11-23	-176.5	-17.1	AAK
781	-126.8	12.8	0.4	2013-11-23	-176.5	-17.1	BBSR
782	109.0	-13.6	0.1	2013-11-23	-176.5	-17.1	FURI
783	-171.9	-28.2	0.1	2013-11-25	-55.0	-53.9	ERM
784	71.0	-42.2	-0.0	2013-11-25	-55.0	-53.9	KMI
785	-92.8	-5.7	-0.3	2013-11-25	-55.0	-53.9	COR
786	3.6	-10.5	-0.4	2013-11-25	-55.0	-53.9	GNI
787	-26.7	10.2	0.3	2013-11-25	-55.0	-53.9	KEV
788	-120.8	-24.9	0.8	2013-11-25	-55.0	-53.9	POHA
789	-91.5	-11.8	0.3	2013-11-25	-55.0	-53.9	PFO
790	-118.3	-2.1	0.1	2013-11-25	-55.0	-53.9	ADK
791	115.1	-50.3	-0.0	2013-11-25	-55.0	-53.9	TATO
792	97.4	-19.0	0.1	2014-01-01	167.2	-13.9	MBAR
793	-134.1	3.7	0.4	2014-02-02	-177.9	-32.9	WCI
794	-121.1	-0.6	-0.3	2014-02-02	-177.9	-32.9	BBSR
795	-128.1	39.3	-0.3	2014-02-02	-177.9	-32.9	PAB
796	109.3	-36.8	0.1	2014-02-02	-177.9	-32.9	MSEY
797	96.7	-33.4	-0.3	2014-02-02	-177.9	-32.9	FURI
798	100.5	-18.7	-0.1	2014-02-07	167.4	-15.1	KMBO
799	161.7	41.9	0.1	2014-02-07	167.4	-15.1	KBS
800	102.2	-47.9	0.3	2014-02-07	167.4	-15.1	LBTB
801	7.3	82.6	-0.1	2014-02-12	82.6	35.9	WCI
802	-1.4	83.4	-0.1	2014-02-12	82.6	35.9	WVT
803	143.3	26.0	0.1	2014-02-12	82.6	35.9	KNTN
804	-135.2	-21.5	-0.1	2014-02-18	-58.9	14.7	WRAB
805	-152.3	51.6	-0.1	2014-03-02	127.4	27.4	TGUH
806	-95.4	-6.5	-0.4	2014-03-10	-125.1	40.8	EFI
807	-53.9	23.2	0.4	2014-03-10	-125.1	40.8	SHEL
808	-58.8	27.1	0.2	2014-03-10	-125.1	40.8	ASCN
809	-168.0	-1.4	0.3	2014-03-10	-125.1	40.8	TAU
810	-35.7	29.6	-0.1	2014-03-10	-125.1	40.8	TSUM

Measurement Index	Bounce Point (Longitude°)	Bounce Point (Latitude°)	$S_{\mathrm{LAB}}S$ Amplitude	Earthquake Date	Earthquake (Longitude°)	Earthquake (Latitude°)	Station Name
811	-14.3	-17.6	-0.2	2014-03-16	-70.7	-20.0	KMBO
812	-31.5	40.2	-0.5	2014-03-16	-70.7	-20.0	KURK
813	-130.7	40.6	-0.1	2014-03-16	-70.7	-20.0	SSE
814	-11.5	-34.5	-0.2	2014-03-16	-70.7	-20.0	ABPO
815	-121.8	-60.5	-0.1	2014-03-16	-70.7	-20.0	TAU
816	-26.1	42.8	0.1	2014-03-16	-70.7	-20.0	WMQ
817	-39.1	17.7	-0.2	2014-04-03	-70.6	-20.3	BFO
818	-26.9	39.9	-0.1	2014-04-03	-70.6	-20.3	MAKZ
819	-19.1	31.5	0.0	2014-04-03	-70.6	-20.3	AAK
820	-31.8	36.7	0.1	2014-04-03	-70.6	-20.3	BRVK
821	-161.1	31.3	-0.6	2014-04-11	-85.9	11.6	DAV
822	-22.0	-9.1	0.0	2014-04-11	-85.9	11.6	ABPO
823	-56.9	63.4	-0.2	2014-04-11	-85.9	11.6	BRVK
824	-139.6	49.0	0.4	2014-04-11	-85.9	11.6	MAJO
825	-147.0	-9.4	-0.0	2014-04-11	-85.9	11.6	CTAO
826	-133.9	-2.7	-0.0	2014-04-12	162.2	-11.3	SDV
827	-114.4	-43.8	0.1	2014-04-12	162.2	-11.3	RCBR
828	96.3	-31.1	0.1	2014-04-12	162.2	-11.3	LSZ
829	106.4	-26.7	0.1	2014-04-12	162.2	-11.3	ABPO
830	-134.1	8.3	0.3	2014-04-12	162.2	-11.3	SJG
831	164.8	51.9	0.4	2014-04-12	162.2	-11.3	BORG
832	-132.0	8.2	-0.1	2014-04-13	162.1	-11.5	ANWB
833	-139.4	6.8	0.2	2014-04-13	162.1	-11.5	MTDJ
834	95.2	-56.2	0.1	2014-04-15	8.7	-53.5	WRAB
835	111.0	-55.3	-0.0	2014-04-15	8.7	-53.5	PMG
836	-30.7	20.9	-0.5	2014-04-15	8.7	-53.5	COLA
837	-166.7	-54.9	-0.1	2014-04-15	8.7	-53.5	JOHN
838	-131.9	-49.2	0.0	2014-04-15	8.7	-53.5	POHA
839	117.4	-15.6	0.0	2014-04-15	8.7	-53.5	ADK
840	84.9	-8.2	0.2	2014-04-15	8.7	-53.5	YSS
841	82.4	-23.7	0.2	2014-04-15	8.7	-53.5	TATO
842	-158.3	7.1	-0.8	2014-04-18	-101.0	17.4	PMG
843	92.6	-7.7	-0.5	2014-04-19	155.1	-6.7	MBAR
844	177.1	-54.9	0.2	2014-04-19	155.1	-6.7	PMSA
845	-139.0	15.7	0.1	2014-04-19	155.0	-6.8	SJG
846	-156.8	11.2	-0.1	2014-04-24	-127.7	49.6	RAO
847	171.4	21.6	0.3	2014-04-24	-127.7	49.6	WRAB
848	-96.7	5.1	0.4	2014-04-24	-127.7	49.6	PLCA
849	-127.8	-20.2	-0.9	2014-04-24	-127.7	49.6	QSPA
850	130.1	15.3	0.0	2014-05-01	170.3	-21.4	AAK
851	165.0	38.9	0.1	2014-05-01	170.3	-21.4	KBS
852	166.9	45.2	-0.6	2014-05-04	179.1	-24.6	KONO
853	159.8	37.0	0.2	2014-05-04	179.1	-24.6	LVZ
854	103.8	-22.5	0.0	2014-05-04	179.1	-24.6	FURI
855	-26.6	58.5	0.1	2014-05-13	-82.3	7.2	NIL
856	-158.4	27.5	-0.3	2014-05-13	-82.3	7.2	DAV
857	56.0	-60.1	-0.1	2014-06-14	91.1	-10.1	EFI
858	139.8	5.1	-0.1	2014-06-14	91.1	-10.1	JOHN
859	-134.9	5.9	-0.5	2014-06-23	-177.7	-30.0	WCI
860	-112.1	15.6	0.4	2014-06-23	-177.7	-30.0	CMLA
861	-132.3	8.2	-0.2	2014-06-23	-177.7	-30.0	SSPA

Measurement Index	Bounce Point (Longitude°)	Bounce Point (Latitude°)	$S_{\mathrm{LAB}}S$ Amplitude	Earthquake Date	Earthquake (Longitude°)	Earthquake (Latitude°)	Station Name
862	50.9	-9.8	-0.0	2014-06-29	-28.4	-55.5	ULN
863	27.4	-37.1	0.1	2014-06-29	-28.4	-55.5	MSEY
864	62.1	-33.7	0.0	2014-06-29	-28.4	-55.5	CHTO
865	-118.4	-20.8	-0.0	2014-06-29	-175.5	-15.0	SAML
866	-158.5	29.6	-0.8	2014-07-04	152.8	-6.2	WCI
867	88.8	-30.6	0.2	2014-07-04	152.8	-6.2	TSUM
868	-172.6	-30.7	-0.0	2014-07-11	142.4	37.0	EFI
869	-138.0	46.7	-0.1	2014-07-11	142.4	37.0	JTS
870	-104.7	-35.5	-0.2	2014-07-21	-178.4	-19.8	RCBR
871	164.9	-53.1	0.2	2014-08-03	146.2	0.8	PMSA
872	-168.4	25.4	0.3	2014-08-03	146.2	0.8	TUC
873	-118.5	-42.8	-0.4	2014-08-24	-73.6	-14.6	SNZO
874	-23.1	-22.9	0.1	2014-08-24	-73.6	-14.6	LSZ
875	-14.7	-31.4	-0.0	2014-08-24	-73.6	-14.6	ABPO
876	-123.0	17.1	0.0	2014-10-09	-110.8	-32.1	COLA
877	-143.7	19.7	0.6	2014-10-09	-110.8	-32.1	MA2
878	-36.1	-14.3	0.1	2014-10-14	-88.1	12.5	BOSA
879	-162.7	30.8	-0.6	2014-10-14	-88.1	12.5	DAV
880	-142.0	48.5	0.1	2014-10-14	-88.1	12.5	MAJO
881	-155.2	52.7	0.3	2014-10-14	-88.1	12.5	TATO
882	-126.1	0.9	-0.0	2014-11-01	-177.8	-19.7	GRTK
883	133.4	29.6	0.2	2014-11-01	-177.8	-19.7	KIV
884	143.9	19.4	-0.4	2014-11-01	-177.8	-19.7	MAKZ
885	101.0	-36.0	-0.3	2014-11-01	-177.8	-19.7	MBAR
886	139.0	17.9	-0.0	2014-11-01	-177.8	-19.7	AAK
887	153.0	16.3	-0.4	2014-11-01	-177.8	-19.7	ULN
888	147.2	31.4	0.5	2014-11-01	-177.8	-19.7	ARU
889	145.3	26.0	-0.0	2014-11-01	-177.8	-19.7	BRVK
890	107.4	-17.1	-0.1	2014-11-01	-177.8	-19.7	FURI
891	-134.9	17.5	0.1	2014-11-01	-177.8	-19.7	HRV
892	75.6	-40.6	0.2	2014-11-07	148.2	-6.0	SHEL
893	67.8	-38.9	0.0	2014-11-07	148.2	-6.0	ASCN
894	-148.4	10.8	0.1	2014-11-16	179.7	-37.6	FFC
895	-153.5	3.9	0.0	2014-11-16	179.7	-37.6	COR
896	-103.2	0.2	-0.2	2014-11-16	179.7	-37.6	CMLA
897	102.2	-52.7	-0.1	2014-11-16	179.7	-37.6	ABPO
898	-127.3	-7.3	0.2	2014-11-16	179.7	-37.6	DWPF
899	-130.7	2.4	0.5	2014-11-16	179.7	-37.6	SSPA
900	91.9	-36.3	-0.5	2014-11-16	179.7	-37.6	FURI
901	-135.8	-5.2	0.2	2014-11-16	179.7	-37.6	HKT
902	-173.1	43.2	0.2	2014-11-16	179.7	-37.6	ESK
903	-179.9	43.2	-0.2	2014-12-02	123.1	6.2	HKT
904	92.3	-7.5	0.0	2014-12-07	154.5	-6.5	MBAR
905	-94.9	-43.4	0.4	2015-01-07	-82.7	5.9	VNDA
906	-33.6	-18.8	-0.1	2015-01-07	-82.7	5.9	BOSA
907	147.5	39.8	0.2	2015-01-23	168.5	-17.0	LVZ
908	-126.1	-27.9	0.2	2015-01-23	168.5	-17.0	SAML
909	-145.2	20.2	0.5	2015-01-23	168.5	-17.0	SSPA
910	175.0	37.8	0.0	2015-01-23	168.5	-17.0	ALE
911	132.4	36.0	-0.3	2015-01-23	168.5	-17.0	OBN
912	-144.6	23.4	-0.0	2015-01-23	168.5	-17.0	HRV

Measurement Index	Bounce Point (Longitude°)	Bounce Point (Latitude°)	$S_{\mathrm{LAB}}S$ Amplitude	Earthquake Date	Earthquake (Longitude°)	Earthquake (Latitude°)	Station Name
913	-148.5	15.7	0.2	2015-01-23	168.5	-17.0	CCM
914	176.2	48.0	0.3	2015-01-23	168.5	-17.0	BORG
915	-43.4	29.5	0.5	2015-02-11	-66.7	-23.1	LVZ
916	-124.9	41.8	0.2	2015-02-11	-66.7	-23.1	SSE
917	-95.3	21.9	-0.0	2015-02-11	-66.7	-23.1	KDAK
918	-171.0	44.9	-0.2	2015-02-27	122.5	-7.3	GRTK
919	-167.7	35.0	0.1	2015-02-27	122.5	-7.3	GTBY
920	160.1	7.5	-0.1	2015-02-27	122.5	-7.3	POHA
921	-170.2	22.6	-0.1	2015-02-27	122.5	-7.3	TEIG
922	-140.8	19.4	0.2	2015-03-29	152.6	-4.7	SJG
923	103.9	-34.4	-0.1	2015-03-30	-173.0	-15.5	MBAR
924	-159.1	53.1	0.3	2015-03-30	-173.0	-15.5	ESK
925	172.5	51.6	0.1	2015-04-17	-178.6	-15.9	KONO
926	-123.6	-5.9	0.2	2015-04-17	-178.6	-15.9	SDV
927	146.3	34.7	0.1	2015-04-17	-178.6	-15.9	ARU
928	-132.7	-1.3	-0.1	2015-04-17	-178.6	-15.9	TGUH
929	-136.4	18.8	0.3	2015-04-17	-178.6	-15.9	SSPA
930	-139.2	20.2	0.3	2015-05-05	151.9	-5.5	ANWB
931	-155.9	-47.8	-0.1	2015-05-07	154.6	-7.2	PLCA
932	-119.8	-51.4	-0.2	2015-05-07	154.6	-7.2	RCBR
933	-147.4	6.6	0.2	2015-05-07	154.6	-7.2	TGUH
934	-133.2	16.8	0.1	2015-05-12	142.0	38.9	LCO
935	-129.6	44.3	0.6	2015-05-12	142.0	38.9	OTAV
936	137.6	-43.2	0.0	2015-05-12	142.0	38.9	HOPE
937	-139.3	49.3	-0.3	2015-05-12	142.0	38.9	TGUH
938	-105.7	-8.7	0.2	2015-05-19	-132.2	-54.3	WCI
939	112.6	-33.2	-0.5	2015-05-19	-132.2	-54.3	NIL
940	-40.8	-41.4	0.3	2015-05-19	-132.2	-54.3	DBIC
941	-50.0	-47.1	-0.0	2015-05-19	-132.2	-54.3	ASCN
942	-122.9	-10.5	-0.2	2015-05-19	-132.2	-54.3	PFO
943	-108.5	-8.7	0.2	2015-05-19	-132.2	-54.3	CCM
944	41.4	-51.0	0.1	2015-05-19	-132.2	-54.3	RAYN
945	-16.1	-65.1	0.2	2015-05-19	-132.2	-54.3	TSUM
946	173.9	-25.8	-0.1	2015-05-19	-132.2	-54.3	GUMO
947	103.2	-45.3	0.0	2015-05-20	164.2	-10.9	BOSA
948	-132.9	-2.2	0.1	2015-05-20	164.2	-10.9	SDV
949	-142.1	2.7	-0.5	2015-05-20	164.2	-10.9	TGUH
950	-148.9	26.7	0.2	2015-05-20	164.2	-10.9	SSPA
951	-160.1	14.6	0.2	2015-05-20	164.2	-10.9	PFO
952	-154.8	8.7	0.2	2015-05-20	164.2	-10.9	SLBS
953	-164.8	29.6	0.3	2015-05-22	163.7	-11.1	FFC
954	107.2	-27.0	0.2	2015-05-22	163.7	-11.1	ABPO
955	-143.7	15.5	0.0	2015-05-22	163.7	-11.1	DWPF
956	-149.2	26.8	0.1	2015-05-22	163.7	-11.1	SSPA
957	-160.3	14.5	0.1	2015-05-22	163.7	-11.1	PFO
958	-135.9	8.5	0.3	2015-05-22	163.7	-11.1	SDDR
959	-155.0	8.6	-0.0	2015-05-22	163.7	-11.1	SLBS
960	-150.6	22.7	-0.2	2015-05-22	163.2	-11.1	WCI
961	95.8	-14.3	-0.0	2015-05-22	163.2	-11.1	MBAR
962	-138.2	9.0	0.5	2015-05-22	163.2	-11.1	GTBY
963	-178.5	46.4	0.1	2015-05-22	163.2	-11.1	SFJD

Measurement Index	Bounce Point (Longitude°)	Bounce Point (Latitude°)	$S_{\mathrm{LAB}}S$ Amplitude	Earthquake Date	Earthquake (Longitude°)	Earthquake (Latitude°)	Station Name
964	169.2	41.7	0.1	2015-05-22	163.2	-11.1	ALE
965	149.5	15.9	-0.3	2015-05-29	-156.5	56.7	NWAO
966	85.1	0.5	-0.4	2015-05-30	140.5	27.8	BOSA
967	-137.4	5.6	0.0	2015-05-30	140.5	27.8	CPUP
968	83.6	-3.8	-0.3	2015-06-23	139.7	27.7	SUR
969	-153.4	23.3	0.1	2015-07-10	158.4	-9.3	WVT
970	-132.3	-24.4	0.3	2015-07-10	158.4	-9.3	SAML
971	94.7	-27.4	0.3	2015-07-10	158.4	-9.3	LSZ
972	104.6	-24.1	-0.3	2015-07-10	158.4	-9.3	ABPO
973	-147.1	18.3	-0.2	2015-07-10	158.4	-9.3	DWPF
974	-153.5	30.0	-0.5	2015-07-10	158.4	-9.3	SSPA
975	-146.5	-44.8	0.1	2015-07-18	165.1	-10.4	PLCA
976	-139.1	24.4	-0.0	2015-07-18	165.1	-10.4	BBSR
977	109.8	-12.9	0.4	2015-07-18	165.1	-10.4	MSEY
978	108.1	-27.0	0.4	2015-07-18	165.1	-10.4	ABPO
979	-148.3	26.8	0.3	2015-07-18	165.1	-10.4	SSPA
980	-105.9	-2.3	0.4	2015-07-27	-169.4	52.4	HOPE
981	-170.2	38.9	0.2	2015-07-27	138.5	-2.6	WCI
982	-154.1	23.8	0.2	2015-07-27	138.5	-2.6	MTDJ
983	-136.2	-0.6	0.4	2015-08-10	158.1	-9.3	SDV
984	100.7	-45.7	0.2	2015-08-10	158.1	-9.3	SUR
985	94.6	-27.2	0.2	2015-08-10	158.1	-9.3	LSZ
986	-147.3	18.3	0.2	2015-08-10	158.1	-9.3	DWPF
987	-143.7	0.9	-0.3	2015-08-12	157.9	-9.3	JTS
988	-129.9	-15.2	0.3	2015-08-12	157.9	-9.3	PTGA
989	-145.7	-8.9	-0.2	2015-08-12	157.9	-9.3	PAYG
990	-147.4	18.4	-0.3	2015-08-12	157.9	-9.3	DWPF
991	70.2	-66.0	0.1	2015-08-12	157.9	-9.3	ASCN
992	-89.0	-14.7	-0.2	2015-09-13	-109.4	25.1	EFI
993	179.3	22.7	-0.3	2015-09-13	-109.4	25.1	KAPI
994	-176.1	57.3	0.1	2015-09-13	-109.4	25.1	ENH
995	-152.5	50.3	-0.2	2015-09-13	-109.4	25.1	YSS
996	0.9	-36.0	-0.2	2015-09-21	-71.4	-31.7	MSEY
997	13.6	-48.1	-0.6	2015-09-21	-71.4	-31.7	DGAR
998	-129.8	-66.0	0.3	2015-09-21	-71.4	-31.7	TAU
999	-155.6	15.6	-0.0	2015-09-24	131.3	-0.6	BCIP
1000	-155.3	-41.2	0.3	2015-09-24	131.3	-0.6	LPAZ
1001	-126.8	-3.4	-0.1	2015-10-20	167.3	-14.9	GRGR
1002	-135.6	4.8	0.5	2015-10-20	167.3	-14.9	GTBY
1003	-136.9	19.0	0.3	2015-10-20	167.3	-14.9	BBSR
1004	134.8	23.6	0.1	2015-10-20	167.3	-14.9	KURK
1005	98.3	-37.6	0.1	2015-10-20	167.3	-14.9	LSZ
1006	-141.2	11.4	0.4	2015-10-20	167.3	-14.9	DWPF
1007	-130.7	3.5	-0.2	2015-10-20	167.3	-14.9	SJG
1008	39.6	-27.2	-0.2	2015-10-26	70.4	36.5	PMSA
1009	70.5	-26.1	-0.0	2015-10-26	70.4	36.5	QSPA
1010	176.9	42.5	0.1	2015-11-04	124.9	-8.3	WCI
1011	61.8	7.1	0.0	2015-11-04	124.9	-8.3	KOWA
1012	-147.6	5.8	0.4	2015-11-13	128.9	31.0	LCO
1013	-170.6	-25.4	-0.1	2015-11-13	128.9	31.0	PLCA
1014	82.0	-57.9	0.2	2015-11-18	158.4	-8.9	SHEL

Measurement Index	Bounce Point (Longitude°)	Bounce Point (Latitude°)	$S_{\mathrm{LAB}}S$ Amplitude	Earthquake Date	Earthquake (Longitude°)	Earthquake (Latitude°)	Station Name
1015	-147.2	18.6	-0.3	2015-11-18	158.4	-8.9	DWPF
1016	163.9	43.1	0.1	2015-11-18	158.4	-8.9	ALE
1017	88.0	-24.1	0.0	2015-12-07	72.8	38.2	SBA
1018	-157.8	26.4	0.1	2016-01-11	126.9	3.9	BCIP
1019	79.6	-16.3	-0.2	2016-01-11	126.9	3.9	LBTB
1020	-177.0	17.0	-0.1	2016-01-21	-106.9	18.8	KAPI
1021	-178.4	47.4	0.5	2016-01-21	-106.9	18.8	QIZ
1022	-54.2	19.8	-0.2	2016-01-21	-106.9	18.8	DBIC
1023	-30.0	-0.4	0.2	2016-01-21	-106.9	18.8	ABPO
1024	82.1	3.1	-0.1	2016-04-07	166.6	-14.0	KOWA
1025	40.5	-27.5	-0.0	2016-04-10	71.1	36.5	PMSA
1026	130.6	15.7	-0.3	2016-04-10	71.1	36.5	MSVF
1027	148.4	34.6	0.1	2016-04-13	94.9	23.1	KIP
1028	147.7	1.7	0.1	2016-04-13	94.9	23.1	RAR
1029	-138.2	54.4	0.1	2016-04-15	130.8	32.8	BCIP
1030	-143.4	51.4	-0.1	2016-04-15	130.8	32.8	JTS
1031	-146.6	52.5	0.4	2016-04-15	130.8	32.8	TGUH
1032	128.9	18.7	0.2	2016-04-28	167.4	-16.0	AAK
1033	133.5	26.0	-0.1	2016-04-28	167.4	-16.0	BRVK
1034	161.6	41.7	-0.2	2016-04-28	167.4	-16.0	KBS
1035	-116.3	-38.8	0.3	2016-04-29	-103.7	10.3	VNDA
1036	-115.8	-38.4	0.6	2016-04-29	-103.7	10.3	SBA
1037	-103.8	-39.9	0.0	2016-04-29	-103.7	10.3	QSPA
1038	-148.2	13.2	0.2	2016-04-29	-103.7	10.3	KWAJ
1039	-156.8	-8.5	0.2	2016-04-29	-103.7	10.3	CTAO
1040	-159.4	-13.3	-0.3	2016-05-18	-79.8	0.4	KAPI
1041	-146.8	-30.2	0.3	2016-05-18	-79.6	0.5	WRAB
1042	-50.0	58.7	-0.2	2016-05-18	-79.6	0.5	KURK
1043	-47.6	50.4	-0.4	2016-05-18	-79.6	0.5	ARU
1044	-133.0	44.5	0.0	2016-05-18	-79.6	0.5	MAJO
1045	-21.9	24.7	-0.1	2016-05-18	-79.6	0.5	RAYN
1046	-18.6	30.8	0.2	2016-05-18	-79.6	0.5	UOSS
1047	-130.6	-59.6	0.0	2016-05-18	-79.6	0.5	NWAO
1048	168.7	40.7	0.2	2016-05-28	-178.2	-22.0	KEV
1049	-132.5	3.9	0.3	2016-05-28	-178.2	-22.0	DWPF
1050	-170.7	33.9	0.0	2016-05-28	-178.2	-22.0	ALE
1051	106.5	-31.0	0.0	2016-05-28	-26.9	-56.2	YSS
1052	135.7	83.0	0.2	2016-06-01	100.7	-2.1	BCIP
1053	39.6	-65.6	-0.1	2016-06-01	100.7	-2.1	LVC
1054	-174.7	-14.2	0.1	2016-06-01	100.7	-2.1	PAYG
1055	137.2	27.7	0.7	2016-08-12	173.1	-22.5	ARU
1056	-121.5	-30.8	0.2	2016-08-12	173.1	-22.5	SAML
1057	168.3	38.8	0.2	2016-08-12	173.1	-22.5	KBS
1058	136.9	14.3	0.8	2016-08-12	173.1	-22.5	WMQ
1059	98.1	-32.6	0.1	2016-08-31	152.8	-3.7	BOSA
1060	-148.2	6.6	-0.4	2016-08-31	152.8	-3.7	JTS
1061	-145.5	-32.9	0.2	2016-08-31	152.8	-3.7	LVC
1062	-160.1	36.1	0.2	2016-08-31	152.8	-3.7	SSPA
1063	-141.9	20.5	0.1	2016-08-31	152.8	-3.7	SJG
1064	-171.1	34.2	-0.1	2016-09-24	-178.2	-19.8	ALE
1065	-171.1	50.4	0.4	2016-09-24	-178.2	-19.8	ESK

Measurement Index	Bounce Point (Longitude°)	Bounce Point (Latitude°)	$S_{\mathrm{LAB}}S$ Amplitude	Earthquake Date	Earthquake (Longitude°)	Earthquake (Latitude°)	Station Name
1066	151.3	37.0	-0.0	2016-10-19	108.2	-4.9	COR
1067	70.1	8.0	0.2	2016-10-30	13.1	42.9	NWAO
1068	-150.7	8.1	-0.0	2016-11-14	173.2	-42.6	FFC
1069	84.7	-45.1	0.1	2016-11-14	173.2	-42.6	KMBO
1070	-146.0	1.0	0.1	2016-11-14	173.2	-42.6	RSSD
1071	-134.2	-5.0	-0.1	2016-11-14	173.2	-42.6	WVT
1072	100.4	-39.4	0.0	2016-11-14	173.2	-42.6	MSEY
1073	-81.5	-57.2	0.5	2016-11-14	173.2	-42.6	RCBR
1074	-143.4	-12.0	-0.0	2016-11-14	173.2	-42.6	SLBS
1075	96.8	-20.4	0.4	2016-11-14	173.2	-42.6	RAYN
1076	105.1	-16.4	-0.9	2016-11-14	173.2	-42.6	UOSS
1077	135.5	-43.9	-0.3	2016-11-21	141.4	37.4	HOPE
1078	-137.2	48.1	-0.1	2016-11-24	-88.9	11.9	ERM
1079	-143.1	55.1	0.3	2016-11-24	-88.9	11.9	INCN
1080	-36.6	-15.1	-0.1	2016-11-24	-88.9	11.9	BOSA
1081	-152.2	72.0	-0.0	2016-11-24	-88.9	11.9	KMI
1082	-159.2	-18.0	-0.4	2016-11-24	-88.9	11.9	MBWA
1083	-14.4	30.9	0.3	2016-11-25	74.0	39.3	LPAZ
1084	50.6	87.3	-0.3	2016-11-25	74.0	39.3	RSSD
1085	-25.5	41.4	0.2	2016-11-25	74.0	39.3	NNA
1086	146.5	21.5	0.4	2016-12-06	96.2	5.3	KIP
1087	29.8	-48.4	-0.4	2016-12-06	96.2	5.3	LVC
1088	148.1	20.8	0.4	2016-12-06	96.2	5.3	POHA
1089	-175.7	13.9	0.1	2016-12-08	-126.2	40.5	CTAO
1090	98.5	-12.4	0.3	2016-12-08	161.3	-10.7	KMBO
1091	95.0	-13.3	0.2	2016-12-08	161.3	-10.7	MBAR
1092	83.5	-64.5	0.1	2016-12-08	161.3	-10.7	SHEL
1093	-130.6	2.0	0.0	2016-12-08	161.3	-10.7	GRGR
1094	96.1	-30.1	0.4	2016-12-08	161.3	-10.7	LSZ
1095	-145.2	16.3	0.0	2016-12-08	161.3	-10.7	DWPF
1096	-159.0	14.8	0.1	2016-12-08	161.3	-10.7	TUC
1097	-153.6	22.1	0.3	2016-12-08	161.3	-10.7	CCM
1098	-145.5	8.3	0.0	2016-12-08	161.3	-10.7	TEIG
1099	-166.8	30.3	0.1	2016-12-09	161.1	-10.8	FFC
1100	45.7	-39.7	-0.0	2016-12-21	127.9	-7.5	RCBR
1101	75.2	-22.5	0.0	2016-12-21	127.9	-7.5	TSUM
1102	-65.8	11.9	-0.0	2016-12-25	-73.9	-43.4	SFJD
1103	-12.2	-3.2	0.1	2016-12-25	-73.9	-43.4	GNI
1104	-121.0	-15.4	-0.7	2016-12-25	-73.9	-43.4	POHA
1105	-106.0	9.1	0.1	2016-12-25	-73.9	-43.4	KDAK
1106	-55.0	11.7	0.2	2016-12-25	-73.9	-43.4	BORG
1107	-118.1	18.8	0.1	2016-12-25	-73.9	-43.4	MA2
1108	156.2	40.7	0.6	2017-01-03	176.1	-19.4	LVZ
1109	-129.7	12.6	0.3	2017-01-03	176.1	-19.4	BBSR
1110	-161.1	38.8	-0.4	2017-01-03	176.1	-19.4	SFJD
1111	140.6	30.7	0.3	2017-01-03	176.1	-19.4	ARU
1112	-104.7	-39.0	0.2	2017-01-03	176.1	-19.4	RCBR
1113	104.0	-14.1	0.2	2017-01-03	176.1	-19.4	FURI
1114	174.9	52.6	-0.3	2017-01-03	176.1	-19.4	ESK
1115	170.6	53.8	0.1	2017-01-10	122.6	4.5	WCI
1116	99.5	-54.1	0.3	2017-01-10	122.6	4.5	HOPE

Measurement Index	Bounce Point (Longitude°)	Bounce Point (Latitude°)	$S_{\mathrm{LAB}}S$ Amplitude	Earthquake Date	Earthquake (Longitude°)	Earthquake (Latitude°)	Station Name
1117	171.6	33.9	0.0	2017-01-10	122.6	4.5	PFO
1118	179.5	42.0	0.2	2017-01-10	122.6	4.5	HKT
1119	-141.9	26.1	0.1	2017-01-19	161.3	-10.3	BBSR
1120	76.0	-15.0	0.3	2017-01-19	161.3	-10.3	DBIC
1121	131.4	-59.0	-0.3	2017-02-10	125.5	9.9	EFI
1122	79.3	-14.3	0.1	2017-02-10	125.5	9.9	BOSA
1123	-140.5	-43.8	-0.4	2017-02-21	-63.9	-19.3	PMG
1124	-25.0	54.0	0.2	2017-02-21	-63.9	-19.3	XAN
1125	-126.4	43.4	0.3	2017-02-21	-63.9	-19.3	TATO
1126	-155.0	34.2	0.6	2017-02-24	-178.8	-23.3	SFJD
1127	167.6	39.9	0.2	2017-02-24	-178.8	-23.3	KEV
1128	-102.0	-39.2	-0.5	2017-02-24	-178.8	-23.3	RCBR
1129	-135.9	12.6	0.1	2017-02-24	-178.8	-23.3	SSPA
1130	145.8	36.3	0.2	2017-02-24	-178.8	-23.3	OBN
1131	162.8	-16.5	-0.1	2017-03-29	162.8	56.9	QSPA
1132	-13.5	30.3	-0.0	2017-04-03	25.2	-22.7	FFC
1133	-33.1	14.5	0.1	2017-04-03	25.2	-22.7	ANMO
1134	-24.7	23.1	0.0	2017-04-03	25.2	-22.7	RSSD
1135	-25.7	14.2	0.0	2017-04-03	25.2	-22.7	CCM
1136	-32.1	7.3	0.2	2017-04-03	25.2	-22.7	HKT
1137	-32.5	17.9	0.4	2017-04-24	-72.1	-33.0	OBN
1138	-126.5	21.2	0.0	2017-04-24	-72.1	-33.0	YSS
1139	77.8	3.6	0.5	2017-04-28	125.1	5.5	MBAR
1140	105.1	-50.3	-0.4	2017-05-09	167.4	-14.6	BOSA
1141	102.6	-47.5	0.3	2017-05-09	167.4	-14.6	LBTB
1142	172.4	30.9	0.2	2017-05-29	120.4	-1.3	PFO
1143	78.2	-16.8	0.3	2017-07-06	124.6	11.1	SUR
1144	-166.6	-39.6	0.4	2017-07-06	124.6	11.1	LVC
1145	77.0	-3.1	0.7	2017-07-06	124.6	11.1	LSZ
1146	83.1	-2.8	-0.0	2017-07-11	164.0	-49.5	BFO
1147	-157.7	-3.1	0.1	2017-07-11	164.0	-49.5	COR
1148	128.7	18.3	0.0	2017-07-11	164.0	-49.5	LVZ
1149	-133.4	-11.2	0.1	2017-07-11	164.0	-49.5	WVT
1150	133.3	21.1	-0.1	2017-07-11	164.0	-49.5	KEV
1151	173.4	1.2	0.1	2017-07-11	164.0	-49.5	ADK
1152	40.8	-29.4	-0.2	2017-07-20	27.4	36.9	VNDA
1153	52.6	-18.6	-0.1	2017-07-20	27.4	36.9	CASY
1154	39.5	-29.9	-0.1	2017-07-20	27.4	36.9	SBA
1155	-17.9	7.2	-0.1	2017-07-20	27.4	36.9	CPUP
1156	106.0	-16.6	-0.2	2017-08-08	103.9	33.2	CASY
1157	62.9	11.3	0.5	2017-08-08	103.9	33.2	LSZ
1158	-140.6	-11.3	0.1	2017-10-08	176.8	52.4	PMSA
1159	48.7	-4.7	-0.1	2017-10-10	8.6	-54.3	MAKZ
1160	62.4	-4.9	0.2	2017-10-10	8.6	-54.3	ULN
1161	129.3	-60.6	0.2	2017-10-10	8.6	-54.3	HNR
1162	-157.9	-18.2	0.1	2017-10-24	123.1	-7.2	OTAV
1163	165.0	52.2	0.5	2017-10-24	123.1	-7.2	SSPA
1164	-178.9	30.0	-0.1	2017-10-24	123.1	-7.2	HKT
1165	151.2	39.5	0.1	2017-10-31	169.1	-21.7	KEV
1166	100.2	-15.0	-0.4	2017-10-31	169.1	-21.7	FURI
1167	100.1	-14.8	-0.1	2017-11-01	168.9	-21.6	FURI

Measurement Index	Bounce Point (Longitude°)	Bounce Point (Latitude°)	$S_{\mathrm{LAB}}S$ Amplitude	Earthquake Date	Earthquake (Longitude°)	Earthquake (Latitude°)	Station Name
1168	-165.6	38.1	0.2	2017-11-04	-173.2	-15.3	ALE
1169	-168.0	-52.1	0.5	2017-11-07	143.5	-4.2	PLCA
1170	-150.6	-40.2	-0.8	2017-11-07	143.5	-4.2	LVC
1171	87.7	-17.8	0.3	2017-11-07	143.5	-4.2	LSZ
1172	-27.1	41.2	0.1	2017-11-12	46.0	34.9	BCIP
1173	-148.6	0.1	0.2	2017-11-13	-84.5	9.5	PMG
1174	-29.1	-5.2	-0.8	2017-11-13	-84.5	9.5	LSZ
1175	-21.4	-11.5	0.1	2017-11-13	-84.5	9.5	ABPO
1176	-146.1	-12.2	-0.1	2017-11-13	-84.5	9.5	CTAO
1177	176.8	46.2	0.2	2017-11-19	168.6	-21.5	BORG
1178	100.1	-14.4	-0.0	2017-11-19	168.7	-21.3	FURI
1179	-127.7	-3.5	0.2	2017-11-19	168.7	-21.3	SJG
1180	-29.2	55.0	0.2	2017-11-30	-23.4	-1.1	BILL
1181	-55.2	55.5	-0.6	2017-11-30	-23.4	-1.1	ADK
1182	-0.4	-66.7	0.3	2017-11-30	-23.4	-1.1	TAU
1183	-126.5	-46.0	-0.7	2017-12-13	2.2	-54.2	POHA
1184	154.4	9.1	0.2	2017-12-15	108.2	-7.5	POHA
1185	165.8	32.7	-0.0	2017-12-15	108.2	-7.5	TUC
1186	178.9	37.4	-0.2	2017-12-15	108.2	-7.5	TEIG
1187	-134.1	54.2	-0.3	2018-01-10	-83.5	17.5	ERM
1188	-142.2	-42.7	0.1	2018-01-14	-74.7	-15.8	CTAO
1189	45.2	-1.4	0.1	2018-01-28	9.7	-53.1	KURK
1190	-34.8	-12.8	0.2	2018-01-28	9.7	-53.1	BBSR
1191	-28.2	21.9	0.3	2018-01-28	9.7	-53.1	COLA
1192	89.0	-36.7	0.1	2018-01-28	9.7	-53.1	DAV
1193	107.0	-39.3	0.2	2018-01-28	9.7	-53.1	GUMO
1194	127.2	-60.2	0.1	2018-01-28	9.7	-53.1	HNR
1195	-137.6	-49.8	0.7	2018-01-28	9.7	-53.1	KIP
1196	-132.5	-49.7	0.3	2018-01-28	9.7	-53.1	POHA
1197	-151.3	77.6	-0.4	2018-02-16	-98.0	16.4	LSA
1198	-160.6	-4.0	-0.2	2018-02-16	-98.0	16.4	WRAB
1199	-154.8	-3.5	-0.3	2018-02-16	-98.0	16.4	CTAO
1200	-168.6	29.2	0.1	2018-02-16	-98.0	16.4	DAV
1201	-140.1	5.2	0.1	2018-02-16	-98.0	16.4	FUNA
1202	-34.6	1.2	0.3	2018-02-16	-98.0	16.4	LSZ
1203	-166.7	-7.3	0.1	2018-02-16	-98.0	16.4	MBWA
1204	-143.6	12.4	-0.4	2018-02-16	-98.0	16.4	TARA
1205	-144.8	18.4	0.1	2018-03-08	153.2	-4.4	GTBY
1206	158.1	45.6	-0.2	2018-03-08	153.2	-4.4	ALE
1207	-163.4	22.9	0.1	2018-03-08	153.2	-4.4	ANMO
1208	-149.4	36.7	0.5	2018-03-08	153.2	-4.4	BBSR
1209	169.8	33.1	0.1	2018-03-08	153.2	-4.4	COLA
1210	-167.0	29.5	0.1	2018-03-08	153.2	-4.4	RSSD
1211	-157.5	28.9	0.2	2018-03-08	153.2	-4.4	WVT
1212	-127.4	41.0	0.1	2018-04-02	-63.0	-20.7	TATO
1213	-158.4	-66.0	0.2	2018-05-04	-155.0	19.3	BOSA
1214	-111.1	2.1	0.0	2018-05-04	-155.0	19.3	LPAZ
1215	-162.6	-30.1	0.3	2018-05-04	-155.0	19.3	VNDA
1216	-178.7	-30.4	0.1	2018-05-04	-155.0	19.3	CASY
1217	-130.5	-29.1	-0.2	2018-05-04	-155.0	19.3	PMSA
1218	-155.1	-35.3	-0.5	2018-05-04	-155.0	19.3	QSPA

Measurement Index	Bounce Point (Longitude°)	Bounce Point (Latitude°)	$S_{\mathrm{LAB}}S$ Amplitude	Earthquake Date	Earthquake (Longitude°)	Earthquake (Latitude°)	Station Name
1219	-92.9	13.1	0.4	2018-05-04	-155.0	19.3	RCBR
1220	-161.7	-30.1	0.3	2018-05-04	-155.0	19.3	SBA
1221	-176.1	52.8	-0.1	2018-08-05	116.4	-8.3	SDDR
1222	169.0	46.8	-0.0	2018-08-05	116.4	-8.3	WVT
1223	-118.4	-0.2	0.4	2018-08-15	-178.0	51.4	EFI
1224	152.8	44.1	0.4	2018-08-17	119.8	-7.4	FFC
1225	94.5	-59.9	-0.4	2018-08-17	119.8	-7.4	HOPE
1226	170.2	42.6	0.3	2018-08-17	119.8	-7.4	CCM
1227	-175.5	52.1	-0.4	2018-08-19	116.6	-8.3	SDDR
1228	171.7	32.1	-0.0	2018-08-19	116.6	-8.3	ANMO
1229	168.0	45.0	-0.1	2018-08-19	116.6	-8.3	CCM
1230	160.8	32.2	0.3	2018-08-19	116.6	-8.3	COR
1231	177.7	46.2	0.5	2018-08-19	116.6	-8.3	DWPF
1232	-165.6	-18.7	0.0	2018-08-19	116.6	-8.3	PAYG
1233	163.0	40.5	0.3	2018-08-19	116.6	-8.3	RSSD
1234	172.7	27.5	-0.4	2018-08-19	116.6	-8.3	TUC
1235	169.3	46.6	0.1	2018-08-19	116.6	-8.3	WVT
1236	-109.0	-44.0	0.1	2018-08-21	-62.9	10.8	TAU
1237	-133.0	-17.8	0.2	2018-08-21	-62.9	10.8	CTAO
1238	-121.8	2.3	0.0	2018-08-21	-62.9	10.8	FUNA
1239	-134.9	-71.1	0.1	2018-08-24	-70.8	-11.0	MBWA
1240	-117.8	13.2	-0.2	2018-08-24	-70.8	-11.0	MIDW
1241	-156.2	13.1	0.1	2018-09-05	141.9	42.7	RPN
1242	166.1	41.0	0.2	2018-09-06	179.3	-18.5	KEV
1243	-139.2	-0.9	0.2	2018-09-09	161.5	-10.0	BCIP
1244	-134.8	9.9	-0.1	2018-09-09	161.5	-10.0	SJG
1245	-137.7	4.1	0.5	2018-09-10	-179.4	-31.8	CCM
1246	-129.5	-3.0	0.7	2018-09-10	-179.4	-31.8	DWPF
1247	96.6	-39.5	0.3	2018-09-16	178.2	-25.4	MBAR
1248	103.2	-23.2	0.1	2018-09-16	178.2	-25.4	FURI
1249	-159.3	-0.1	0.1	2018-09-28	119.8	-0.2	OTAV
1250	179.5	26.1	-0.2	2018-09-28	119.8	-0.2	SLBS
1251	113.5	-62.3	0.0	2018-09-30	-178.1	-18.4	LBTB
1252	-90.5	-58.7	-0.2	2018-09-30	-178.1	-18.4	ASCN
1253	-123.7	-0.9	-0.6	2018-09-30	-178.1	-18.4	SJG
1254	-149.4	8.5	0.0	2018-10-10	151.2	-5.7	TGUH
1255	93.7	-30.9	-0.0	2018-10-10	151.2	-5.7	LBTB
1256	-165.2	19.7	-0.3	2018-10-10	151.2	-5.7	TUC
1257	156.3	-20.3	0.3	2018-10-10	156.3	49.3	QSPA
1258	-123.7	16.2	-0.2	2018-10-13	153.2	52.9	PLCA
1259	-130.3	3.0	0.5	2018-10-13	153.2	52.9	EFI
1260	143.9	15.1	-0.3	2018-10-16	169.5	-21.7	ULN
1261	-8.3	85.5	-0.1	2018-10-22	-129.4	49.3	KIV
1262	179.2	19.1	-0.2	2018-10-22	-129.4	49.3	CTAO
1263	-97.5	5.0	-0.0	2018-10-22	-129.3	49.3	PLCA
1264	-149.8	81.9	0.4	2018-10-25	20.6	37.5	KIP
1265	135.7	42.6	0.2	2018-11-09	-11.2	71.6	CTAO
1266	-41.9	3.8	0.5	2018-11-09	-11.2	71.6	PMSA
1267	163.7	41.1	0.4	2018-11-18	-178.9	-17.9	LVZ
1268	105.5	-51.8	0.2	2018-11-18	-178.9	-17.9	LSZ
1269	147.5	37.7	0.2	2018-12-05	169.4	-21.9	LVZ

Measurement Index	Bounce Point (Longitude°)	Bounce Point (Latitude°)	$S_{\mathrm{LAB}}S$ Amplitude	Earthquake Date	Earthquake (Longitude°)	Earthquake (Latitude°)	Station Name
1270	-131.4	-29.1	-0.0	2018-12-05	169.4	-21.9	NNA
1271	66.6	-14.9	0.0	2018-12-11	-26.4	-58.5	HIA
1272	70.0	-26.8	0.2	2018-12-11	-26.4	-58.5	XAN
1273	100.5	-51.6	-0.1	2018-12-11	-26.4	-58.5	DAV
1274	165.2	-11.3	0.1	2018-12-20	164.7	55.1	SBA
1275	-155.6	-49.4	-0.6	2019-01-05	-71.6	-8.1	KAPI
1276	-132.1	49.8	-0.1	2019-01-05	-71.6	-8.1	TATO
1277	-175.0	38.0	0.2	2019-01-06	126.8	2.3	HKT
1278	-176.3	25.8	0.0	2019-01-06	126.8	2.3	SLBS
1279	85.3	1.0	0.2	2019-01-22	42.4	-43.1	MDJ
1280	59.1	4.0	-0.4	2019-01-22	42.4	-43.1	KURK
1281	115.0	-42.8	-0.4	2019-01-22	42.4	-43.1	HNR
1282	82.5	13.5	0.3	2019-01-22	42.4	-43.1	MA2
1283	87.0	-11.7	0.3	2019-01-22	42.4	-43.1	TATO
1284	65.1	18.1	0.1	2019-01-22	42.4	-43.1	TIXI
1285	-29.7	-21.0	0.0	2019-02-22	-77.0	-2.2	LBTB
1286	-17.2	26.6	0.1	2019-02-22	-77.0	-2.2	UOSS
1287	-20.3	-3.1	-0.1	2019-02-22	-77.0	-2.2	KMBO
1288	-26.2	-14.1	0.1	2019-02-22	-77.0	-2.2	LSZ
1289	-6.4	-20.6	0.3	2019-03-01	-70.2	-14.7	MSEY
1290	7.5	-14.6	0.5	2019-03-01	-70.2	-14.7	PALK
1291	-136.1	39.9	-0.3	2019-03-01	-70.2	-14.7	TATO
1292	-165.6	22.6	0.2	2019-04-12	122.6	-1.8	TGUH
1293	157.1	47.7	0.0	2019-04-12	122.6	-1.8	FFC
1294	-163.1	17.3	0.0	2019-04-12	122.6	-1.8	JTS
1295	70.3	-41.6	-0.2	2019-04-12	122.6	-1.8	TRIS
1296	176.0	47.6	0.2	2019-04-12	122.6	-1.8	WVT
1297	-158.8	31.4	0.5	2019-05-14	152.6	-4.0	WCI
1298	-154.8	-8.9	0.4	2019-05-30	-89.4	13.2	WRAB
1299	-147.9	1.6	-0.1	2019-06-15	-178.1	-30.6	PFO
1300	-95.2	-44.9	-0.0	2019-06-15	-178.1	-30.6	RCBR
1301	-132.4	7.7	0.3	2019-06-15	-178.1	-30.6	SSPA
1302	-135.0	5.3	0.2	2019-06-15	-178.1	-30.6	WCI
1303	-158.4	37.1	-0.1	2019-06-24	129.2	-6.4	SJG
1304	-175.1	16.9	0.2	2019-06-24	129.2	-6.4	SLBS
1305	-39.5	10.9	0.1	2019-07-04	-117.5	35.7	BOSA
1306	-85.0	-12.0	-0.0	2019-07-04	-117.5	35.7	HOPE
1307	-85.0	-12.0	-0.0	2019-07-06	-117.6	35.8	HOPE
1308	62.8	-18.4	0.7	2019-07-07	126.2	0.5	SHEL
1309	178.8	31.4	0.1	2019-07-07	126.2	0.5	TUC
1310	177.4	49.2	0.1	2019-07-07	126.2	0.5	WCI
1311	176.3	31.4	0.0	2019-07-14	120.4	-18.2	CCM
1312	-175.8	18.1	0.1	2019-07-14	120.4	-18.2	HKT
1313	-165.3	4.0	0.2	2019-07-14	120.4	-18.2	TEIG
1314	-157.4	17.3	-0.3	2019-07-14	128.0	-0.6	BCIP
1315	-162.2	40.0	0.2	2019-07-14	128.0	-0.6	GTBY
1316	-161.2	34.9	-0.0	2019-07-14	128.0	-0.6	MTDJ
1317	-165.7	28.9	0.3	2019-07-14	128.0	-0.6	TEIG
1318	105.0	-51.9	0.3	2019-07-31	168.0	-16.2	BOSA
1319	67.0	-52.4	-0.1	2019-07-31	168.0	-16.2	DBIC
1320	-106.5	-6.2	-0.1	2019-07-31	168.0	-16.2	SACV

Measurement Index	Bounce Point (Longitude°)	Bounce Point (Latitude°)	$S_{\mathrm{LAB}}S$ Amplitude	Earthquake Date	Earthquake (Longitude°)	Earthquake (Latitude°)	Station Name
1321	-130.1	1.9	-0.3	2019-07-31	168.0	-16.2	SJG
1322	-102.1	15.0	-0.7	2019-08-01	-72.3	-34.2	KDAK
1323	-145.8	9.7	-0.3	2019-08-01	-72.3	-34.2	INCN
1324	77.1	-25.3	0.1	2019-08-27	-26.6	-60.2	BJT
1325	140.9	-64.4	-0.6	2019-08-27	-26.6	-60.2	PMG
1326	144.7	40.3	-0.0	2019-09-01	-178.6	-20.4	KIEV
1327	172.5	47.6	0.1	2019-09-01	-178.6	-20.4	KONO
1328	-161.6	35.1	0.0	2019-09-25	128.4	-3.5	GTBY
1329	138.7	-65.3	0.1	2019-09-25	128.4	-3.5	EFI
1330	-159.7	11.8	-0.1	2019-09-25	128.4	-3.5	JTS
1331	169.5	32.0	0.2	2019-09-25	128.4	-3.5	COR
1332	-179.6	27.3	-0.0	2019-09-25	128.4	-3.5	TUC
1333	70.7	-54.8	-0.1	2019-09-29	-73.2	-35.5	KMI
1334	-137.0	10.3	0.0	2019-09-29	-73.2	-35.5	ERM
1335	-149.0	5.8	-0.0	2019-09-29	-73.2	-35.5	INCN
1336	-48.8	23.4	-0.0	2019-09-29	-73.2	-35.5	KEV
1337	130.1	-60.6	-0.0	2019-10-29	125.0	6.8	EFI
1338	-172.4	53.1	0.6	2019-10-29	125.0	6.8	DWPF
1339	-155.8	16.7	0.0	2019-10-29	125.0	6.8	OTAV
1340	171.0	47.2	0.2	2019-10-29	125.0	6.8	RSSD
1341	60.1	15.7	0.0	2019-10-31	125.2	6.9	DBIC
1342	-167.7	36.6	-0.6	2019-11-04	-175.3	-18.6	ALE
1343	-132.5	18.7	-0.1	2019-11-04	-175.3	-18.6	HRV
1344	-133.8	16.3	0.2	2019-11-04	-175.3	-18.6	SSPA
1345	145.8	36.5	-0.1	2019-11-08	-179.5	-21.9	OBN
1346	171.2	47.1	0.4	2019-12-15	125.2	6.7	RSSD
1347	-167.0	39.6	0.3	2019-12-15	125.2	6.7	TEIG
1348	73.4	-10.5	0.4	2019-12-15	125.2	6.7	TSUM
1349	61.8	-16.6	-0.9	2020-01-24	39.1	38.4	CASY
1350	-20.3	8.1	0.1	2020-01-24	39.1	38.4	LCO
1351	7.9	-19.4	0.4	2020-01-24	39.1	38.4	PMSA
1352	-91.4	-36.9	0.2	2020-01-28	-78.8	19.4	VNDA
1353	-46.8	39.2	0.2	2020-03-31	-115.1	44.5	DBIC
1354	-26.4	25.8	0.2	2020-03-31	-115.1	44.5	LBTB
1355	178.5	20.5	-0.1	2020-03-31	-115.1	44.5	WRAB
1356	167.9	23.5	0.3	2020-03-31	-115.1	44.5	MBWA
1357	38.3	-31.1	0.0	2020-05-02	25.7	34.2	VNDA
1358	-94.7	-1.4	-0.2	2020-05-15	-117.9	38.2	PLCA
1359	-53.3	19.2	0.1	2020-05-15	-117.9	38.2	SHEL
1360	-172.4	20.6	0.5	2020-05-15	-117.9	38.2	PMG
1361	-99.5	-14.7	0.1	2020-05-15	-117.9	38.2	PMSA
1362	-131.5	-22.6	0.2	2020-05-15	-117.9	38.2	SBA
1363	13.8	-27.7	0.1	2020-06-03	-68.5	-23.3	PALK
1364	-175.0	-30.0	-0.0	2020-06-13	128.3	28.9	PLCA
1365	-159.7	79.0	-0.1	2020-06-13	128.3	28.9	BBSR
1366	176.3	16.1	-0.5	2020-06-23	-96.0	15.9	COCO
1367	-33.8	0.7	-0.0	2020-06-23	-96.0	15.9	LSZ
1368	-155.6	6.2	0.2	2020-06-23	-96.0	15.9	PMG
1369	-89.7	24.1	0.1	2020-08-30	-29.9	0.8	KIP
1370	-90.5	-23.0	-0.1	2020-08-30	-29.9	0.8	RAR
1371	-22.8	32.3	-0.2	2020-09-01	-71.3	-28.0	MAKZ

Measurement Index	Bounce Point (Longitude°)	Bounce Point (Latitude°)	$S_{\mathrm{LAB}}S$ Amplitude	Earthquake Date	Earthquake (Longitude°)	Earthquake (Latitude°)	Station Name
1372	-55.6	19.9	0.4	2020-09-01	-71.4	-27.9	BORG
1373	35.9	-41.2	-0.0	2020-09-01	-71.4	-27.9	CHTO
1374	-34.5	55.8	0.4	2020-09-18	-26.9	0.9	BILL
1375	38.9	-29.4	-0.3	2020-10-30	26.8	37.9	SBA
1376	-46.3	21.6	0.1	2020-12-27	-75.0	-39.3	LVZ
1377	-162.5	-32.6	0.1	2020-12-27	-75.0	-39.3	GUMO
1378	-43.5	13.4	0.2	2020-12-27	-75.0	-39.3	KONO
1379	-161.3	-50.2	0.4	2020-12-27	-75.0	-39.3	PMG
1380	-143.6	-18.8	-0.1	2020-12-27	-75.0	-39.3	WAKE